Development and Optimisation of a Liquid Argon Detector as a Prototype Liquid Argon Positron Emission Tomography Photon Detector

Theodoros Christodoulou

Department of Physics
Royal Holloway, University of London

A thesis submitted to the University of London for the degree of Doctor of Philosophy

17th March 2022

Declaration

I confirm that the work presented in this thesis is my own. Where information has been derived from other sources, I confirm that this has been indicated in the document.

Signed: Theodoros Christodoulou

Date: 17th March 2022

Abstract

In Positron Emission Tomography (PET), patients ingest or are injected with a radioactive beta-plus (positron) emitter. PET scan's ability to examine the body at a molecular and cellular level makes it one of the most critical imaging methods in clinical medicine. Depending on the area under examination, the procedure can take from 30 minutes up to 3 hours, and the activity of the radioactive tracer is adjusted based on the scan time and patient size. Long scan times result in a higher dose absorbed by the patient, which is not wanted. To reduce the scan time of a PET scan, the detection efficiency of the PET detector must be increased as high as possible. From the current scintillation crystals used in PET imaging, liquid Argon (LAr) has the highest light yield, which leads to a decrease in the patient's scan time. Also, liquid Argon is as high as 60 times cheaper per cc than commercially available scintillation detectors, which is also a factor driving the LAr-based PET detector prototype construction.

Commonly, PET detectors consist of an array of small detector cells arranged in a cylindrical format around the patient's body. In this thesis, a LAr filled cell is optimised to yield the highest detection efficiency using GEometry ANd Tracking (GEANT4) simulations. Various cell geometries are tested, with and without a reflective coating material. Instead of using the established tetraphenyl butadiene (TPB) coating in the various cells under test, Aluminium with Magnesium Fluoride (Al+MgF_2) is used. TPB coating is used to shift the scintillation photons wavelength from the Vacuum Ultraviolet (VUV) range to the visible spectrum. This shifting introduces a time delay in detecting the scintillation photons that affects the Time-of-Flight (TOF) information. The limited number of photons collected during a PET scan makes images appear noisier and blurrier than other imaging methods, and TOF helps to improve the image quality of the reconstructed images. Al+MgF_2 has a reflectivity of approximately 84 % at 128 nm (LAr scintillation light wavelength), making it a good candidate for testing. As TPB coating is not used, specially designed Silicon photomultipliers that detect LAr VUV wavelength are used, which can also operate in cryogenic temperature and submerged in LAr. The cell geometry with the highest detection efficiency had its energy resolution tested. The thesis also contains a calculation of the depth of interaction of the 511 keV photons within the optimised cell using the TOF concept.

Alongside the GEANT4 simulation, a prototype LAr detector was built in the laboratory whose purpose is to compare the simulation results with the results acquired in the laboratory. The thesis shows the detailed methodology used to build the prototype's vacuum, cryogenic, monitoring and data acquisition systems. Due to Covid-19 restriction, cell optimisation was shifted more towards the

simulation side, and a single ring PET imaging detector was simulated using Geant4 Application for Emission Tomography (GATE). By inserting the optimised cell parameters found in the GEANT4 simulations and placing a human body phantom at the centre of the single ring PET detector, the reconstructed images are evaluated. A pixel-driven backprojection algorithm is built specifically for the evaluation of the single ring PET images.

Acknowledgements

There are many people I would like to thank without whom the completion of this thesis would not be possible. In three years at the physics department of Royal Holloway I had the opportunity to work in a stimulating and international environment. I have shared the laboratory with people I consider good friends now.

First, I would like to thank my supervisors, Professor Stewart Boogert and Dr Joseph Walding, who guided me throughout this project. For the last two years of my project, I worked closely with Professor Stewart Boogert, and I would like to thank him specifically. I consider myself lucky to be one of his PhD students. He always believed in me, and his refusal to give up on me fueled my eagerness to constantly improve and learn as much I could from his immeasurable knowledge and wisdom. I consider the countless time he spent with me throughout this project as a gift for which I will always be grateful.

Second, as this project required the construction of a prototype detector from scratch, many custom-made parts were designed. All these parts were then manufactured by the mechanical workshop team of Royal Holloway. Special thanks to Ian and Richard from the mechanical workshop team, as they were always cooperative and tried to deliver the parts as soon as possible. Also, I would like to thank Andy, Tom and Ian from the support staff as they were always willing to help me with the simplest tasks of providing an extra pair of hands during the construction of the detector from the more time consuming such as placing orders and finding in-house equipment I needed for my project.

Third, I would like to thank Andrei and Kiril, which we have spent countless hours in the laboratory together, each working on his own project, but always it felt like we were a team willing to help each other with any difficulties we encountered on our projects. Furthermore, I would like to thank William Shields, a person I consider to be the link that connects all the PhD students. He always helps anyone requesting help, and I would like to thank him for dragging me out of the laboratory on Friday nights for a relaxing drink at the Pub.

Last but not least, I would like to thank my family and my wife Maria, who has provided me with immense support during my PhD.

Contents

List of Figures

List of Tables

Chapter 1

Positron Emission Tomography

Positron Emission Tomography (PET) is a non-invasive imaging method in diagnostic medicine. The basic principle is that a patient ingests or is injected with a radioactive β^+ (positron) emitter. These radionuclides are produced either in a cyclotron or by radioisotope generators such as ^{82}Rb through an elution process. Depending on the biological process of interest, are then tagged to a tracer compound (e.g. Fluorodeoxyglucose). The positron annihilates with an electron within the patient, and this annihilation produces two back-to-back gamma-ray photons. Assuming the gamma-rays do not interact with the patient as they exit, they then point towards the location where the beta emitter was absorbed. The detection of these gamma rays, through image reconstruction algorithms, leads to the three-dimensional (3D) image of the object of interest. Each image is segmented into small box shape elements (voxels), which have values proportional to the amount of the tracer absorbed. Hence, the spatial distribution of the tracer inside a living human can be mapped quantitatively. This chapter will give an overview of the physical principles underlying PET detectors, including the mathematical algorithms used to form an image.

1.1 Physics of Positron Emission and Annihilation

1.1.1 Positron Emission and Annihilation

A nucleus of an atom consists of protons and neutrons. Protons are positively charged particles, whereas neutrons are neutral. As protons in an atom are positively charged, a repulsive force is exerted between them. To hold the nucleus together, a force called the strong nuclear force opposes and overcomes this repulsive electrostatic force, and the atom is considered to be in a stable configuration. However, when the strong force holding the nucleus together is not sufficient, the atom becomes unstable and to reach a stable configuration, the nucleus decays and emits radiation. Three of the most common types of decays are alpha (α-decay), beta (β-decay) and gamma (γ-decay), all of which involve emitting of one or more particles or photons.

The decay of interest in PET imaging is the β-decay, and more specifically, the β^+-decay. There are two types of β-decay, β^- and the β^+. During β^--decay, a neutron (n) in an atom's nucleus turns into a proton (p), an electron (e^-) and an antineutrino, whereas in a β^+-decay a proton in an atom's nucleus turns into a neutron, a positron (e^+) and an electron neutrino (ν_e). Positrons are positively charged, and as they are the antiparticles of electrons, their mass is equal to 0.511 MeV. In the literature as well as in this thesis, the terms positron and β^+ particle are used interchangeably. It will become evident when the annihilation process is explained why only the β^+-decay is of interest in PET imaging, but first, an understating of β^+-decay is important. The process of β^+ emission is shown in Figure 1.1 and can be represented as

$$p \rightarrow n + e^+ + \nu_e. \tag{1.1}$$

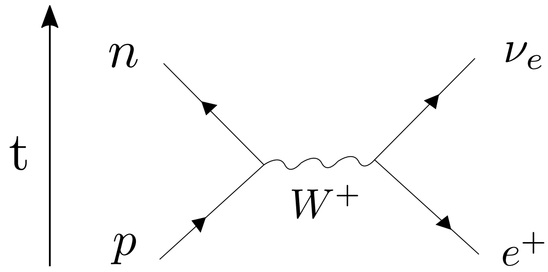

Figure 1.1: Feynman diagram of the β^+-decay. A proton (p) in an atom's nucleus turns into a neutron (n), a positron (e^+) and an electron neutrino (ν_e). To conserve charge, the W carries a positive charge which it transfers to the positron upon its decay.

As the neutron mass is greater than that of the proton, this process can only occur inside a nucleus when the daughter nucleus has greater binding energy (and therefore lower total energy) than the mother nucleus. The difference between these energies goes into the reaction of converting a proton into a neutron, a positron, a neutrino and there respective kinetic energy. Equation 1.2 shows the β^+-decay of ^{22}Na, which is the radioactive source used in this thesis

$$^{22}_{11}\mathrm{Na} \rightarrow ^{22}_{10}\mathrm{Ne} + \beta^+ + \nu_e. \tag{1.2}$$

The maximum kinetic energy of a positron $E_{e^+,\max}$ depends on the parent nucleus involved in the decay and is equal to

$$E_{e^+,\mathrm{max}} = Q - 2m_ec^2 - E_i \tag{1.3}$$

where Q is the difference between the sum of the masses of the initial reactants and the sum of the masses of the final products in energy units, usually in MeV, m_e the rest mass of the electron, c the speed of light, and E_i the energy level to which the decay occurred.

The amount of activity of any radionuclide may be expressed as the number of decays per unit time. The SI unit of radioactivity is the becquerel (Bq) and is defined as one radioactive decay per second. Radioactive samples decay exponentially and the relationship between the activity of a sample at specific time $A(t)$, is given by

$$A(t) = A(0)e^{-\lambda t} \tag{1.4}$$

where $A(0)$ is the initial activity of the sample, λ is the decay constant, and t is the time that the radioactive source activity is measured. The decay constant λ is described by

$$\lambda = \frac{\ln 2}{T_{1/2}} \tag{1.5}$$

where $T_{1/2}$ is the half life of the radionuclide sample.

The positron released during the β^+-decay has a very short lifetime in an electron-rich material such as human cells. Through inelastic interactions with atomic electrons, positrons lose energy rapidly and then combine with electrons. This process is called annihilation and is the basis of PET imaging. The positron annihilates with an electron in an atom within the patient, and this annihilation produces two back-to-back gamma-ray photons, see Figure 1.2. The positron and electron are almost at rest when the annihilation occurs, and therefore the energy released comes primarily from the mass of the particles.

The amount of energy that the two back-to-back photons carry can be calculated using Einstein's well known relativistic equation, and the conservation of energy and momentum. The equation that relates the energies of the emitted photons E_{γ_1} and E_{γ_2} and the angle between them is

$$\frac{1}{E_{\gamma_1}} + \frac{1}{E_{\gamma_2}} = \frac{1 - \cos\theta}{m_ec^2} \tag{1.6}$$

where m_e is the rest mass of an electron, c the speed of light, and θ the angle between the emitted photons. As photons are emitted with equal energies and in opposite directions ($\theta = \pi$) one can see from Equation 1.6 that the energy of the emitted photons is equal to the rest mass of the electron

$$E_{\gamma_1} = E_{\gamma_2} = m_ec^2 = 511 \text{ keV}. \tag{1.7}$$

The annihilation process has two important properties which PET scanners utilise. First, the gamma-ray photons are very energetic, which means the probability of escaping a patient's body

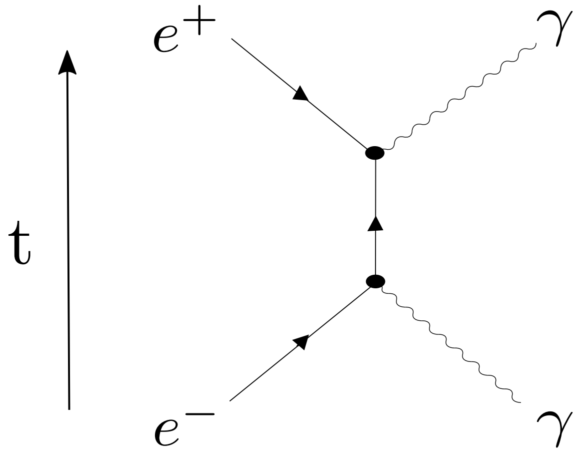

Figure 1.2: Feynman diagram of the annihilation of positron with an electron producing two gamma photons.

without interacting is high. Second, the annihilation photons are emitted in opposing directions, and by using this geometric relationship, the start point of the annihilation process within the patient can be estimated.

1.1.2 Positron Range and Noncolinearity

PET imaging systems spatial resolution is affected by two factors (a) the positron range and (b) the noncolinearity. These factors led to errors in determining the location of the positron-emitting radionuclide, and as a result, these errors manifest themselves in the reconstructed images as blurring. Positrons before their annihilation with electrons, follow a random path within a tissue due to the inelastic collisions with the surrounding atoms. For that reason, the exact distance travelled by the positron before its annihilation can not be determined. Therefore, the effective positron range is used to estimate this distance and is given by the shortest (perpendicular) distance from the emitting nucleus to the line joining the back-to-back photons, called the Line of Response (LOR), see Figure 1.3. The result of this approximated calculation of the distance that the positron is travelled inside a patient is the blurring of the image. Also, as the positrons are emitted with different energies, see Table 1.1, the magnitude of the blurring in an image is radionuclide dependant. The positron range distributions are not well described by gaussian functions and as a result the root mean square (rms) of the effective range is used to determine the blurring effect of the positron range to a PET image. A typical blurring caused by positron range is in the order of 0.5 to 3 mm (depends on the density of the absorber) [4].

Moreover, positrons and electrons are not entirely at rest during the annihilation process. That difference in their momentum results in the generation of the annihilation photons which are not exactly back-to-back ($\theta \neq \pi$). In fact, it will be emitted with a distribution of angles around 180^o, see Figure 1.3. The effect of noncolinearity is independent of the initial energy of the positrons, and the reason is that positrons must lose their energy before they can annihilate. The emitted photons roughly follow a Gaussian distribution with a maximum deviation of $\pm 0.25^o$ [2]. For a point source, the blurring effect of noncolinearity to a PET image Δ_{nc} [3] can be estimated by

$$\Delta_{\mathrm{nc}} \approx 0.0022D \tag{1.8}$$

where D is the diameter of the PET scanner. From equitation 1.8, it can be seen that the effect of blurring due to noncolinearity increases linearly with the detector diameter. For instance, in a human PET scanner of a diameter of 80 cm, the blurring effect is equal to 1.76 mm whereas for an animal PET scanner with a diameter of 15 cm is equal to 0.33 mm [3]. Table 1.1 shows the physical properties (half-life, positrons maximum kinetic energy, positrons range) of the most common radionuclides used in PET imaging [1].

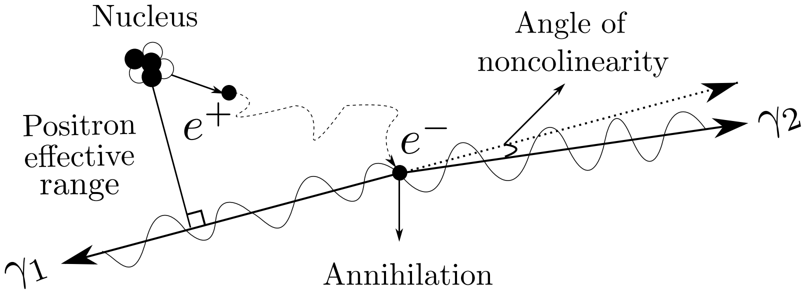

Figure 1.3: Positron travels a torturous path before its annihilation with the electron. The effective range of a positron is the shortest perpendicular distance from the line joining the back-to-back photons. As positron and electrons are not entirely at rest during the annihilation process, the back-to back photons are not emitted with exactly 180^0 angle between them.

Radionuclide	Source	Half-life (min)	$E_{e^+,\max}$(keV)	Mean positron range in water (mm)
^{11}C	Cyclotron	20.40	970	1.1
^{13}N	Cyclotron	9.96	1190	1.3
^{15}O	Cyclotron	2.07	1720	2.5
^{18}F	Cyclotron	110	635	0.5
^{68}Ga	Generator	68	1899	0.8
^{82}Rb	Generator	1.25	3356	0.8

Table 1.1: Physical characteristics of the most common radionuclides used in PET imaging.

1.2 Interaction of Gamma Rays with Matter

A spectroscopic radiation detector is solely built around the generation of a signal which is proportional to the energy of an incident radiation photon. When a gamma-ray interacts with a detection medium, it induces a signal proportional to the energy of incident radiation. Therefore, it is critical to understand how the annihilation photons interact with matter (e.g.human tissue, bones).

Photons interact with matter by transferring all or some of their energy to the atomic electrons of a material. Even though there are several interaction processes which may take place during a photon interaction (e.g. Rayleigh scattering, pair production) with matter the most dominate interactions in PET imaging is the photoelectric effect and the Compton scattering. The distinguishing factors in determining what process is most likely to happen is the energy of the incident photon E_{inc} and the atomic number of the absorber material Z [5], see Figure 1.4.

1.2.1 Photoelectric Effect

The photoelectric effect is dominant in energies less than 200 keV [5]. This process occurs when an incident photon transfers all of its energy to an electron (usually k-shell electron) of an atom. This photoelectron is ejected from the target atom with energy E_e equal to

$$E_e = E_\gamma - U_{\text{K,L,M,..}} \tag{1.9}$$

where E_γ is the energy of the incident photon, and $U_{\text{K,L,M,..}}$ is the binding energy of the electrons on K,L,M,.. shells. When the photoelectric effect occurs in an atom; a vacancy is created in the electron shell from the ejected electron. Subsequently, a cascade of electrons from a higher-level shell fills the vacancy, and an X-ray photon whose energy is equal to the difference between the initial and final energy levels.

A single function which describes the probability of the photoelectric interaction (τ) in all energy

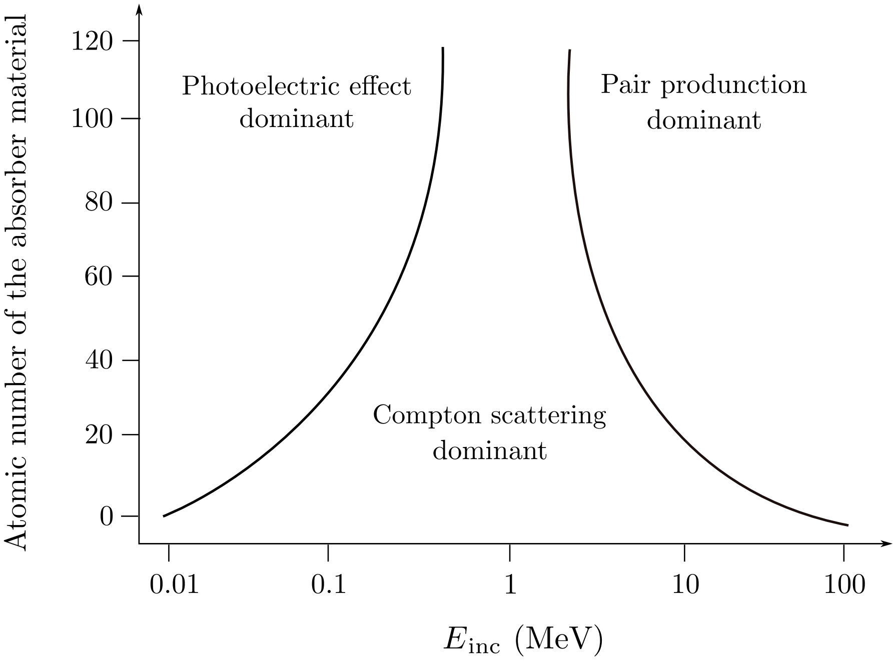

Figure 1.4: The dominant gamma-ray interaction mechanisms as a function of energy of the incident photon E_{inc} and atomic number Z [5]. The solid black lines show the values of Z and E_{inc} for which the two neighbouring interactions are equal.

ranges as a function of the atomic numbers Z is not available. However, it can be shown [6] that it is approximately

$$\tau \propto \frac{Z^n}{E_\gamma^3} \tag{1.10}$$

where n varies between 3 and 4 over the gamma-ray energy region of interest, and E_γ is the energy of the gamma-ray.

1.2.2 Compton Scattering

Compton scattering occurs when an incident photon scatters off a free or loosely bound electron in a material. During this process, the incident photon transfers some of its energy to the electron resulting in changing direction. Then, that electron is ejected from the atom, and its so called recoil electron. Using the conservation of energy and momentum, the energy of the scattered photon E_{sc} is equal to

$$E_{\text{sc}} = \frac{E_\gamma}{1 + \frac{E_\gamma}{m_e c^2}(1 - \cos\theta)} \tag{1.11}$$

where E_γ is the energy of the incident photons, m_e the rest mass of the electron, c the speed of light and θ the scattering angle.

The probability that the gamma-ray will undergo a Compton scattering is proportional to the atomic number Z, as when the atomic number increases, the number of possible targets increases as well. The differential cross-section $\frac{d\sigma}{d\Omega}$ of scattered gamma rays incident on a single electron is equal to

$$\frac{d\sigma}{d\Omega} = Zr_o^2\left(\frac{1}{1+\alpha(1-\cos\theta)}\right) + \left(\frac{1+\cos^2\theta}{2}\right) + \left(1+\frac{\alpha^2(1-\cos\theta)^2}{(1+\cos^2\theta)[1+\alpha(1-\cos\theta)]}\right) \tag{1.12}$$

where Z is the atomic number, r_o the classical electron radius ($\approx 2.8 \times 10^{-15}$ m), θ the scattering angle, and α is equal to the energy of the incident gamma-ray E_{inc} divided by the electron rest mass energy. The differential cross-section of a scattering gamma-ray on a single electron can be also calculated by Klein-Nishina formula [7].

1.2.3 Interaction Cross Section

The interaction of photons $I(x)$ with a material of specific mass thickness can be described as

$$I(x) = I(0)e^{-\mu_{\text{tot}}x} \tag{1.13}$$

where $I(0)$ is the initial intensity of the gamma-ray, μ_{tot} is the sum of the linear attenuation coefficients of all photon interaction with the material at the energy of interest, and x the mass thickness of the material defined as the mass per unit area. In PET imaging the two dominant interactions are the photoelectric effect and Compton scattering. Therefore, the total value of the linear attenuation coefficient μ_{tot} is approximately the sum of that two interactions and is equal to

$$\mu \approx \mu_{\text{Compton}} + \mu_{\text{photoelectric}} \tag{1.14}$$

where μ_{compton} is the linear attenuation coefficient due to the Compton interactions, and $\mu_{\text{photoelectric}}$ the linear attenuation coefficient due to the photoelectric absorption. The probability that an incident photon will not interact with a material P_T (transmittance) is equal to

$$P_T = \frac{I(x)}{I(o)} = e^{-\mu x}. \tag{1.15}$$

A PET scanner aims to detect the annihilation photons that escape a patient's body without interacting. Therefore, the detector medium must be able to stop these photons either with large values of μ_{tot} or by using dense materials, or both. The interaction probability P_I is defined as

$$P_I = 1 - P_T. \tag{1.16}$$

Three media are of potential interest in PET imaging (a) the tissue of the body, (b) the detector material and (c) any material used for shielding or collimation. Because liquid argon is the detection

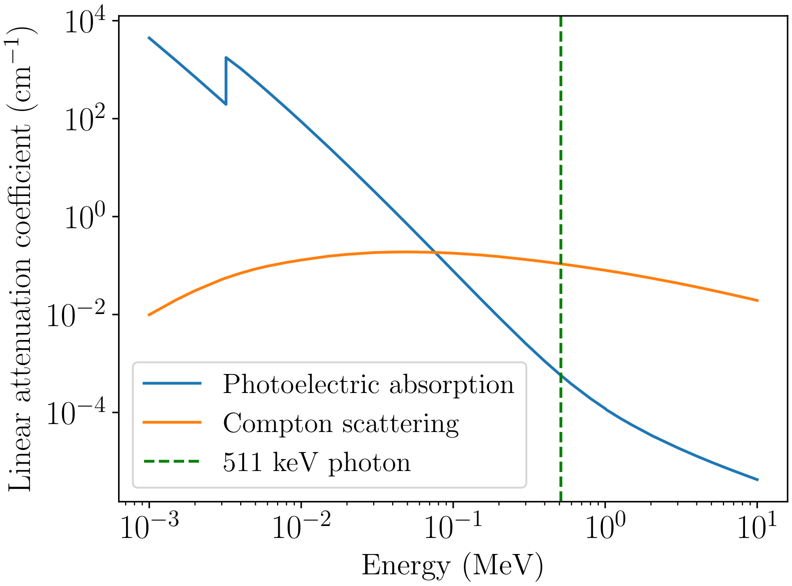

Figure 1.5: Liquid argon linear attenuation coefficient as a function of energy. The sharp discontinuity on the blue line is the K absorption edge (energy level just beyond the binding energy). The doted green line shows the sum of the linear attenuation coefficient due to photoelectric absorption and Compton scattering at at 511 keV (plot made from data acquired from NIST XCOM: Photon Cross Sections Database) [15].

medium under test, Figure 1.5 shows the linear attenuation coefficient of liquid argon (LAr) as a function of energy. Table 1.2 shows the attenuation coefficient of soft tissue, bone, lead, tungsten and LAr at 511 keV [8]. Lead and tungsten are two commonly used materials in PET imaging centres, and that is why they are included in Table 1.2.

Material	μ_{Compton} (cm^{-1})	$\mu_{\text{photoelectric}}$ (cm^{-1})	μ_{tot} (cm^{-1})
Soft tissue	0.096	0.00002	0.096
Bone	0.169	0.001	0.170
Lead	0.76	0.89	1.78
Tungsten	1.31	1.09	2.59
LAr	0.109	0.0006	0.110

Table 1.2: Linear attenuation coefficients for soft tissue, bone, lead, tungsten [8] and LAr at 511 keV, for the two dominant interactions in PET imaging (μ_{Compton}, $\mu_{\text{photoelectric}}$), and the total linear attenuation μ_{tot} derived from all photon interaction at 511 keV.

1.3 PET Detectors Imaging Technology

1.3.1 PET Detectors

To obtain the best possible image quality, a PET scanner must have an excellent detection efficiency (the more annihilation photons are detected, the better the signal to noise ratio in the image) and also give precise information on the spatial location of the detected annihilation events. To achieve a good spatial resolution PET detectors must have an array of small detector elements for which the precision of localisation is based on the detector's size, or by using a large detection medium with position-sensitive capabilities. It is also essential to be able to determine the time when the 511 keV photons are detected, as this information is used to determine which photons have arrived closely enough in time to be considered as an annihilation pair, which have originated from the same radioactive decay. This is called timing resolution and typically can range from 2 to 6 ns. A time window which is double or triple the typical time resolution is used in PET scanners to avoid any accidental rejection of annihilation events. Also, as the annihilation photons may interact with the patient's tissue and therefore lose energy (i.e. Compton scattering photons), a PET detector must be able to distinguish between the incident photons different range of energies. This ability is called energy resolution and allows the correct registration of the annihilation events used for the reconstruction of the image.

Almost all of the detectors used for the detection of the annihilation pairs in a PET scanner are scintillation detectors. These detectors serve as an interacting medium for high energy photons. When energy is deposited into a scintillation material, it lifts its atoms into an excited state called luminescence (emission of visible or near-visible light photons). When the atom returns to its ground state it emits scintillation photons with an energy proportional to the energy absorbed by the detector material. Subsequently, this energy is converted to an electrical signal by detectors sensitive to the wavelength of scintillation photons generated. The vast majority of commercially available PET scanners use photomultiplier tubes (PMTs) for the conversion of the scintillation light to an electrical current. However, in some PET detectors, silicon photomultipliers (SiPM) are used to convert the scintillation light into an electrical current. SiPM properties and characteristics will be described in Chapter 2.

1.4 Photomultiplier Tubes

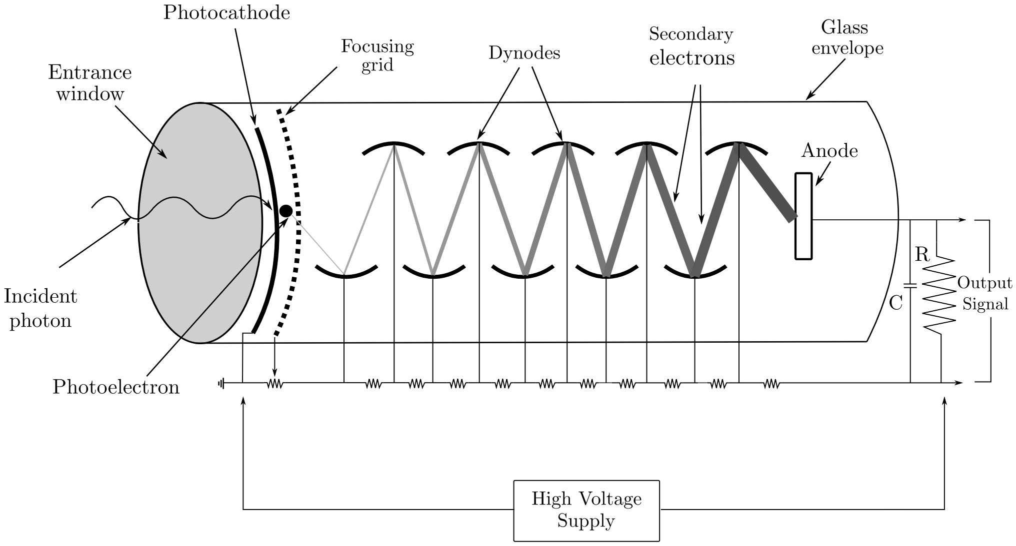

Figure 1.6: Schematic of a photomultiplier tube (PMT). A PMT is comprised of multiple dynodes, which are electrodes that are progressively held at higher voltages through a resistor chain. The dynodes are coated with an emissive material and placed inside a vacuum-sealed glass tube. Additionally, the inner surface of the entrance window, known as the photocathode, is coated with an emissive material. When light photons hit the photocathode, they release electrons into the tube, which are then accelerated by the potential difference to reach the first dynode. Upon striking the first dynode, these electrons gain enough energy to release more electrons, which continue to be accelerated towards the subsequent dynodes. After ten stages of amplification, the electrical signal is measured.

From the electromagnetic interaction processes, the dominant process for which the scintillation light is converted to photoelectrons within the PMT is the photoelectric effect. Light from the scintillation medium is transmitted through a glass entrance window and ejects electrons from a negatively charged photosensitive compound called photocathode. An electric field then accelerates each photoelectron towards multiple dynodes (positively charged), prior to its detection in the anode (electron collector). Dynodes are also coated with an emissive material; therefore, secondary electrons are generated when the accelerated electron collides with the dynode. Usually, ten dynodes are inside a photomultipliers tube, and as a result, a ten stage amplification of the initial electron is generated, see Figure 1.6. This increase in the amplitude of the detected signal is refereed as gain, typically in the order of 10^6 and leads to a high signal-to-noise ratio. The operating voltage of PMTs is commonly between 1000-2000 V. PMTs typical shape is round with a diameter ranging from 1 to 5 cm. An output pulse of PMT is in a milliampere range with a response time in the order of nanoseconds.

1.4.1 Block Detectors

To localise the annihilation event, the majority of PMTs are coupled with the scintillation crystal in a block design, see Figure 1.7. As shown in Figure 1.7a, a block design configuration consist of a scintillation crystal coupled with four PMTs. A relatively large block of a scintillation crystal (typically $4 \times 4 \times 3$ cm) is segmented (saw cuts) into an array of smaller detector elements (often 8×8). To optically isolate the individual small detector elements, a reflective material is used between the gaps created from the segmentation of the scintillation material block. The depth of the cuts is not even along the detector block, and by carefully designing the depth of the cuts, a unique signal can be measured from the coupled PMTs. Deep cuts are located on the corners of the detector elements, whereas shallower cuts are located towards the middle. For example, if an annihilation photon hits the corner of the detector block, which the saw cuts are deeper, virtually all of the scintillation light produced from the interaction will be detected by the PMTs locate exactly underneath them. On the other hand, the annihilation photons which have interacted in the middle of the scintillation block will result in an even spread of the scintillation photons generated to the four PMTs coupled on the scintillation block. The X and Y coordinate for each annihilation photon that interacts with the scintillation block is calculated based on

$$X = \frac{A + B - C - D}{A + B + C + D} \tag{1.17}$$

and

$$Y = \frac{A + C - B - D}{A + B + C + D} \tag{1.18}$$

where A, B, C and D are the four PMTs signal as shown in Figure 1.7.

A further extension of the block detector design, which is commercially available in PET detectors, is the quadrant-sharing design. In this method, the size and the coupling design of PMTs, in each scintillation block are different from the standard block design. Larger PMTs are used compared to

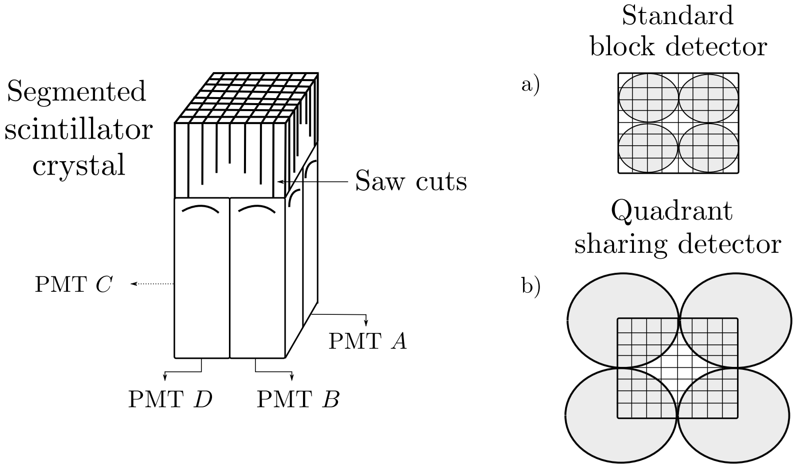

Figure 1.7: Schematic of a block detector design: a) standard PMT configuration used in a typical block detector design and b) shows the arrangement of the PMTs in the quadrant-sharing detector design.

the standard block design. The four edges of the scintillation block are placed at the centre of the PMTs (see Figure 1.7b). Still, four PMTs are used to decode each block, but each PMT now serves four different scintillator blocks. The block where the interaction occurs is determined by which four PMTs show a significant signal. Each PMT serves four different scintillation blocks, which reduces the total PMTs needed in PET scanners, typically by a factor of four. This reduction in the number of PMTs lowers the manufacturing cost of the PET scanner as PMTs are one of the most expensive parts. It's worth noting that the reduction in the number of PMTs also directly impacts the size and complexity of the electronics and data acquisition systems needed to read out the PMTs, which can further reduce the cost of the overall system. The location of the annihilation events is determined based on which four PMTs show a significant signal. To calculate the X and Y coordinate of the annihilation photons, Equation 1.17 is used (the same used in the standard block design).

1.5 Data Collection

The goal of a PET scanner is to record the annihilation events which have originated from the same radioactive decay and are detected without an energy loss or change in their direction (no scattering). These events are referred to as true coincidence. However, in a clinical scenario, these ideal circumstances are not possible, as the 511 keV photons may interact with the patient's body prior to their detection. Moreover, the geometry of a PET scanner which mostly is a ring shape leads to falsely registering undesirables events. These unwanted events are called random, scattered, and multiple coincidences, see Figure 1.8. These undesirable events degrade the image resolution even further from the already discussed factors which affect the image quality of a PET image (positron range and non-linearity), see Section 1.1.2.

1.5.1 Type of Events

True coincident events occur when two photons resulting from the same annihilation point are detected within a preset time and energy window. The time and energy window is different across different PET scanner manufacturers. However, its possible to have events which satisfy the above criteria but have not originated from the same annihilation point and therefore are falsely registered as true coincidence events. These events are called random coincidence events.

These events are indistinguishable from the true coincidence events, but their count rate can be estimated [9]. The number of random coincidence events per second N_R recorded is equal to

$$N_R = 2\tau N_1 N_2 \tag{1.19}$$

where τ is the width of the coincidence window and N_1 and N_2 are the annihilation photons detected per second by a pair of detectors.

As already stated in Section 1.2.2, the most dominant process at 511 keV is Compton scattering. Depending on the size and the geometry of the object, this type of events can range from 15% to well over 50% of the total events recorded. The photons which have undergone Compton scattering change direction before their detection. In principle, Compton scattering events are true coincidence events, but because of the changing in their direction, the line which connects the two opposing detectors (LOR) is incorrectly defined. One can argue that these events should arrive with an energy less than 511 keV and therefore can be filtered out. However, conventional PET scanners have poor energy resolution, and as a result, depending on the scintillation material, a wide range of photon energies are accepted. For example, in a PET scanner using Lutetium Oxyorthosilicate (LSO) as a scintillation medium, the accepted energy range is between 425 and 650 keV [10].

Lastly, multiple coincidence events occur when multiple detector pairs have detected annihilation events within the same time window. In this case, the position of the event becomes ambiguous, and therefore these events are discarded, despite the fact that some true coincidence events are also discarded.

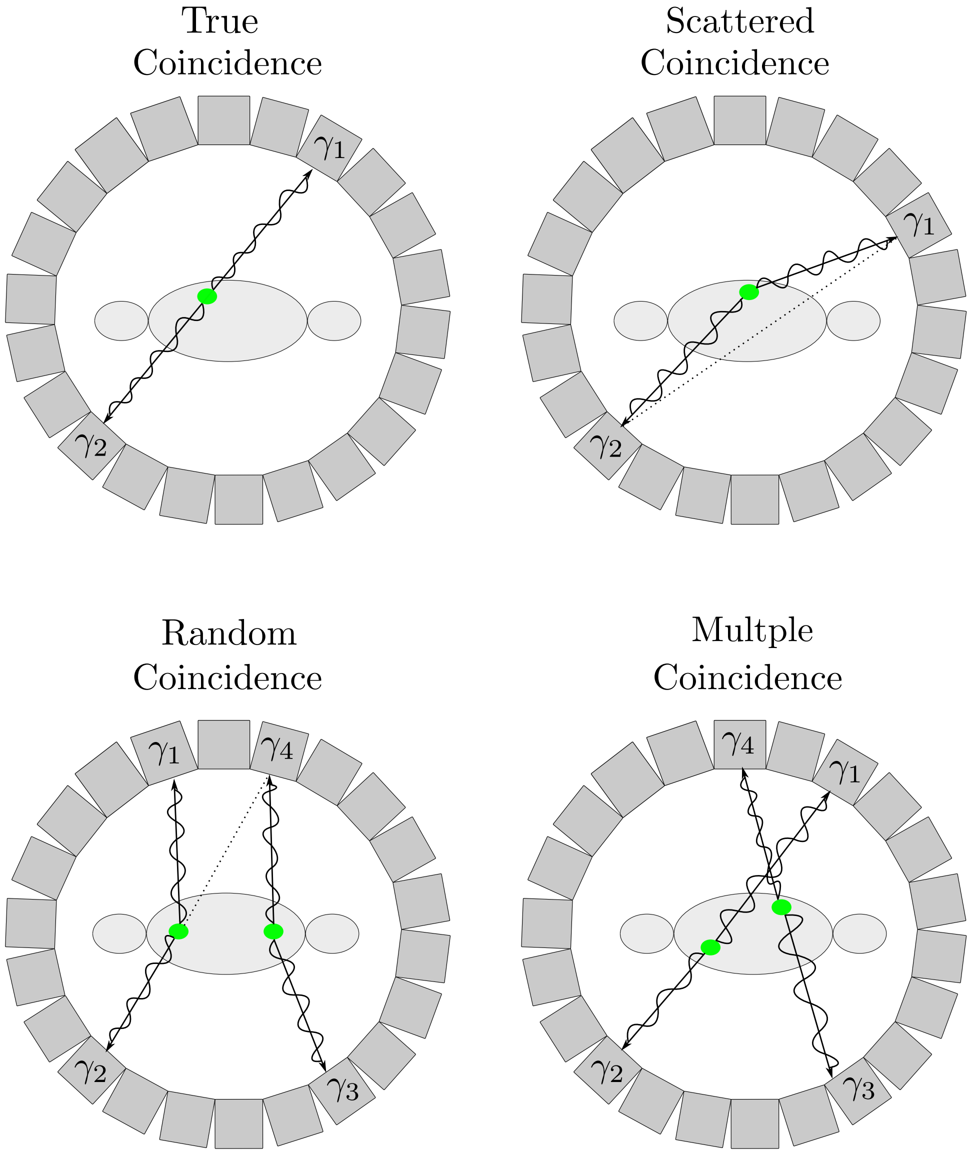

True Coincidence

Scattered Coincidence

Random Coincidence

Multple Coincidence

Figure 1.8: Illustration of the four main coincidence event types. Green circles show the point of annihilation. True coincidence: When both annihilation photons are detected without any scattering in the patient's body. Scattered coincidence: Annihilation photons undergo Compton scattering, and as a result, events are misspointed. Random Coincidence: A coincidence is recorded by two photons from separate annihilation events. Multiple Coincidence: Multiple annihilation events are recorded at the same time. These events generally are discarded.

1.6 Performance of PET Systems

1.6.1 Spatial Resolution and Depth Of Interaction

As discussed in the positron range and noncolinearity section, the image resolution of a PET image is limited. Moreover, the geometry of the detector degrades even further the image resolution due to the lack of information regarding the depth of interaction (DOI) within the crystal. The DOI widens the point spread function, and as a result, the spatial resolution of the image is reduced, see Figure 1.9. For example, if an annihilation event is created in the centre of the PET scanner, the intrinsic spatial resolution is determined by the width of the detector elements. However, if the annihilation event is emitted with an offset from the centre of the PET detector, the subtended solid angle of the detector increases, and therefore the spatial resolution decreases, see Figure 1.9.

In 1993, Derenzo and Moses developed an equation which encompasses all the various factors that can affect the spatial resolution of a PET scan image [11], [66]. That equation calculates the reconstructed image spatial resolution Γ for a point source located at radius r from the centre of a PET detector, and it is equal to

$$\Gamma = a\left[\left(\frac{d}{2}\right)^2 + b^2 + (0.0022D)^2 + s^2 + \frac{(Ar^2)}{r^2+R^2}\right]^{1/2} \tag{1.20}$$

where a is a multiplicative factor which accounts for the resolution degradation that occurs during the image reconstruction process; for conventional filtered backprojection reconstruction algorithms, see Section1.7.1, this term is typically set to 1.25, the first term in the square brackets is related to the geometry of the individual detector crystals and d represents the crystal width, b is the uncertainty in identifying the individual crystals when coupled to secondary detection systems such as PMTs, the term $(0.0022D)^2$, as already stated, describes the effect of noncolinearity, s^2 relates to the effective size of the object, which includes the positron range, A is a blurring factor due to DOI and depends on the detector material, and lastly, R the radius of the detector ring.

1.6.2 Sensitivity

The sensitivity of a PET scanner is defined as the number of counts per unit time detected by the device for each unit of activity present in a source. It is normally expressed in counts per second per microcurie or megabecquerel (cps/mCi or cps/MBq) [12]. Assuming that dead time is small, sensitivity depends on the geometric and detection efficiency of the PET scanner. The detection efficiency of a PET detector depends on the scintillation material decay time, the scintillation medium density, the scintillation medium atomic number, and the thickness of the detector material. The sensitivity S of a single ring PET detector is

$$S = \frac{A\epsilon^2 e^{-\mu_{tot}x}(3.7 \times 10^4)}{4\pi r^2} \tag{1.21}$$

where A is the detector area seen by a point source, ϵ the detector efficiency, μ_{tot} the linear attenuation coefficient of the detector material at 511 keV, x the thicknesses of the scintillation medium, and r is the radius of the detector.

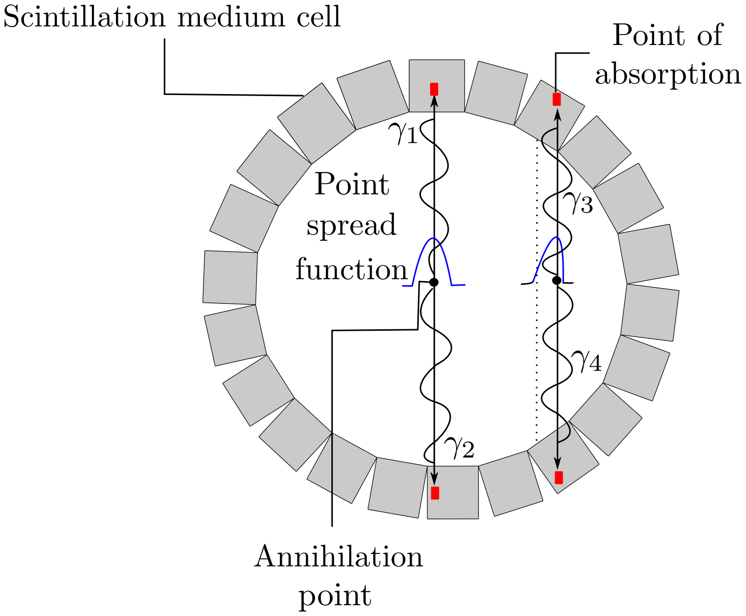

Figure 1.9: In a ring PET scanner, the point spread function becomes asymmetric with increasing radial offset because of the lack of the information regarding the depth of the annihilation photons absorption inside the scintillation medium. This results in degrading of the spatial resolution.

1.7 Image Reconstruction

The aim of image reconstruction is to give quantitatively accurate cross-sectional images of the positron-emitting radionuclides within the object of interest, using the information acquired from the externally detected radiation. This is done using mathematical algorithms of computed tomography or from the concept of Time Of Flight (TOF). Essentially these methods allow the clinical personnel to get a clinically useful diagnostic image. PET scanners typically consist of rings of detectors that fully encompasses the object to be imaged, as shown in Figure 1.8. The inadequacy of a single, ideal reconstruction method has resulted in the development of a range of image reconstructing techniques, each with their relative advantages and disadvantages. Generally, these methods fall into one of two distinct categories; analytic or statistical methods. Analytic methods consist of backprojection algorithms and the statistical methods from the iterative reconstruction algorithms.

1.7.1 Backprojection

There are two different methods to implement the backprojection algorithms on a computer. The first method is ray-driven backprojection, and the second is pixel-driven backprojection. As the two methods are mathematically identical [12], only ray-driven backprojection will be described. It is worth mentioning that results may slightly be different between the two methods depending on the detail of how weighting factors and interpolations are carried out.

In ray-driven backprojection lines are drawn between the detector pairs which true coincidence events are registered. First, an image matrix typically with a pixel size of 128×128 pixels is defined, and then for each valid LOR, a line is drawn on the image matrix. The value of each pixel V_{pix} that is intersected by the drawn line is equal to

$$V_{\text{pix}} = Nw \tag{1.22}$$

where N is the number of counts detected by the detector pair, and w is the weighting factor proportional to the path length of each intersected line in each pixel, see Figure 1.10.

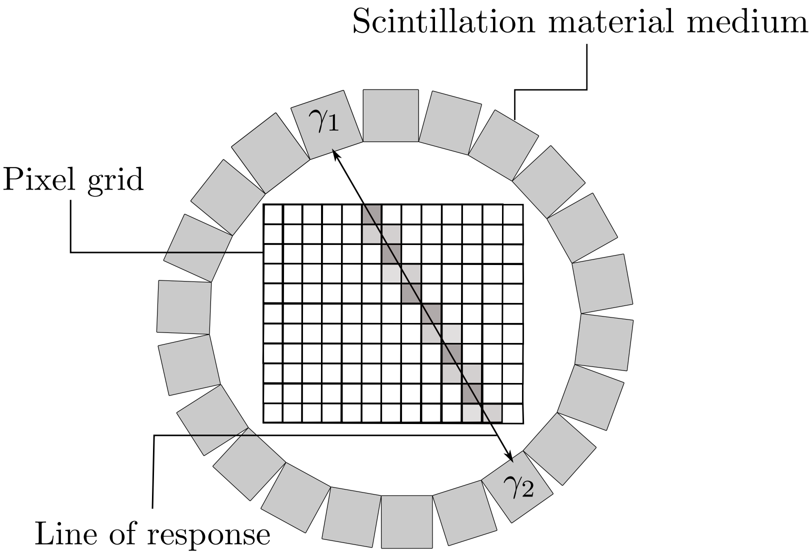

Figure 1.10: Illustration of backprojection image reconstruction. Events detected in a given line of response are placed in the pixels which are intersected by the LOR. The pixel value is determined by the number of lines intersecting each pixel, multiply by a weighting factor based on the path length of the line through each pixel.

Backprojection of the data resembles the true distribution of the radioactivity in the object, but outside of the boundaries of the object, especially seen in complex objects, the images appear blurred. The blurring is propositional to $1/r$, where r is the distance from the object. Mathematically, it can be shown that the relationship between backprojected image $a'(x, y)$ and the true activity distribution in the object $a(x, y)$ is given by

$$a'(x, y) = a(x, y) \circledast \frac{1}{r} \tag{1.23}$$

where $\circledast$ denotes the operation of convolution [13]. To reduce the effect of blurring in the backprojected image, various post-process filters are applied to the backprojected image such as Ramp, Hamming and Hann. These filters improve the contours of the objects under review, and to be more specific in PET imaging; they help to outline the internal structure of the patient (e.g. organs, bones) more precisely.

1.7.2 Iterative Reconstruction Methods

The most widely used method in the iterative reconstruction algorithms is the Maximum Likelihood Expectation Maximisation (MLEM). This method consists of the image space and the projection space. In the image space, an initial estimate of the image is made, typically a uniform distribution where each pixel is equal to one. Next, the reverse method of the backprojection algorithm shown in Section 1.7.1 called forward projection is used, and an estimated image is generated based on the forward projections. This estimated image is transferred to the projection space and is compared with the initial image generated in the image space. Then this estimated image is backprojected into the image space, and the initial image is updated. This process is repeated until a convergence criterion is reached. Because of this repetitive nature of this category of image reconstruction algorithms, the term iterative is given, see Figure 1.11. MLEM algorithm relies on the generation of a "system matrix" [14], which describes the likelihood that a decay in a given pixel will be measured by a LOR. Multiple factors can be added in this probabilistic likelihood matrix such as geometrical factors and the physics of a given radioactive source. The development of suitable approaches to improve the MLEM algorithms is complicated and as a result, is a research field of its own in the medical physics field.

The concept behind MLEM algorithms is that the number of counts in a line of response varies according to a Poisson distribution. The probability of measuring a number of counts m along a line of response i at a given mean of the distribution q, $P_r(m_i|q_i)$ is equal to

$$P_r(m_i|q_i) = \frac{q_i^{m_i} e^{-q_i}}{m_i!} \tag{1.24}$$

The image vector which most likely has yielded the data set m_i is chosen from the MLEM algorithm, and the image is updated. As the image reconstruction based on MLEM is used primarily in data sets which are suffering from low statistics and high noise (e.g. human PET imaging), in this thesis, is not used.

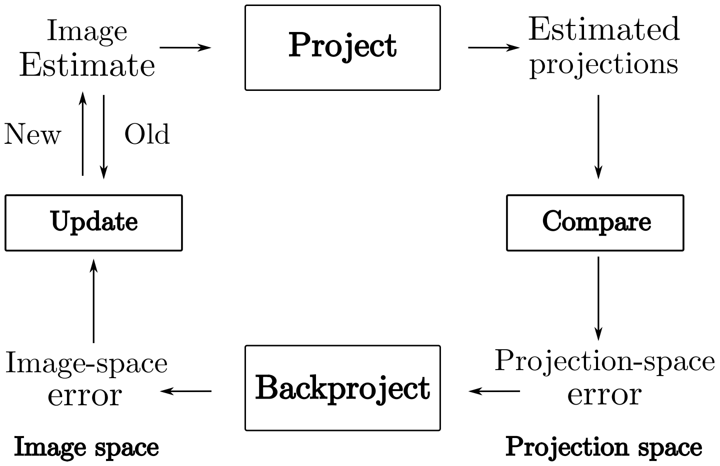

Figure 1.11: Flow chart of a generic iterative image reconstruction process.

1.7.3 Time of Flight (TOF)

Conceptually, TOF is the easiest and most accurate imaging method. It involves the measuring of the time difference in the arrival time of two annihilation photons to the scintillation detectors, see Figure 1.12. The location Δx of an annihilation event with respect to a point at the centre of the PET detector is equal to

$$\Delta x + d_1 = ct_1 \tag{1.25}$$

$$d_2 - \Delta x = ct_2 \tag{1.26}$$

where d_1 is the distance of detector one from the centre, d_2 the distance of detector two from the centre, t_1 and t_2 are the detection times of the annihilation photons from detector one and detector two respectively, and c is the speed of light ($\approx 3.0\times10^8\ m/s$). By subtracting Equation 1.25 from 1.26, Δx is equal to

$$\Delta x = \frac{c\Delta t}{2} \tag{1.27}$$

where Δt is the difference in the arrival time of the two annihilation photons. For example, if an annihilation occurs closer to one detector than the other, this small but measurable delay between the two 511 keV photons allows the accurate localisation of the annihilation event. A typical PET scanner has a diameter of 80 cm and assuming that the annihilation point is almost at the boundaries of one of the detectors, the time difference in the arrival time will be 2.6 ns. However, to calculate this time difference is very difficult because PET detectors have a finite time resolution which arises from the decay time of the scintillation material, and the processing of the output signal from the PMTs or SIPMs. Therefore the use of a coincidence time window which is two or three times larger the maximum arrival time of the scintillation photon is necessary. In modern PET scanners, the TOF is used alongside computed tomography algorithms to narrow the possible location of the annihilation events across the LOR. As already stated in the backprojection section, the image pixels that belong to the same LOR are all incremented, whereas in the TOF reconstruction only the image pixels close to the annihilation events will be incremented. As a result, a better signal to noise ratio is achieved.

To reach the ultimate goal for TOF reconstruction requires the improvement of the time resolution. The reduction of time resolution will lead to the localisation of the annihilation events without the need for image reconstruction algorithms such as backprojection and iterative. A constant search in finding the best scintillation material alongside fast electronics still remains the goal of the medical physics scientific community.

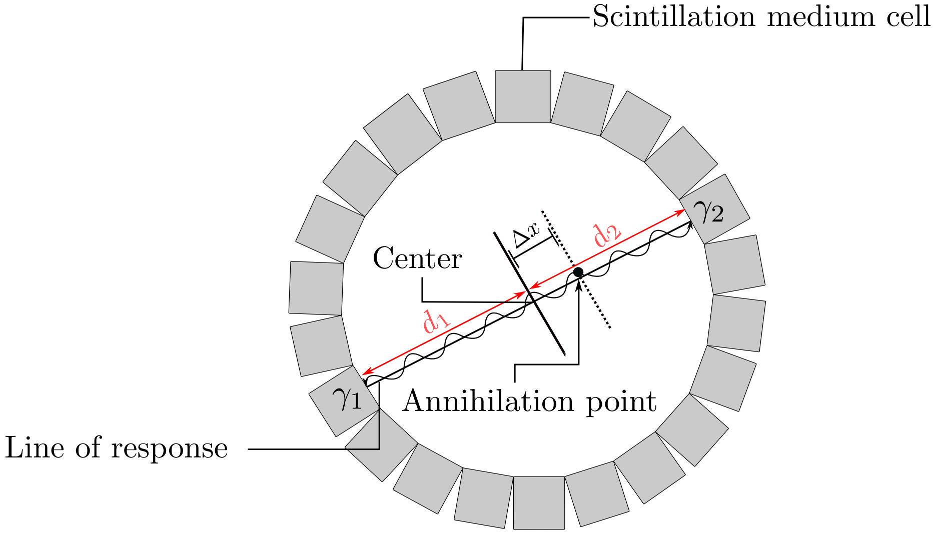

Figure 1.12: Diagram of the time of flight (TOF) feature of PET scanner narrowing the event position along the line of response.

1.7.4 Comparison Between Image Reconstruction Algorithms

As already stated, the image reconstruction method plays a crucial role in converting the collected data into a visual representation of the distribution of positron-emitting radiotracers within the body. Filtered backprojection, iterative image reconstruction, and time-of-flight are the three most widely used image reconstruction methods in PET that offer unique advantages and disadvantages. Filtered backprojection is a traditional approach to image reconstruction in PET, in which the collected data is first filtered and then back-projected onto a two-dimensional image plane to create a preliminary image of the activity distribution. FBP is fast and straightforward, but its image quality can be degraded due to scatter and random coincidence events. On the other hand, iterative image reconstruction uses sophisticated mathematical algorithms to estimate the activity distribution, providing improved image quality with reduced noise levels and spatial resolution. However, this approach is computationally intensive and requires longer processing times. TOF reconstruction uses the time-of-flight information of the gamma rays to improve image contrast and reduce noise levels, especially in regions with high activity concentration. This method requires specialized hardware and timing detectors, which can increase the cost and complexity of PET imaging systems.

The complementary nature of these image reconstruction methods can be exploited by combining them to achieve improved image quality and reduced noise levels in PET imaging. For example, FBP can produce fast preliminary images that are refined using iterative reconstruction, or iterative reconstruction can be combined with TOF information to achieve high-quality images while reducing computation time. Combining these methods makes it possible to take advantage of the strengths of each approach and overcome their limitations, leading to improved image resolution and contrast in PET imaging.

Chapter 2

Liquid Argon Scintillation Detector

As already described in the first Chapter, PET detectors use a scintillation medium to stop the annihilation photons and produce a measurable signal. The amplitude of the signal generated is proportional to the number of the scintillation photons emitted from the scintillation medium. This property is called light yield and is of paramount importance in PET detectors. In section 1.6.2, it was stated that the sensitivity of a PET detector is proportional to the square of the detection efficiency. To increase the detection efficiency, one needs a light yield per keV as high as possible to record a large signal. Also, the high light yield will result in better energy resolution that in turn, will help to reduce the accepted energy window of the coincidence events. Liquid argon has a much higher light yield per keV compared to the scintillation crystals currently used in PET scanners see Section 2.3, and therefore makes it a strong candidate for use in PET detectors.

However, except the high photon yield, a PET photon detector should have a fast scintillation light decay time, a high stopping power, and a low cost. This chapter will describe the physical properties of LAr, and compare them with that of the scintillation crystals used in commercial PET scanners. In addition, in this chapter the physical properties of silicon photomultipliers (SiPMs) will be described as in this thesis are the preferred detectors of use for the detection of the scintillation photons generated by liquid argon. The reason that SiPMs were chosen over PMTs for the detection of the scintillation photons generated by liquid argon will be explained in Section 2.11.

2.1 Liquid Argon Properties

From the family of noble gases, argon (Ar) was the first to be discovered at the end of the 19th century. Argon is an inert gas which is abundant in our atmosphere (9300 ppm). It can be easily isolated by fractional distillation of liquid air. Argon name is derived from the Greek word αργό which means “slow” or “inactive”. In the Earth atmosphere, four isotopes of Ar exist. Three of them are stable ^{40}Ar (99.6%), ^{36}Ar (0.34%), ^{38}Ar (0.06%) and one unstable ^{39}Ar. The unstable isotope is a beta emitter which is created through the interaction of cosmic rays and ^{40}Ar. The activity of ^{39}Ar is estimated to be 1 Bq/kg with a half-life of 269 days. Table 2.1 list argon physical properties [16] and Figure 2.1 illustrates argon phase diagram.

Argon physical properties	Value
Atomic number	18
Atomic weight	39.94
Dielectric constant	1.6
Boiling point at 1 bar (K)	87.15
Triple point temperature (K)	83.78
Latent heat of vaporization (J/g)	161.10
Ionisation density (eV)	15.76
Radiation length (cm)	14.2
Liquid density at 1 bar (g/cm^3)	1.39
Expansion ratio of liquefied argon (l)	1:800

Table 2.1: Physical properties of Argon [16]

.

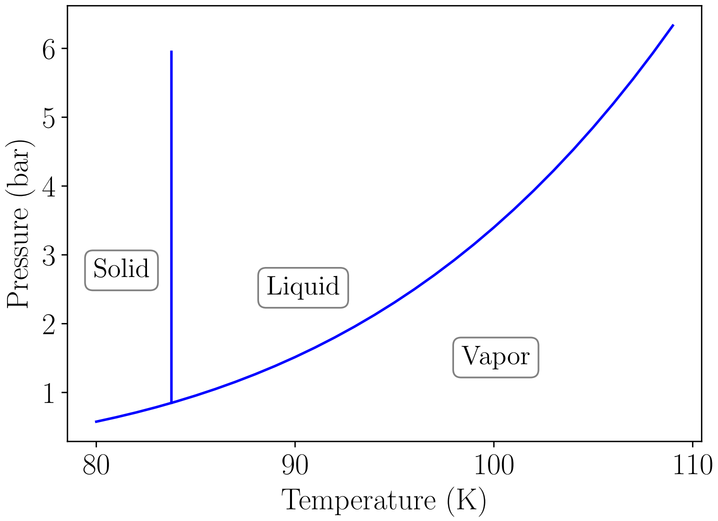

Figure 2.1: Phase diagram of argon showing the solid, gas and liquid state based on pressure and temperature. Plot was generated with data acquired from references [26] and [27].

2.2 Scintillation Mechanism

When an ionising particle interacts with liquid argon, it produces scintillation light. The wavelength of this scintillation light is 128 nm (9.7 eV) with a FWHM ≈6 nm [17]. Throughout the collision of the ionising particle with LAr, the recoiling particle either excites or ionises the surrounding argon atoms. This excitation or ionisation, form excimers Ar_2^* (excited dimers). These excimers through the "self-trapping" process which occurs in few picoseconds [18] scintillate producing vacuum-ultraviolet photons. The processes which form the excimers are

- Excitons-Neighbouring argon atoms

$$\mathrm{Ar}^* + \mathrm{Ar}\ (\text{self-trapping}) \rightarrow \mathrm{Ar}_2^* \rightarrow 2\mathrm{Ar} + \gamma\ (128\ \mathrm{nm}) \tag{2.1}$$

- Recombination of Ar_2^+ and thermalised secondary electrons

$$\begin{gathered}\mathrm{Ar}^+ + \mathrm{Ar} \rightarrow \mathrm{Ar}_2^+ + e^- \rightarrow \mathrm{Ar}^{**} + \mathrm{Ar} \rightarrow \mathrm{Ar}_2^{**} \rightarrow Ar^* + \mathrm{Ar} + \text{heat} \\ \mathrm{Ar}^* + \mathrm{Ar} \rightarrow \mathrm{Ar}_2^* \rightarrow 2\mathrm{Ar} + \gamma\ (128\mathrm{nm}).\end{gathered} \tag{2.2}$$

The average number of electron-hole pairs N_{ion} produced through the absorption of energy E inside liquid argon is

$$N_{\text{ion}} = \frac{E}{W_{\text{ion}}} \tag{2.3}$$

where W_{ion} is the ionisation energy and is equal to 23.6 eV. The ratio between the number of excited atoms N_{ex} and number of ions N_{ion} is equal to 0.21 [19]. The maximum number of scintillation photons emitted N_{ph} is equal to the sum of the number of ions and the number of the excited atoms produced by an ionising particle

$$N_{\text{ph}} = N_{\text{ion}} + N_{\text{ex}}. \tag{2.4}$$

By equating Equations 2.3 and 2.4, the average energy needed to produce a scintillation photon W_{ph} is

$$W_{\text{ph}} = \frac{W_{\text{ion}}}{\left(1 + \frac{N_{\text{ex}}}{N_{\text{ion}}}\right)} = 19.5\ \text{eV}. \tag{2.5}$$

Excimers are produced in two singlet states and one triplet state. The difference between them is that the former has its electrons paired (anti-parallel) and the latter has its electrons not paired (parallel). The multiplicity rule defined as $2S{+}1$, where S is the sum of the particles spin. The multiplicity for a singlet state is equal to one ($S = 0$), where for a triplet state the multiplicity equals three ($S = 1$). Through the transition between these states, a photon is emitted, but first, a series of selection rules must be valid as not all transitions are allowed to emit light. These selection rules are [20]:

1. The total orbital angular momentum L should be either equal to 0 or ±1.
2. When an electrons transits between states, the total spin must not change (ΔS=0). However, this rule does not apply for heavy atoms such as argon, and therefore the Russell-Saunders notation is no longer an adequate representation, due to the strong spin-orbit coupling (LS).
3. Parity must be conserved. Parity is defined based on the symmetry of the molecule with respect to a reflection at any plane through its internuclear axis. When it is symmetric at any plane of reflection, the sign + is used, whereas when it is not, the − sign is used. Therefore, an allowed transition is $+ \to +$ or the $- \to -$. It must be noted that for homonuclear molecules only orbital transitions of $g \to u$ and vice versa are allowed. The symbols g and u are notations taken from the German words gerade and ungerade, and in English means even and odd respectively. If an inversion through the centre of a molecule results in a phase change, the molecule is said to be in an ungerade orbital. On the other hand, when there is no phase change, it is said to be in a gerade orbital. For example, when a p orbital with the two characteristic lobes is inverted through its centre of symmetry, the two lobes change phase (+ and −), and the orbital is said to be ungerade.

As already stated, when liquid argon atoms are excited, two singlet states are produced ${}^1\Sigma_u^-$, ${}^1\Sigma_u^+$ and one triplet ${}^3\Sigma_u^+$. Through the transition of this states to the ground state ${}^1\Sigma_g^+$ scintillation light is emitted. However, the singlet state ${}^1\Sigma_u^-$ does not emit light as the parity is not conserve($- \to +$). The decay of ${}^1\Sigma_u^+ \to {}^1\Sigma_g^+$ is strongly allowed and occurs in 6 ns. On the other hand, the decay of ${}^3\Sigma_u^+ \to {}^1\Sigma_g^+$ occurs in 1.6 µs [19] because the decay to two spin-0 argon atoms takes longer. For a light particle such as electron and photon, the ratio between the singlet and triplet state is equal to 1/2, whereas for heavier particles is 4/5 [21].

If no quenching is taken into account, the photon yield in LAr is equal to 51 photons/keV. This number is reduced relative to the Liner-Energy-Transfer (LET). When the scintillation loss is on the low-LET side, it can be explained by electron escaping recombination, whereas, for high-LET particles, a mechanism called core-penumbra is proposed by Hitachi and Doke [22]. At 511 keV which is the energy of interest, ARIS collaboration evaluated LAr light yield relative to the absolute value using a ^{22}Na radioactive source and found that quenching effects are negligible, assuming LAr is pure and not contaminated [23].

Lastly, its worth noting that the energy needed to excite an electron in LAr from the valance to the conduction band is 14.3 eV [24], see Section 2.4. As the energy of the scintillation light emitted from LAr is equal to 9.7 eV, one can say that argon is transparent to its own scintillation light.

2.3 LAr vs Scintillation Crystals

The requirements that a PET photon detector should have are (a) a high photon yield, (b) a high stopping power, (c) a fast scintillation light decay time and (d) a low cost. A liquid argon (LAr) detector potentially could improve on existing detectors in all of these key requirements. The most common scintillation detectors used in PET scanners are Bismuth Germanium Oxide (BGO), Lutetium-Yttrium Oxyorthosilicate (LYSO) and Lutetium Oxyorthosilicate (LSO). A comparison between the most popular scintillation crystal used in PET scanner and LAr is shown in Table 2.2.

One of the properties of LAr which distinguishes it from the existing scintillation crystals is light yield. LAr has a light yield of 51 photons/keV, whereas BGO, LYSO and LSO have 9, 25 and 30 photons/keV, respectively [25]. To record high signals, one needs a light yield as high as possible. This will increase PET detectors sensitivity, see Section 1.6.2. As shown in Table 2.2, LAr density is approximately five times smaller than that of the scintillation crystals used in most commercially available PET scanners. Therefore, the stopping power of these crystals is higher than that of LAr. However, this can be mitigated by increasing the length of the stopping medium, as described further in Chapter 3. All new commercially available PET scanners have implemented the TOF feature, see section 1.7.3, as by using scintillation detectors with fast decay time will improve the annihilation photons localisation, and therefore the quality of a PET image. By using detectors with fast decay time, it will lead to an image which only pixels close to the annihilation events are incremented, and not all the pixels along the LOR. The LAr fast decay time is 1.6 ns, whereas, for BGO, LYSO and LSO is 300 ns , 40 ns and 40 ns respectively. Lastly, as argon is abundant in our atmosphere is very cheap to buy (£1 per cubic centimetre) [40]. However, a possible estimate of the cost of a complete LAr based detector was not performed in this thesis.

Material	Density (g/cm^3)	Light yield (photons/keV)	Decay time (ns)
BGO	7.13	8	300
LSO	7.40	30	40
LYSO	7.15	25	40
LAr	1.39	51	fast: 6 slow: 1600

Table 2.2: Physical properties comparison between typical scintillation crystals used in PET scanners with LAr [25].

2.4 Silicon Photomultipliers Physics

A silicon photomultiplier (SiPM) is a semiconductor photodetector that produces a signal in response to absorption of a photon. In addition, to the acronym SiPM there are many other acronyms used in the literature, such as Multi-Pixel Photon Counter (MPPC), Geiger-mode Avalanche Multi-Pixel Photo-diode (GAMPD) which refer to semiconductor photon detectors. Throughout this thesis, the term SiPM and MPPC will be used interchangeably. Before describing how SiPMs can be used in PET imaging, an understanding of their physical properties and structure is crucial.

An atom consists of a nucleus and the orbital electrons. These electrons occupy discrete energy levels, and the outermost orbital electrons are called valance electrons. For all atoms except noble gases, the outermost level which houses the valance electrons has free states into which electrons can participate in the formation of chemical bonds. Materials such as crystals have atoms in close proximity, and as a result, electrons can move into the neighbouring atoms orbital. In solid-state physics to better describe the properties of each material, the concept of energy bands is used. The two distinct energy bands are (a) the valance band which consists of electrons which are tightly bound to the parent atom, and (b) the conduction band which comprises from loosely bound electrons which can move within a material.

To characterise the electrical conductivity of a material, the gap between the highest occupied energy state of the valence band and the lowest unoccupied state of the conduction band is used [28], called band gap. The band gap represents the amount of energy required to excite a valance electron from the valance band to the conduction band. When this gap between the valance band and the conduction band is large, a material is called an insulator, whereas when the band gap is small, the material is called a semiconductor. Lastly, one more type of material exists called metal. Metals have the conduction band and valance band overlapping, and electrons can readily jump between the two bands and that makes them highly conductive. SiPMs belong to the category of semiconductors which is an intermediate between metals and insulators. By using the above basic description of energy bands, is now possible to describe the advancements around the construction of SiPMs and how they are used in PET imaging.

2.5 The PN Junction

In a semiconductor, charge carriers are electrons and holes. Electrons have a negative charge and holes have a positive charge. When a loosely bound electron is promoted from the valance band to the conduction band it leaves an empty state behind (in valance band) called hole. Electrons of valance band, occupy this empty state leaving a hole in their original location. As a result, holes act as charge carriers during their movement in the valance band.

As their name indicates, SiPMs are fabricated using silicon crystals. The collection of charge carriers in SiPMs results in an electrical signal. Therefore, the optimization of this charge carriers collection is of paramount importance. When a silicon crystal has the highest level of purity, the number of negative (electrons) and positive (holes) charge carries is equal. This state is called intrinsic, and the collection of charge is insufficient. Doping a silicon crystal with elements of different band structures (impurities) adds extra charge carries. Silicon has four outermost electrons and therefore, it can form covalent bonds with four neighbouring atoms. Adding an element with five outermost electrons into the silicon crystal, results in the formation of four chemical bonds with the valance electrons of the surrounding silicon atoms leaving one unbound electron, see Figure 2.2b. As these elements contribute extra unbound electrons to the silicon crystal they are called donors. Typical donor elements are phosphorus and arsenic. On the other hand, when elements with three outermost electrons are introduced to the silicon crystal, a local electron deficiency is observed. The reason is that the three valance electrons can only form covalent bonds with the three neighbouring silicon atoms leaving an electron-hole available, see Figure 2.2a. This type of elements are called acceptors. Typical acceptor elements are boron and gallium.

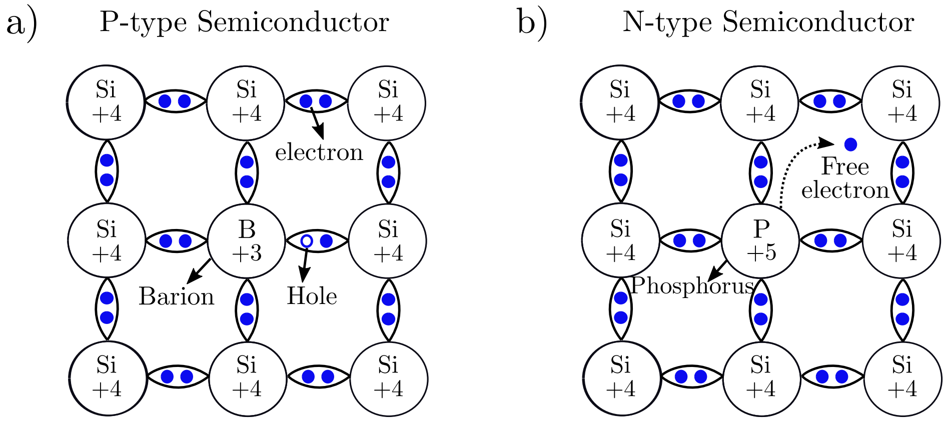

Figure 2.2: Schematic of a P-type and N-type doped semiconductor: a) for a P-type semiconductors only three valance electrons can form covalent bonds with the neighbouring silicon atoms leaving an electron-hole available (typically boron atoms are used as acceptors), b) for N-type semiconductors four valance electrons form covalent bonds with the four neighbouring silicon atoms leaving a free-electron available (typically Phosphorus atoms are used as donors).

A doped semiconductor with an excess of electrons is called N-type, whereas when it is doped with an excess holes is called P-type. When a P and N type semiconductors are joined, the interface between the two differently doped regions forms the basis of a semiconductor device. The two regions have a different concentration of electrons and holes, and as a result, electrons are diffused from the N-side to the P-side, and likewise, holes are diffused from P-side to the N-side, see Figure 2.3b. These charge carriers are recombined by the available holes or electrons in the P and N side, resulting in an interface which contains no charge carries. This region is called the depletion region or depletion layer, see Figure 2.3a. Due to the drift of the charge carriers, the N-side of the depletion region becomes positively charged, whereas the P-side turns into a negatively charged, see Figure 2.3c. Inside the depletion region, an electric field is created, see Figure 2.3d, and therefore a potential barrier referred as built-in voltage is created. Lastly, due to the carriers diffusion and therefore the separation of charge, the electric field generated opposes any further carriers diffusion. that electric field opposes further carrier diffusion due to the separation of charge, see Figure 2.3e.

The depletion region width is important during the fabrications of a SiPM as it affects the photosensitivity and frequency response of the SiPM. Smaller photon wavelengths are absorbed in shallower depths within the depletion layer, and therefore by reducing the depletion region's width the SiPM's photosensitivity increases. Inversely, when a SiPM has to be sensitive at long wavelengths, a wider depletion layer is fabricated. The width of a depletion region W_{dep} is described by

$$W_{\text{dep}} = \sqrt{\frac{2\epsilon}{q_e}\left(\frac{1}{N_A} + \frac{1}{N_D}\right) V_b} \tag{2.6}$$

were ϵ is the permittivity, q_e the electric charge of the electron, N_A the concentration of acceptors, N_D the concentration of donors, and V_b the built-in voltage.

In a silicon semiconductor, when the depletion region is exposed to photons with energies greater than the silicon band gap, which is 1.14 eV a photon current is created (between the P and N region). Unquestionably, electron-hole pairs can be created outside the depletion region due to the photoelectric effect. However, this charge carries have short lifetimes and undergo recombination before they can reach the depletion region.

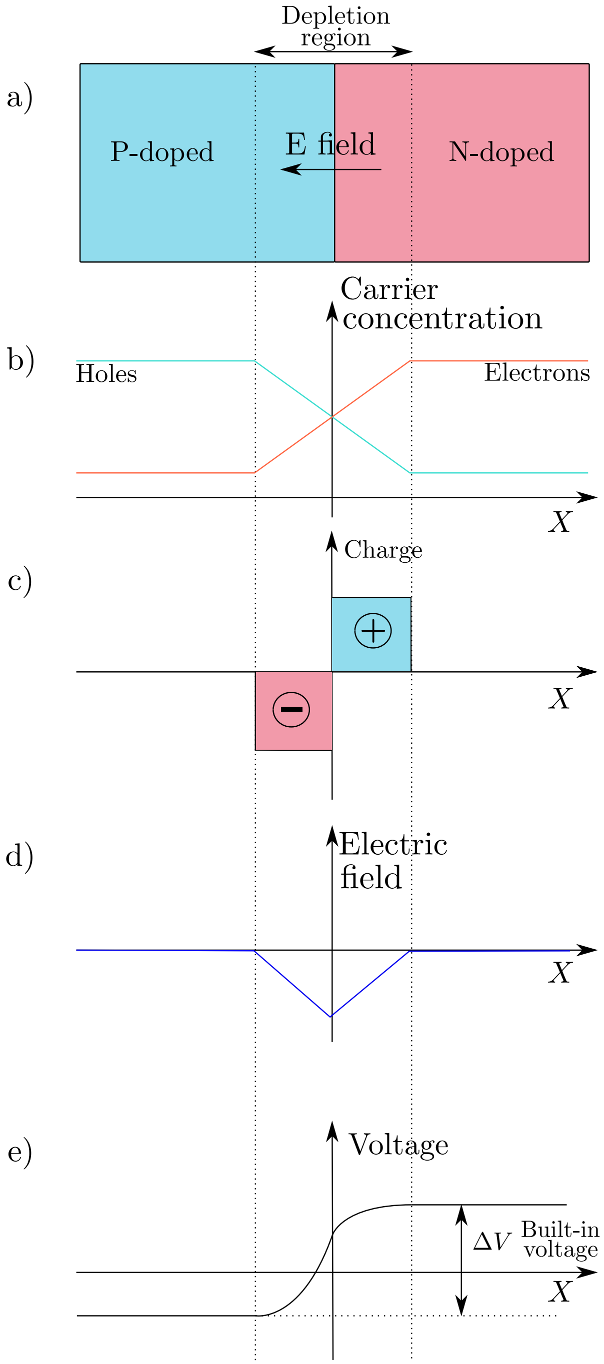

Figure 2.3: Schematic showing the PN's junction properties under equilibrium: a) depletion region representation created by joining the two semiconductor types, b) Illustration of the diffusion of electrons from N-side to the P-side and likewise the diffusion holes from P-side to the N-side, c) the N-side of the depletion region becomes positively charged after the diffusion of carriers, whereas the P-side turns into a negatively charged, d) electric field strength across a PN junction, e) potential difference across the depletion region of a PN junction caused by the charged carriers.

2.6 Applying Bias Voltage to the Junction

To reduce the potential barrier across a PN junction, a positive electric field must be applied to the P side of the junction. Consequently, this reduction of the potential barrier will reduce the width of the depletion layer as the applied positive electric field opposes the initial electric field. This method is called forward biasing. The effect of the forward biasing in a PN junction is the increase in carrier diffusion, causing an immediate increase in the current flow, see Figure 2.4.

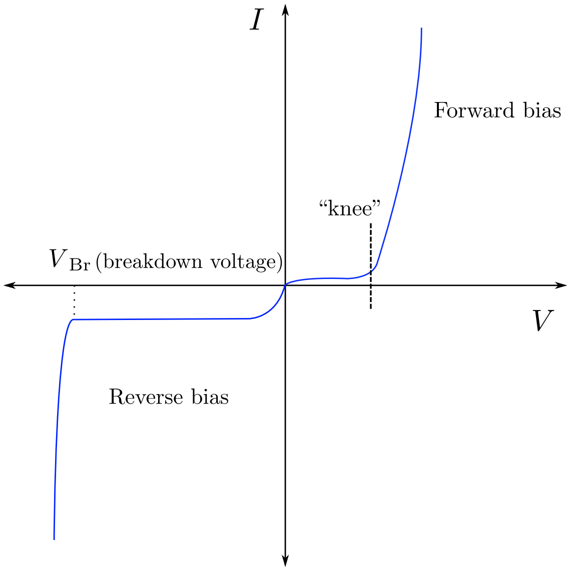

Figure 2.4: Conceptual plot showing the current as a function of the applied bias voltage in a PN junction. The forward biasing voltage on a junction causes the depletion layer to become narrow, which creates a low resistance path that allows for a significant increase in current flow. This increase in current is shown on the curve as "knee" point. The reverse biasing voltage on the junction increases the width of the depletion layer, creating a high resistance path that restricts the flow of current. On the curve, this restriction in current flow is represented as a flat region before the voltage reaches the reverse breakdown voltage.

Contrarily, to increase the potential barrier across the PN junction, a positive electric field must be applied to the N side of the junction. As a result, the potential barrier will increase across the width of the depletion region. This regime is called reversed biasing. In reverse-biased PN junction, due to the high potential barrier, almost no current is flowing in the junction (small current amount can be measured because of the minority charge carriers left in P and N region of the junction). However, after a certain voltage called breakdown voltage, the potential barrier breaks and the current flow increases exponentially, see Figure 2.4.

There are two modes of breakdown in a PN junction (a) the avalanche breakdown and (b) the Zener breakdown. As SiPMs are avalanche photodiodes, only the avalanche breakdown mode will be described. During an avalanche breakdown, the electric field strength across the PN junction is such that the charge carriers are accelerated enough to cause impact ionisations. This impact ionisation effect results in a carrier multiplication phenomenon by which the number of drifting carriers increases exponentially, resembling an avalanche. An in-depth mathematical analysis of the respond of semiconductor in external biassing can be found in references [29], [30].

2.7 Geiger-mode Amplification and Quenching

The applied reverse bias voltage is strongly associated with the gain of a photodiode. At low bias voltage, the gain is in the order of 10, whereas at high reverse biasing it can be 100-1000 times greater. This is due to the impact ionisations. The dominating source of gain comes from the avalanche multiplication, and therefore the device is called Avalanche Photo-Diode (APD). It is feasible to fabricate a device which operates above the breakdown voltage, see Figure 2.5, of the PN junction and that device, is said to be operating in Geiger mode.

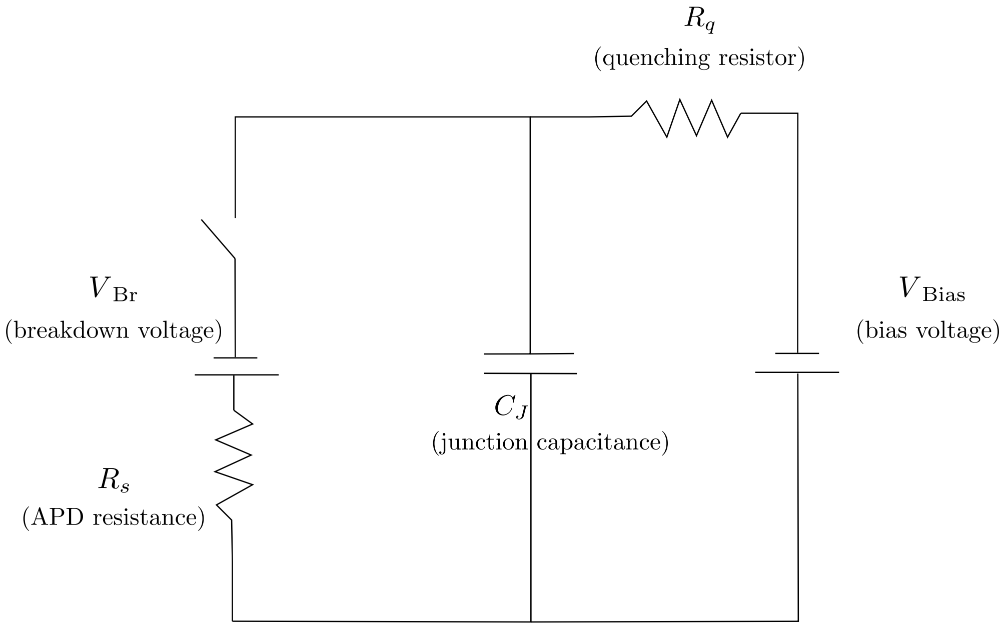

Figure 2.5: Equivalent circuit of a Geiger-mode APD.

In Geiger mode, the electric field is strong enough to accelerate electrons and holes, and in addition to the primary impact ionisations, secondary impact ionisations are produced. As a result, a very large current flows in the PN junction. However, the PN junction saturates rapidly due to the current heating of the junction. This rapid increase in the temperature of the photodiode can permanently damage the device. Thus, Geiger mode APDs are quenched using a resistor (R_q), and the bias voltage (V_{Bias}) drops below the breakdown voltage (V_{Br}). In the conceptual circuit shown in Figure 2.5, the GAPD junction capacitance (C_J) is initially biased V_{Bias} whilst the switch is open. When an electron-hole pair is generated in the depletion region, the switch closes, and the GAPD capacitance starts to discharge through the GAPD's resistance (R_s). The value of R_s is small and allows a surge of current flow. Then the potential difference across the junction capacitance exponentially decays towards the breakdown voltage, and the avalanche process weakens. This is due to the two opposing current loops, one entering C_J to recharge it and one leaving the C_J to discharge it. When the value of the quenching resistor (R_q) is large enough so that the current flow from the bias voltage cannot sustain the junction's capacitance discharge, the avalanche process is quenched.

The maximum current flow in GAPD I_{max} can be described by

$$I_{\text{max}} = \frac{V_{\text{Bias}} - V_{\text{Br}}}{R_q + R_s} \tag{2.7}$$

where V_{Bias} is the bias voltage, V_{Br} the breakdown voltage, R_q is the quenching resistor, and R_s is the series resistance. Figure 2.6 shows the current as a function of time. The amount of charge Q in a current pulse is approximately equal to I_{max} multiplied by the characteristic time τ. The gain μ can then be calculated by

$$\mu = \frac{Q}{e} = \frac{I_{\text{max}}\tau}{e} = \frac{V_{\text{Bias}} - V_{\text{Br}}}{e(R_q + R_s)} \cdot R_q C_J \tag{2.8}$$

where e is the electron charge, and τ is the characteristic time constant and is equal to $R_q C_J$. It is worth noting that the junction capacitance C_J purely depends on the MPPC manufacturing design.

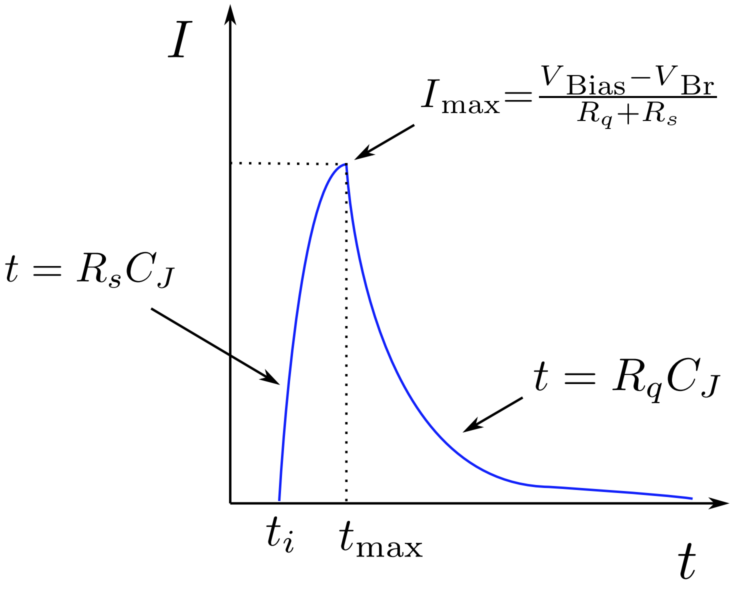

Figure 2.6: Conceptual current pulse of Geiger-mode APD as a function of time. The current pulse begins at t_i and rapidly increases until it reaches the maximum value $I_{\max}$. At $t_{\max}$ the bias voltage is not enough to sustain the junction's capacitance discharge, and the APD begins to discharge.

2.8 Geiger-mode Avalanche Multi-Pixel Photon Counter

Based on the information in the previous sections, it is now possible to describe the Geiger-mode avalanche Multi-Pixel Photon Counter (MPPC) which is the device used in this work. A MPPC is an array of identical APDs called microcells or pixels which are connected to a common-bias and common-output matrix, see Figure 2.7. Depending on the device, the size of a microcell varies from 10 µm to 100 µm and the number of microcells per device ranges from several hundred to several tens of thousands. Although pixels in a MPPC have a common readout, they can undergo an independent discharge and reset, without affecting the whole device due to their separate quenching resistor. However, to have an efficient carrier collection, optical trenches are used to separate each pixel. In Section 2.10, the benefit of this optical trenches will be explained. Examples of SiPM topological designs can be found in references [31], [32]. The SiPM used in this thesis was acquired from Hamamatsu, and details in their topological design can be found in their catalogue [33].

The total charge output of a MPPC is given in quantised units called photoelectrons or pixel triggers N_{triggers} . Each pixel is assumed to be identical, and therefore the total charge output Q_{total}

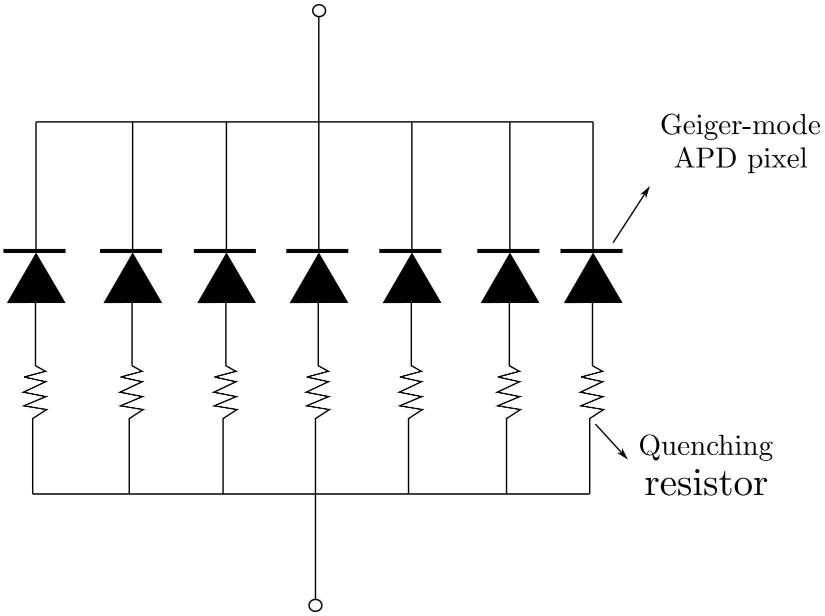

Figure 2.7: Conceptual diagram of a MPPC as a matrix of GAPD pixels connected in parallel.

is equal to

$$Q_{\text{total}} = \sum_{i=1}^{N_{\text{triggers}}} Q_i \ . \tag{2.9}$$

The gain of a MPPC is in the order of 10^7. Figure 2.8 shows the gain of a MPPC as a function of overvoltage (voltage above the breakdown voltage). The data shown in Figure 2.8 are taken during the characterisation of the MPPC S13370-6050CN [34], which is the device used in this thesis. The gain of a MPPC is temperature-dependent when the bias voltage is changing. When the fixed bias voltage increases, the temperature of the MPPC will inevitability increase as well, and as a result, the breakdown voltage will also increase. However, when it is operated at constant overvoltage, the gain remains constant through a large range of temperatures [33].

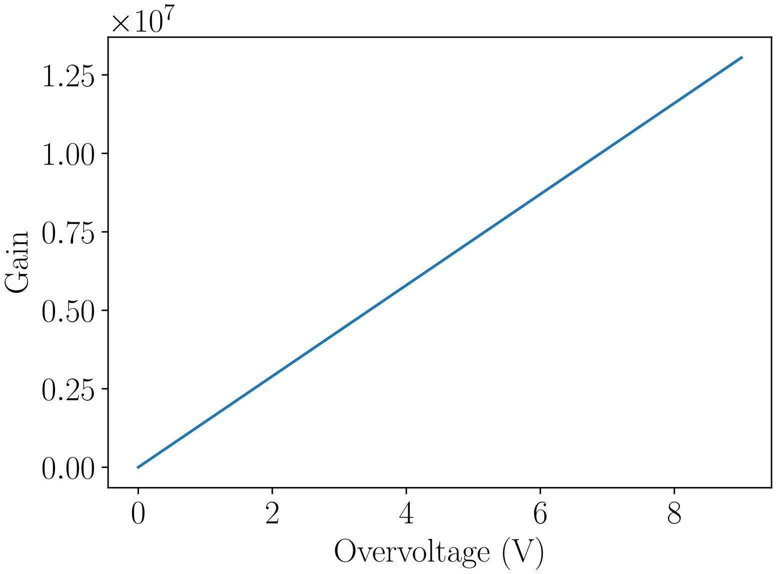

Figure 2.8: Plot showing the gain as a function of overvoltage in a Hamamatsu MPPC S13370-6050CN. Data are acquired during the characterisation of the Hamamatsu MPPC used in this thesis.

2.9 Photon Detection Efficiency

The majority of photon detectors use the term quantum efficiency (QE) to define the ratio of the number of detected photons by the number of incident photons. In PMTs the quantum efficiency depends on the efficiency of a photo-cathode to generate through the photoelectric effect photoelectrons , which in turn this photoelectrons will undergo an avalanche amplification. The typical peak of QE in PMTs is between 10 to 20%. However, recent developments manage to increase their QE to 38% [35]. In contrast, semiconductor detectors have been fabricated with a QE peak of 80% [36].

For MPPCs a different approach is used to define their probability to produces an output signal in response to an incident photon. Although it is feasible to manufacture a single APD with a quantum efficiency as high as 80%, this will not be possible for a MPPC. As already stated, a MPPC is a series of thousands of APD with a common-bias, a common-voltage and an independent quenching resistor. This configuration increases the gain but reduces the number of detected photons. Hence, the term Photon Detection Efficiency (PDE) is used to define the probability that a MPPC will produce an output signal in response to an incident photon, and can be described by

$$\mathrm{PDE}(\lambda, V) = \mathrm{QE}(\lambda) \cdot \sigma(V) \cdot \mathrm{GE} \tag{2.10}$$

where QE is the quantum efficiency, σ is the avalanche probability, GE is the geometrical efficiency or also called geometrical fill factor, λ is the wavelength of the indecent photons and V the overvoltage.

For a MPPC, QE is the probability that an incident photon produces a charge carrier (electron or hole) capable of triggering Geiger discharge in the avalanche section of the depletion region. For better optimisation (higher QE), through Beers-Lambert law, a MPPC can be designed to absorb light in the depletion layer of the desired range of wavelengths (λ). The avalanche probability is defined as the probability charge carriers in the depletion region have enough kinetic energy to induce impact ionisation to the silicon atoms of the MPPC. The likelihood of that scenario depends on the strength of the electric field, which depends on the overvoltage and the width of the depletion region, which also depends on the overvoltage. Lastly, the geometrical fill factor is the fraction of the photosensitive area of the MPPC to the non-photosensitive area. As already stated, to separate the arrays of APDs in a MPPC optical trenches are used. However, these optical trenches reduce the photosensitive area of the SiPM. The area occupied by the optical trenches in a MPPC is considered as"dead space", but their role is of paramount importance in the noise reduction of the MPPC, see Section 2.10.

2.10 Noise

The main factor of noise contribution in a MPPC is (a) the dark current, (b) the after pulses and (c) the optical crosstalk. Dark current is observed in a MPPC due to the small band gap of silicon which is equal to 1.14 eV. An electron can be excited from the valance band to the conduction band via thermal excitation, without the presence of an incident photon. That occurs when charge carriers are generated from thermal excitation, and are excited close to the depletion region of the APD, and in turn manage to produce an avalanche. Moreover, as overvoltage increases the temperature of the MPPC, the dark noise in the detector increases as well. The dark count rate DCR of a MPPC can be described by

$$\mathrm{DCR} = \frac{I_J}{e\mu} \tag{2.11}$$

where I_J is the current flowing in the MPPC, e the charge of the electron, and μ the gain of the MPPC. Figure 2.9 shows the dark current as a function of the bias voltage in the Hamamatsu MPPC used in this thesis. From 52 V and onwards, the dark current increases as the overvoltage (voltage above the MPPC's breakdown) increases.

Noise from after pulses occurs when a small portion of avalanching carriers gets trapped into the impurities of the silicon lattice. As a result, they are released after a short delay (typically between 1-10 ns) upon receiving the necessary energy to jump to the conduction band or valance band. Upon the de-excitation of these carriers, a new avalanche pulse is produced, which appears with a short delay after the genuine parent pulse, see Figure 2.10. Hence this kind of noise is called afterpulse. When an afterpulse is released during the recovery time of the MPPC, its amplitude will be shorter

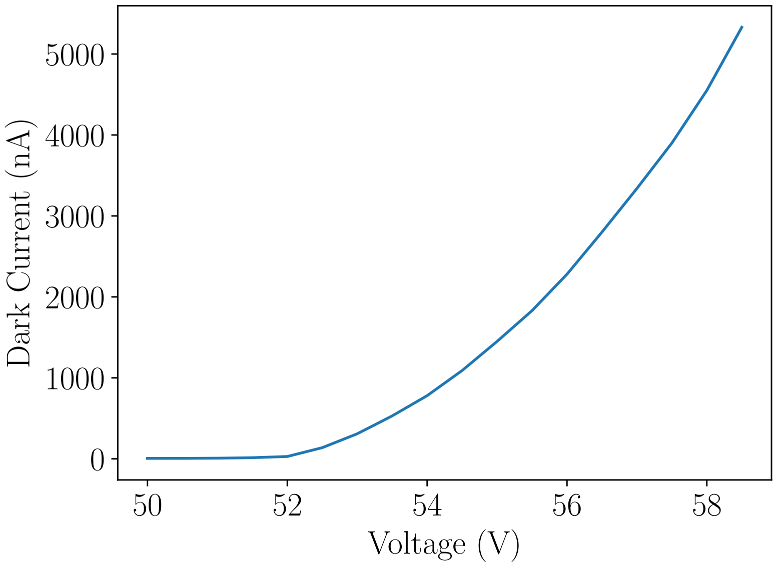

Figure 2.9: Plot showing the dark current as a function of bias voltage in a Hamamatsu MPPC S13370-6050CN. At 52V the overvoltage of the MPPC is started. Data are acquired during the characterisation of the Hamamatsu MPPC used in this thesis.

than a regular photoelectron pulse, and therefore it can be discriminated and filterd out during the pulse analysis. On the other hand, if the afterpulse is produced after the recovery time of the MPPC, it will be indistinguishable of the genuine parent pulse.

Lastly, optical crosstalk occurs when without the presence of an external incident photon, pixels in the MPPC absorb photons (successful carrier multiplication) generated from neighbouring pixels. These photons usually are produced due to phonon vibrations. Accelerated carries do not always contribute to carrier multiplication, and during their scattering collisions with neighbouring silicon atoms, energy is lost as heat due to phonon vibrations. There are two kinds of optical crosstalk, the prompt crosstalk and the delayed crosstalk. Prompt crosstalk occurs when a photon produces an electron-hole pair in the depletion region of a neighbouring pixel and triggers an avalanche process, and its output pulse appears simultaneously with the original pulse. If the MPPC is not used in single-photon counting mode, there is no way to discriminate the crosstalk events from the genuine events, see Figure 2.10. Moreover, the delay crosstalk takes place when a crosstalk photon creates an electron-hole pair outside the MPPC's depletion region. By diffusion, these charge carriers enter the depletion region, and a delay avalanche is produced compared to the original pulse. These delayed pulses can be excluded during the output pulse analysis. The effect of the crosstalk can be substantially diminished when optical trenches are used around each APD in a MPPC. Optical trenches can block this crosstalk photons, but as already stated, optical trenches reduce the geometrical fill factor of a MPPC.

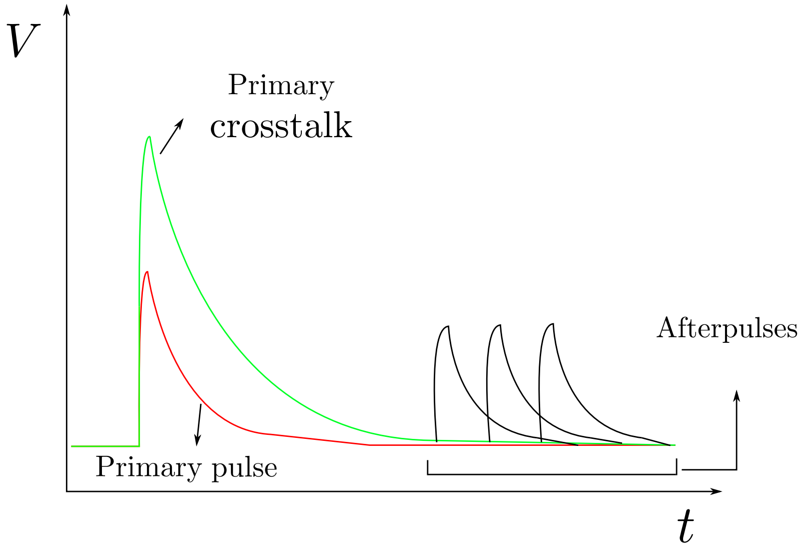

Figure 2.10: Plot of voltage as a function of time in an output signal of a MPPC. Pulses from afterpulse are recorded with short delay and when their detection is occurred during the recovery time of the MPPC its amplitude is reduced. Crosstalk photons detected simultaneously with the primary pulse are indistinguishable and as a result it appears as two photoelectrons.

2.11 PMTs vs SiPMs

Both PMTs and SiPMs can be used to detect the scintillation light generated from the scintillation detectors. However, depending on the situation, one detector can perform better than the other. Therefore, a comparison between the two detectors will be made relevant to a PET imaging scanner. PMTs and SiPMs have a comparable gain, which is in the order of 10^6-10^7. However, the QE or PDE at 128 nm of photon wavelength (LAr scintillation light wavelength) is different. PMTs which are sensitive to vacuum ultraviolet wavelengths have a QE which is smaller than that of the SiPMs. Such PMTs use a photo-cathode made from Beryllium Oxide (BeO) and a window made from Magnesium Floride (MgF_2). At 128 nm, the QE of these PMTs is approximately 5% [37], whereas the PDE of the Hamamatsu MPPC used in this thesis is 14%, see Figure 2.11.

PMTs operating voltage is between 500 to 3000 V, in contrast with the SiPMs which is between 55 to 65 V. The reason that PMTs require this high voltage, is because this voltage is divided between the dynodes which are the contributors of the amplification process, see Section 1.4. SiPMs, as

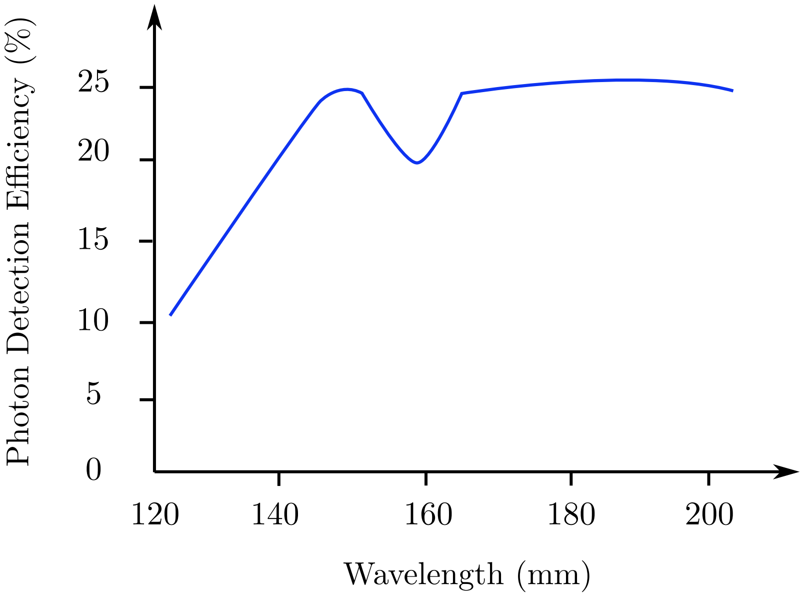

Figure 2.11: Plot showing the PDE as a function of wavelength. The red line shows the PDE of the MPPC used in this thesis. The plot is taken from Hamamatsu MPPC product information [34].

described in Section 2.6, require a few volts above their breakdown voltage to produce an avalanche multiplication.

As PMTs are made from glass, their mechanical robustness is not comparable with that of the SiPMs which are made from mechanically rugged semiconductors. Also, common PMTs are affected by external magnetic fields, whereas SiPMs are immune. Although specially designed PMTs which are immune to extremal magnetic fields exits, their price increases depending on the level of shielding required [38], and that is not ideal when thousands of PMTs are needed (e.g. PET scanner). As already stated in Section 1.6.1, PET detectors have poor spatial resolution. To compensate for these "low" quality images, PET detectors can be used alongside Magnetic Resonance Imaging (MRI). Consequently, photon detectors immune to external magnetic fields are preferred.

PMTs dark count rate (DCR) is small compared to that of SiPMs. PMTs typical dark count rate at ultraviolet wavelengths is ten counts per second [39] whereas in SiPMs is in the order of million [34]. However, temperature plays a significant role in the dark count rate, and therefore submerging the SiPM in LAr results in a negligible dark count rate. Assuming a MPPC with minimal lattice imperfections, the major contribution to the DCR is crosstalk (phonon vibrations). As already stated, accelerated carriers do not always contribute to carrier multiplication, and during their scattering collisions with neighbouring silicon atoms, energy is lost as heat. In this project, the SiPMs will be submerged in LAr, which has a boiling point of 87.15 K, the dark count rate is negligible due to minimal lattice (i.e phonon) vibrations.

Lastly, the cost of the two detectors varies with their size. This factor is of great importance when designing photon detection systems. For example, if a sizeable photosensitive area is required for an experiment, PMTs due to their large size are going to be a cost-effective choice. However, if a small photosensitive area is required, SiPMs will be a better choice as their size is very small, typically in the range of 1 to 36 mm^2. Therefore, for a PET detector, a SiPM is an excellent alternative to PMTs as their small size can improve spatial resolution.

Chapter 3

LAr Single Cell Optimisation

To evaluate a LAr-PET detector's feasibility, a GEANT4 (GEometry ANd Tracking) simulation of a single LAr photon detector cell is created alongside the LAr cell prototype built in the laboratory, see Chapter 4. GEANT4 is a state of the art simulation toolkit of the passage of particles through matter. It is used in high energy, nuclear and accelerator physics, and studies in medical and space science [57]. The simulation allows the testing of potential improvements of the PET photon detector prototype and to evaluate various cell geometries and optical properties. As described in Chapter 1, a PET scanner consists of an array of cells arranged in a cylindrical format around the patient. Therefore, the optimisation of a single LAr cell is the first step towards constructing a complete PET detector.

3.1 Simulation Construction

There are many important metrics during the construction of a PET scanner, and one of the most important is detector efficiency. As described in Section 1.6.2, a PET scanner sensitivity is proportional to the square of the detector's efficiency. As a result, the simulation aims to improve the detector efficiency. Before describing in detail what detector efficiency is, an understating of the GEANT4 simulation construction is important.

GEANT4 splits the classes to mandatory and optional, for the construction of a simulation. For a simulation to work, GEANT4 requires at least three classes. Two of them are initialisation classes (Detector construction and Physics list), and the third one is an action class (Sensitive detectors). Any other class added in the GEANT4 simulation is considered as optional such as the detector visualisation. For the simulation of the single LAr cell, eight classes are created. Details regarding all the simulation classes can be found in the Git repository [58]. However, to better understand how the LAr cell optimisation is performed, three of the eight GEANT4 classes are going to be explained. These classes are the detector construction, the physics list, and the sensitive detector.

- **Detector construction**

  In this class, the detector geometry is defined as well as the properties of the materials. For example, if the cell is made from stainless steel, the optical properties (e.g. reflection, absorption) of stainless steel are implemented in this class. As LAr is the medium in which the annihilation photons will interact and then be detected, except for the LAr optical properties, its scintillation properties are also added in the detector construction class. For creating the various shapes of the cells under test, a python library developed at RHUL called pyg4ometry is used [59]. It allows easy creation of a GEANT4 geometry in its native GDML (Geometry Description Markup Language) format.

- **Physics list**

  In this class, the physics processes involved in PET scanner are implemented. The particles of interest are gammas, electrons and positrons. Therefore, at 511 keV energy and lower, the interactions of interest are the photoelectric effect, the Compton effect, bremsstrahlung, ionisation and multiple scattering. As LAr emits scintillation photons of ≈9.7 eV energy, their optical interactions are also implemented in this class.

- **Sensitive detectors**

  For the detection of the scintillation photons emitted by LAr, SiPMs are used. To emulate the detection properties of SiPMs sensitive detectors are used in GEANT4 with the same dimensions and properties (e.g. PDE) as the SiPMs under test. Sensitive detectors store all the information related to the detected particles such as energy, position and time. In this Chapter the term the SiPM and sensitive detector volume will be used interchangeably.

3.1.1 Detection Efficiency

In all the simulations, a hundred thousand 511 keV photons are generated per run. The simulation of a single 511 keV photon as the primary particle is referred to, in GEANT4, as an event. The number of scintillation photons detected per event is defined as hits. As stated, the metric for evaluating the various geometries created is the detection efficiency. Detection efficiency, ϵ is defined as

$$\epsilon = \frac{N_{\text{detected}}}{N_{\text{events}}} \tag{3.1}$$

where N_{detected} is the number of events produced scintillation photons that were detected by the SiPMs and N_{events} the number of events generated per run. The uncertainty in the detection efficiency $\delta\epsilon$ is equal to

$$\delta\epsilon = \sqrt{\left(\frac{\partial\epsilon}{\partial N_{\text{detected}}}\delta N_{\text{detected}}\right)^2 + \left(\frac{\partial\epsilon}{\partial N_{\text{events}}}\delta N_{\text{events}}\right)^2} \tag{3.2}$$

where $\delta N_{\text{detected}}$ is equal to the $\sqrt{N_{\text{detected}}}$ and δN_{events} is equal the $\sqrt{N_{\text{events}}}$. In this chapter, the high number of simulations results in detection efficiency plots with smaller uncertainties compared to the plotted points.

As in all measured signals, there is an intrinsic uncertainty present in the SiPMs readings. SiPMs noise primarily comes from dark counts, after-pulses and crosstalk. Dark counts are signals from thermally generated electrons within the pixels and not an external source. After-pulses are derived from a small portion of avalanching carriers trapped in impurities within the pixels. Lastly, crosstalk is generated from the energy lost as heat to phonon vibrations resulting from the scattering collisions of carriers. Because the value of noise will be known when the PET detector is completed, all geometries detection efficiency was evaluated based on various thresholds. The threshold is defined as the minimum number of scintillation photons detected from the SiPMs per event, that will be considered in the detection efficiency calculations. For example, if the threshold is five it means that events which the SiPMs detected less than five scintillation photons are not going to be considered in the detection efficiency calculation.

The focus of this chapter is to optimise the detection efficiency of a single LAr-cell, as detection efficiency in PET imaging is crucial because it directly impacts the dose of radiation a patient must receive to produce an accurate and informative image. A high detection efficiency means that fewer radioactive tracers are required for the imaging procedure, reducing the amount of radiation exposure for the patient. This is especially important for those undergoing repeated scans or those with increased sensitivity to radiation, such as young children or pregnant women. By optimising the detection efficiency in PET imaging, healthcare providers can ensure that patients receive the lowest possible radiation dose while still obtaining high-quality diagnostic images. This not only improves the safety and comfort of the patient but also helps to reduce the risk of long-term side effects and complications associated with radiation exposure.

3.2 LAr Cells Geometry

3.2.1 Tee Cell

The tee cell geometry reflects the geometry we have in the laboratory. To compare the results that will be acquired from the laboratory setup with the results taken from the GEANT4 simulation, the exact physical properties and dimensions of the stainless tee cell, LAr and SiPM are implemented in

GEANT4. The dimensions of the stainless steel tee cell are shown in Figure 3.1. The dimensions of the SiPM is 6 × 6 mm and is placed at the centre of the tee cell side fitting, see Figure 3.1.

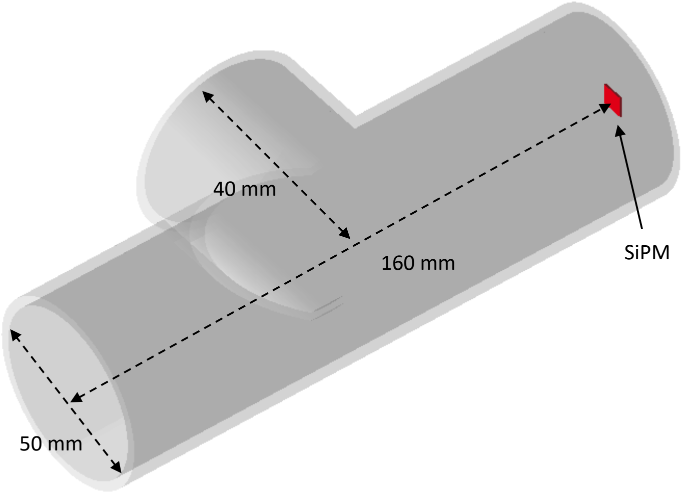

Figure 3.1: Dimensions of the stainless steel tee shape cell used in the laboratory.

As the energy of the scintillation photons generated from LAr is ≈9.7 eV, stainless steel's optical properties are important. It will determine the probability that the scintillation photons are reflected or absorbed at the tee cell walls. As a material, stainless-steel is not a good reflector of the VUV scintillation photons, see Figure 3.2, and as a result, a coating material with high reflectivity in VUV range is needed. However, at first, the goal is to compare the simulations results with the results which are going to be acquired from the experiments performed in the laboratory. As the tee cell in the laboratory is not initially coated, the GEANT4 simulation is made with no reflective coating. The addition of a reflective coating and its impact on the detection efficiency will be described in Section 3.3.

As already stated the reflectivity of a material can be implemented in GEANT4 using boarder surfaces. For example, in Figure 3.3 the stainless steel border surface is set at 100% and therefore the scintillation photon will bounce inside the tee cell until is absorbed by the SiPM or it undergoes a change in its physical process such as Rayleigh scattering within LAr (LAr is transparent to its own scintillation light). The Hamamatsu SiPM used in the laboratory has a photodetection efficiency (PDE) of approximately 14% at a photon wavelength of 128 nm (LAr scintillation light), see Figure 2.11. These values are then assigned to the sensitive detector (SiPM) in GEANT4 in the detector's construction class.

As previously stated, LAr light yield is 51 photons per keV, see Table 2.2, and therefore a single 511 keV has the potential to generate 26061 scintillation photons. Inside the detector's construction

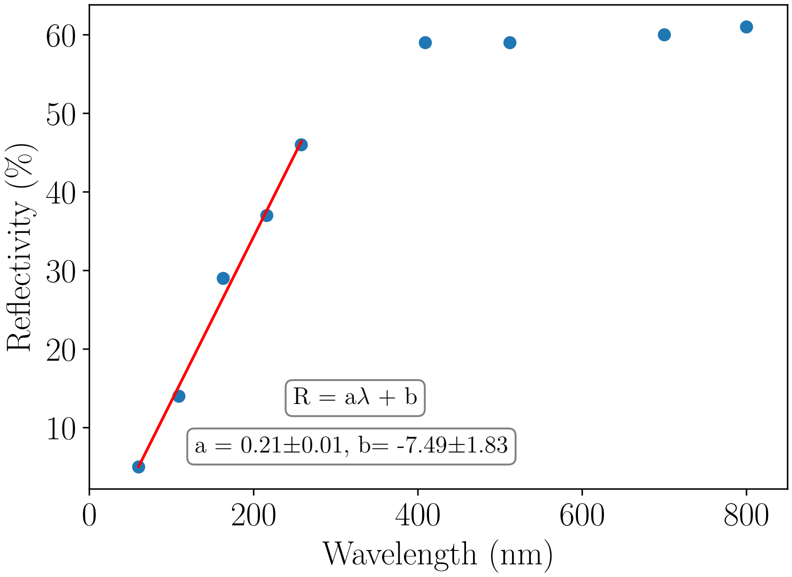

Figure 3.2: Stainless steel reflectivity as a function of wavelength [60], [61]. The red line shows the linear fit of reflectivity between 60 and 258 nm of photons wavelength.

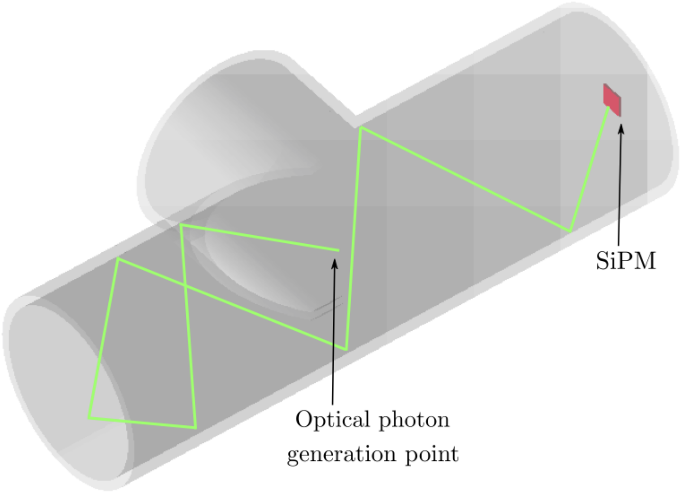

Figure 3.3: Visualisation from the GEANT4 simulation illustrating the boarder surfaces. A 9.7 eV optical photon is generated at the centre of the tee cell, and with stainless steel reflectivity set at 100% the optical photon is absorbed from the SiPM.

class, LAr's properties such as refractive index, absorption length, light yield and fast and slow decay time are implemented. Figure 3.4 shows an example of the scintillation photons generated within LAr from a 511 keV photon inside the tee cell (stainless steel reflectivity is set according to Figure 3.2).

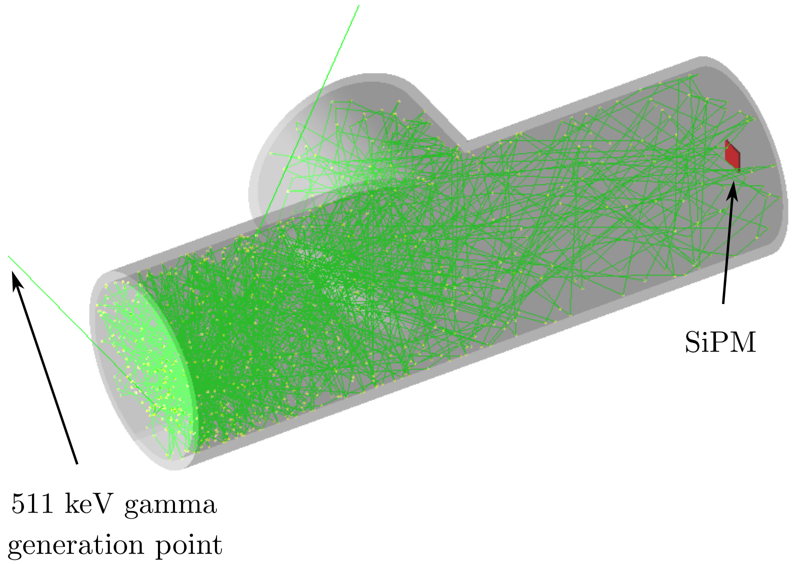

Figure 3.4: Visualisation from the GEANT4 simulation showing the scintillation photons generated from a 511 keV photon with the stainless steel tee cell.

To generate the annihilation photons in the laboratory, a collimated sodium 22 (^{22}Na) radioactive source is used. To reflect the detector's set-up in the laboratory, a collimated source is simulated in GEANT4 as well. The process which ^{22}Na decays is shown in Figure 3.5. When ^{22}Na decays to Neon (Ne) emits a gamma particle with an energy of 1274 keV. Before the emission of the gamma particle, it first decays to a lower state (^{22}Ne*) through the emission of a 546 keV positron 90% of the time or by capturing an orbital electron 10% of the time. To simulate the process in GEANT4 a random number between 1-10 is generated before each run. If that number is less and equal to 9 a positron is emitted otherwise if that number is equal to 10 no positron is emitted. Furthermore, in each run, a gamma particle with an energy of 1274 keV is emitted as the exited (^{22}Ne*) isotope emits a gamma particle to reach a stable state.

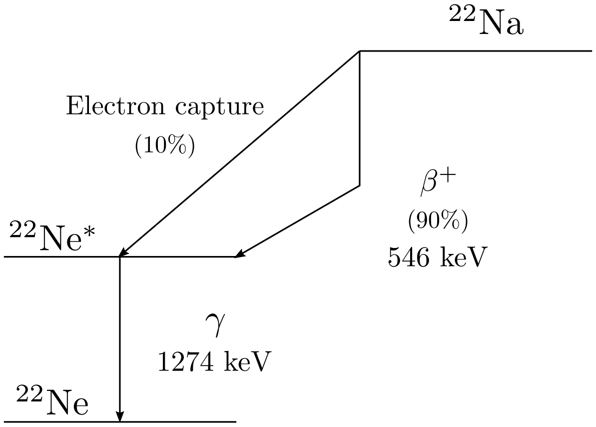

Figure 3.5: Sodium 22 decay scheme.

The positron emitted from the collimated radioactive source annihilates at the tee cell walls and two back-to-back 511 keV photons are generated. The thickness of the stainless steel wall is 1.65 mm and to ensure that all positrons are going to be annihilated, a GEANT4 simulation is created. A solid stainless-steel cube with sides equal to 1.65 mm is created and around it, a sensitive detector is placed, see Figure 3.6. A beta particle source is placed at the cube's centre, and then 100K events are generated. The energy of the positrons generated is 546 keV as the energy of the positrons emitted from the ^{22}Na source. The range R which the beta particles travelled before their annihilation is equal to

$$R = \sqrt{x^2 + y^2 + z^2} \tag{3.3}$$

where x, y and z are the beta particles coordinates from the cube centre before their annihilation. The average range over which the beta particles travel before they are annihilated in steel is ≈0.09 mm, see Figure 3.7. As a result, the beta particles emitted from the source are annihilated at the tee cell wall, and two back-to-back photons are emitted isotropically. The transmission probability of the 511 and 1250 keV photons through stainless-steel is shown in Figure 3.8. The annihilate 511 keV photons have a 9.45% interaction probability with the stainless steel wall and the 1250 keV photons emitted from the sodium source have an interaction probability of 6.71%.

Simulation Results

The GEANT4 simulation provides an insight on the results which are expected in the experiment built in the laboratory. Information such as the detection efficiency, the time profile of the scintillation photons detection and even the start location of the scintillation photons prior to their detection can

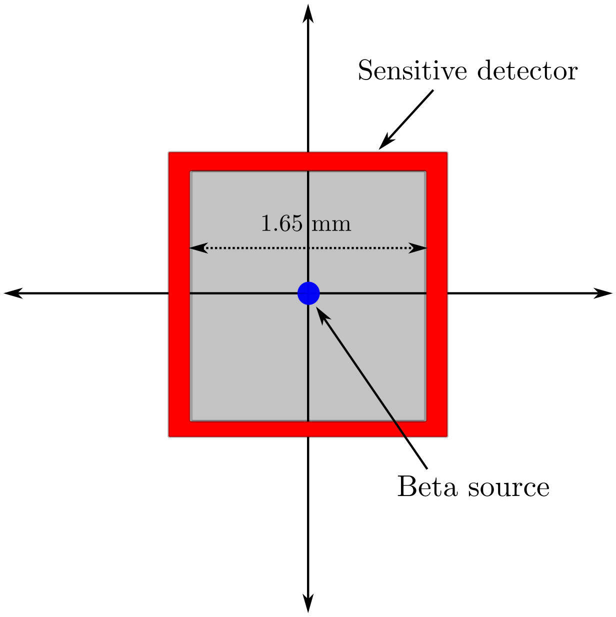

Figure 3.6: Schematic of the setup used in GEANT4 for calculating the positron range in stainless steel.

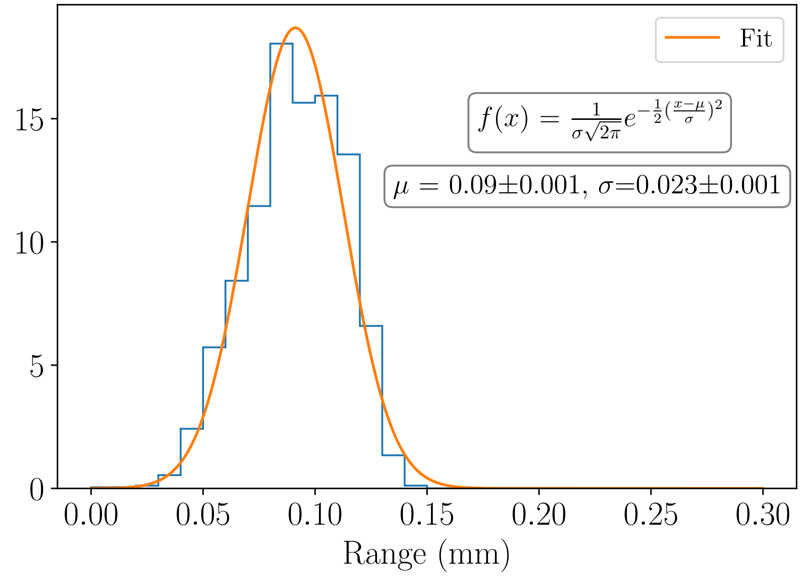

Figure 3.7: Histogram of the positron range emitted within a stainless steel.

be recorded. To calculate the detection efficiency, the ^{22}Na source is placed 5 mm outside the tee cell (y-axis) and 20 mm away from the SiPM (x-axis), see Figure 3.9. Then the source is moved along

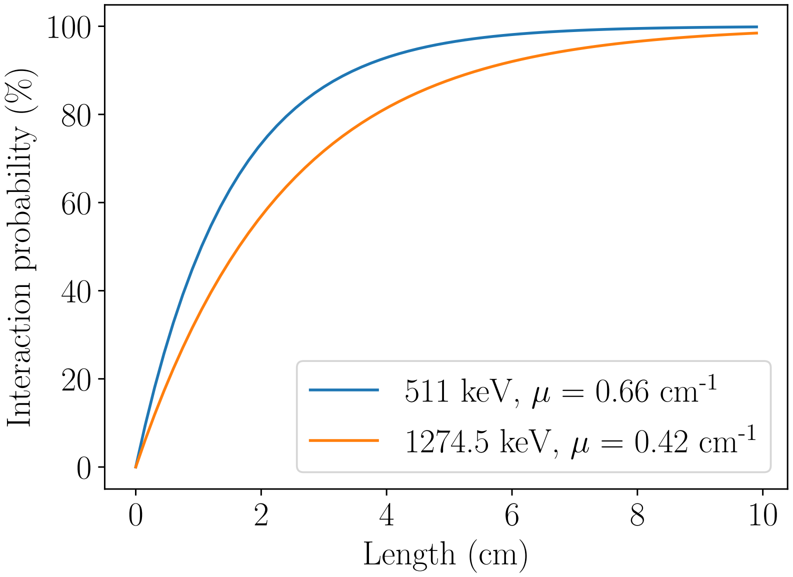

Figure 3.8: Interaction probability of a 511 and 1250 keV photon with stainless-steel.

a straight line along the x-axis, and the detection efficiency is measured. The position of the source along the z-axis stayed unchanged at 0 mm.

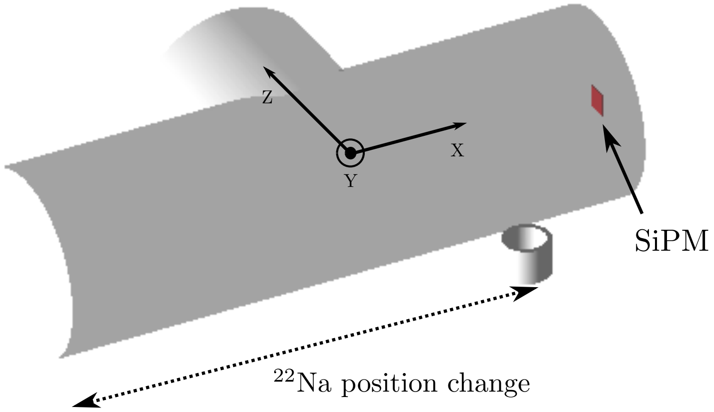

Figure 3.9: Schematic of the setup used for the detection efficiency calculation based on the position of the sodium 22 source along the x-axis. Source is placed 20 mm outside (y-axis) the tee cell.

Figure 3.10 shows the detection efficiency as a function of the scintillation photons threshold. As already stated the position of the source in relation to the SiPM is initially placed 20 mm away from the SiPM (x-axis) and then is moved with a step of 20 mm until the distance between the SiPM and the source is 140 mm. Due to the fact that the reflectivity of stainless steel at 128 nm photons wavelength (LAr scintillation photons) is approximately 20% the probability that the scintillation photons will undergo multiple reflections before reaching the SiPM is low and therefore, the closer the source is to the SiPM the higher the detection efficiency is.

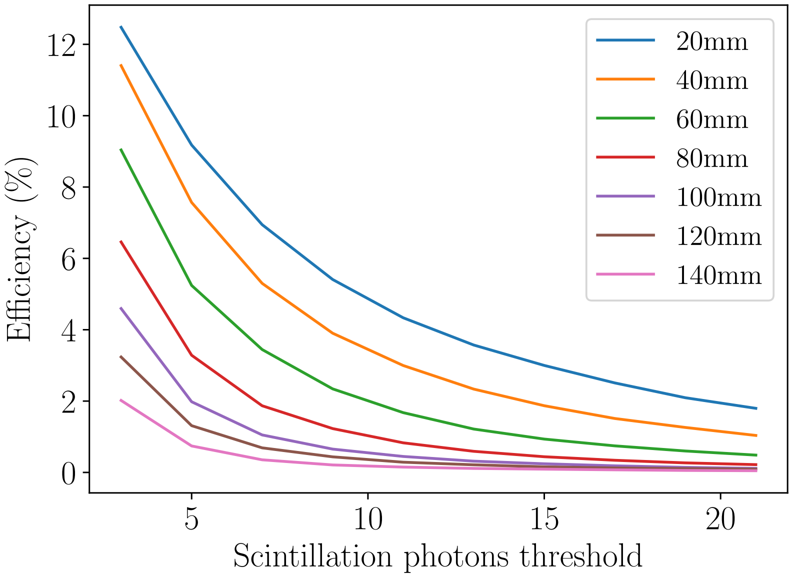

Figure 3.10: Detection efficiency calculation based on the position of the sodium 22 source along the x-axis, and the scintillation photons threshold.

The GEANT4 simulation gives the ability to store the scintillation photons starting position before their detection from the SiPM. Figure 3.11, 3.12 and 3.13 shows the x, y and z coordinates of the scintillation photons before their detection. As expected, when the radioactive source is closer to the SiPM (x-coordinate), more scintillation photons are detected. The coordinate of the SiPM in mm is (80,0,0), and the majority of the detected scintillation photons originate from the centre of the tee cell's cross-section (y = 0 mm, z= 0 mm) as at this position scintillation photons travel straight to the SiPM without the poor steel reflectivity affecting them.

Lastly, the time profile of the detected scintillation photons can give the acquisition time window for the experiment performed in the laboratory. This window can be calculated by subtracting the maximum time, t_{max} , from the minimum time, t_{min}, that the scintillation photons are detected per event and average it. Usually, the acquisition window depends on the number of the scintillation

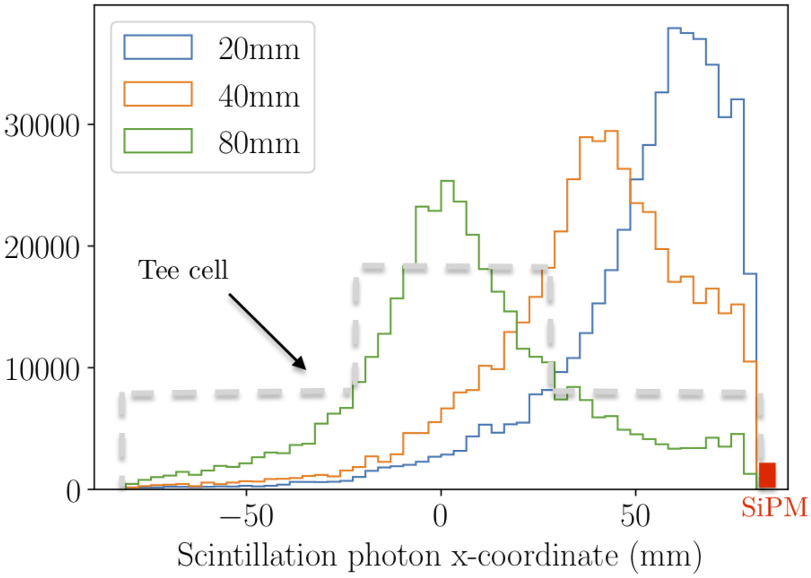

Figure 3.11: Scintillation photons starting location x-coordinate.

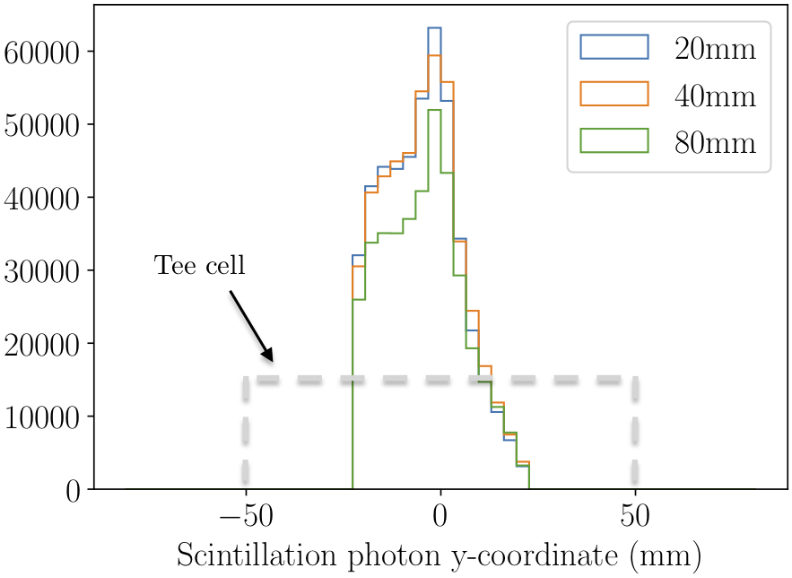

Figure 3.12: Scintillation photons starting location y-coordinate.

photons detected, but in the case that the preset number is not reached the data acquisition system enters an infinite waiting loop. By knowing the approximate time window, that infinite loop can be forced to stop. Figure 3.14 shows the maximum and minimum detection time of scintillation photons

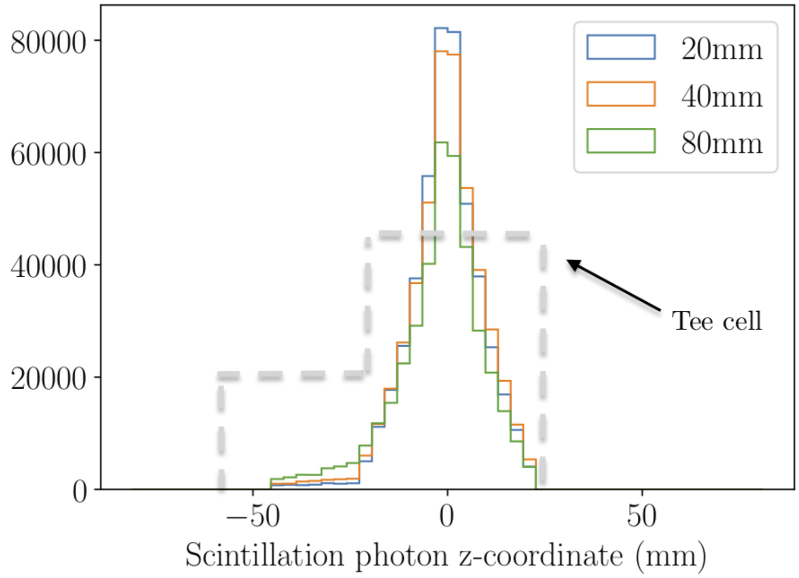

Figure 3.13: Scintillation photons starting location z-coordinate.

in each event, and by averaging the subtracted value of $t_{\max} - t_{\min}$, the acquisition window is found to be 2028.42 ns.

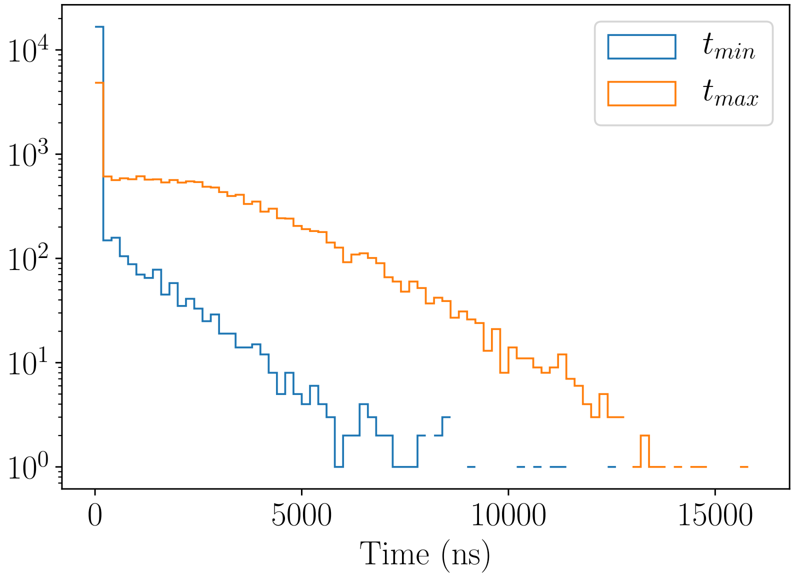

Figure 3.14: Histogram showing the minimum and maximum time scintillation photons are detected in each event.

3.3 Cell Optimisation

The GEANT4 simulation goal is to allow improvements and modifications to a LAr cell and maximise its detection efficiency. Alongside the laboratory's experiment construction, various factors that can improve the detection efficiency such as different geometries and coating materials are evaluated in GEANT4. As shown in Figure 3.2, stainless steel reflectivity at VUV wavelengths is poor, and therefore, a coating material with high reflectivity at VUV wavelengths can increase detection efficiency. Such material is Aluminium with magnesium fluoride (Al+MgF$_2$). For over four decades, Al+MgF$_2$ has set the standard at a high-efficiency reflective coating at VUV wavelengths. Action Optics and Coating is a USA-based company that works with Al+MgF$_2$. By contacting them, they have provided us with the reflectivity as a function of the wavelength of their commercial Al+MgF$_2$ [62]. The detection efficiency can be evaluated by inserting these data to the GEANT4 simulations and as a result, creating a coating surface inside the cell. Figure 3.15 shows Al+MgF$_2$ reflectivity as a function of photons wavelength.

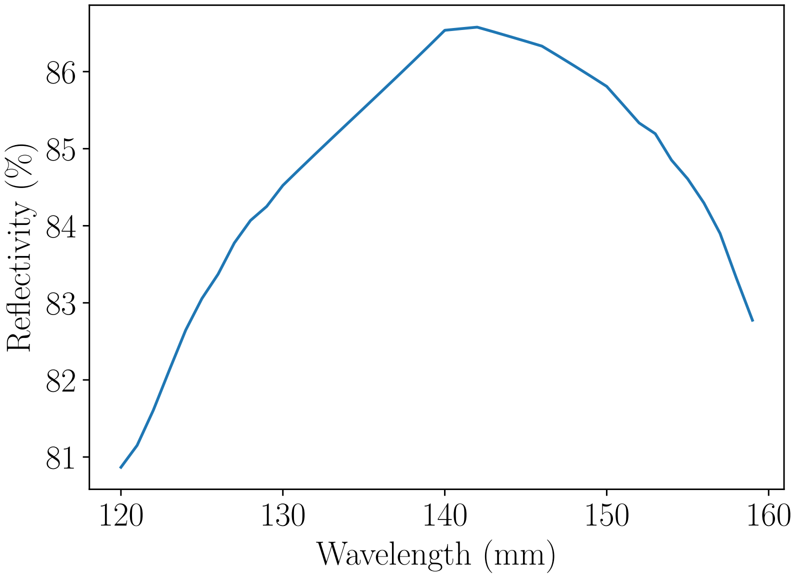

Figure 3.15: Al+MgF$_2$ reflectivity as a function of photons wavelength [62].

During the simulation of the best possible cell's geometry, two factors are also evaluated. First, each cell geometry under test has its length increase as this will also increase the probability of the 511 keV photons interacting with LAr. Therefore more scintillation photons will be emitted, see Equation 1.13 and 1.16. As Liquid argon density is not comparable with that of the common scintillation crystals, a longer length LAr cell is needed to stop the 511 keV annihilation photon. Figure 3.16

shows the interaction probability of a 511 keV as a function of the LAr cell's length. This Figure is made using LAr's linear attenuation coefficient at 511 keV, which is 0.1109 cm^{-1}, and then by inserting it to Equation 1.16, the interaction probability of the 511 keV photon as a function of cell length is plotted. Second, depending on the cell geometry, the maximum number of SiPMs attached on a cell side is simulated. A greater photosensitive area is expected to increase the number of scintillation photons detected.

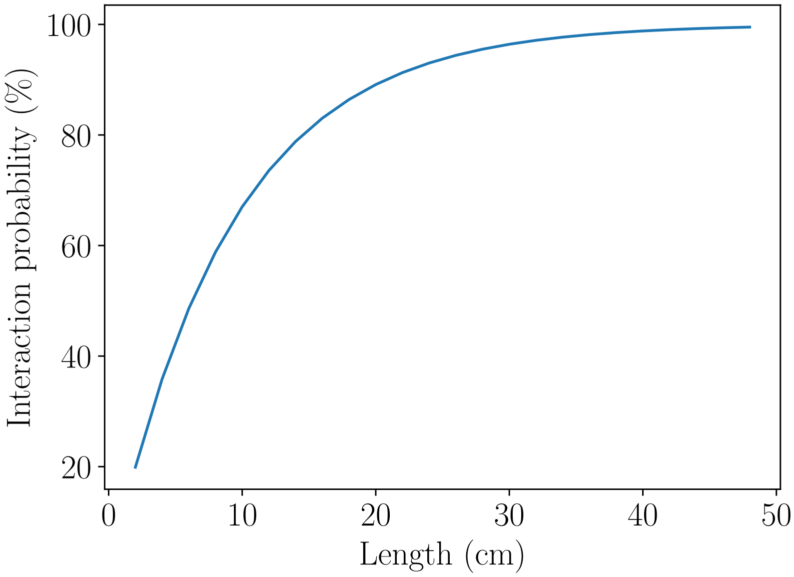

Figure 3.16: Interaction probability of a 511 keV as a function of LAr cell's length.

Cylindrical Geometry

The first geometry under test is the cylindrical stainless steel cell, see Figure 3.17. The source is placed outside of the cylindrical cell at coordinates (-150, 0, 0) mm. The x-coordinate of the source does not play an important role as the cylinder cell is placed in a vacuum. The cell's radius is kept the same as in the tee cell configuration, and only the length of the cylinder is changed. As shown in Equation 1.13, the cylindrical cell's cross-section does not increase the interaction probability of the annihilation photon with the LAr. Therefore the radius of the cylindrical cell stayed the same as the one in the tee cell. As a result, it will enable an easy fit of the optimised new cell to the experiment built in the laboratory in a later stage. As the 511 keV photon is emitted towards the LAr filled cylindrical cell, it first interacts with stainless steel. The stainless steel fitting length is 4 mm (conflat (CF) ultra-high vacuum fitting), and at 511 keV, its linear attenuation is 0.677 cm^{-1}. Using Equation

1.15, the transmission probability of the 511 keV photon through the stainless-steel is 76.27%, see Figure 3.8. Therefore, the closer the simulated detection efficiency is to the transmission probability of a 511 keV photon through a 4mm length stainless-steel the better.

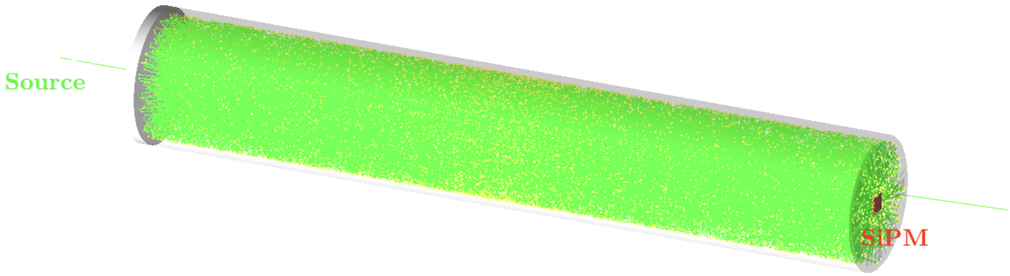

Figure 3.17: Visualisation of the LAr filled stainless steel cylindrical cell acquired from the GEANT4 simulation.

As in the tee cell simulation, the SiPM is placed on the right side of the cylinder at the centre of the side cap, and as already stated the source is placed on the left side of the cylinder, see Figure 3.18. All the cylinders are coated with Al+MgF$_2$ and 100K 511 keV photons are emitted directly (x-direction) to the cylindrical cells. For this stage to emit the 511 keV photons isotropically does not provide any information regarding the best cell geometry. Figure 3.17 shows the detection efficiency of various length cylinders as a function of the scintillation photons threshold. At a threshold of 14 scintillation photons and less the detection efficiency is increased alongside the cylinder's length. However, for a threshold of 14 scintillation photons and more, cylinders with length greater than 16 cm have their detection efficiency reduced. This can be explained because although by increasing the LAr cells length will result in more 511 keV photons interacting with LAr, the scintillation photons generated isotropically will be reflected more times within a longer length cylinder compared to a shorter length cylinder before reaching the SiPM. As Al+MgF$_2$ does not have a 100% reflectivity at LAr's scintillation photons wavelength and the SiPM photosensitive area is small, increasing the length of the cylinders more than 16 cm does not result in an increase in the detection efficiency.

With the addition of the Al+MgF$_2$ the scintillation photons start location before their detection by the SiPM is also recorded. This information essentially gives the location where the Compton scattering occurred in the vessel and then led to the generation of the LAr's scintillation photons. Figure 3.20, 3.19 and 3.21 show the x, y and z coordinates of the scintillation photons for cylinders with lengths of 12, 20 and 28 cm.

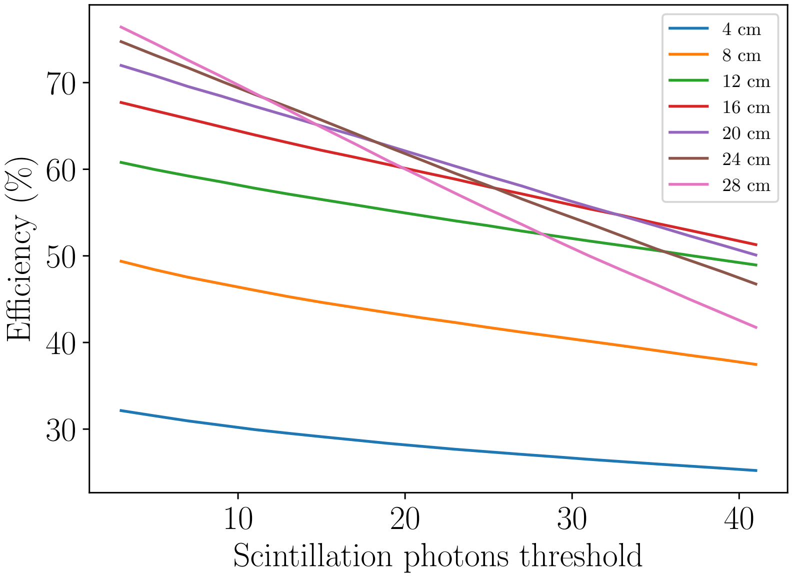

Figure 3.18: Detection efficiency of a various length cylinders as a function of scintillation photons threshold.

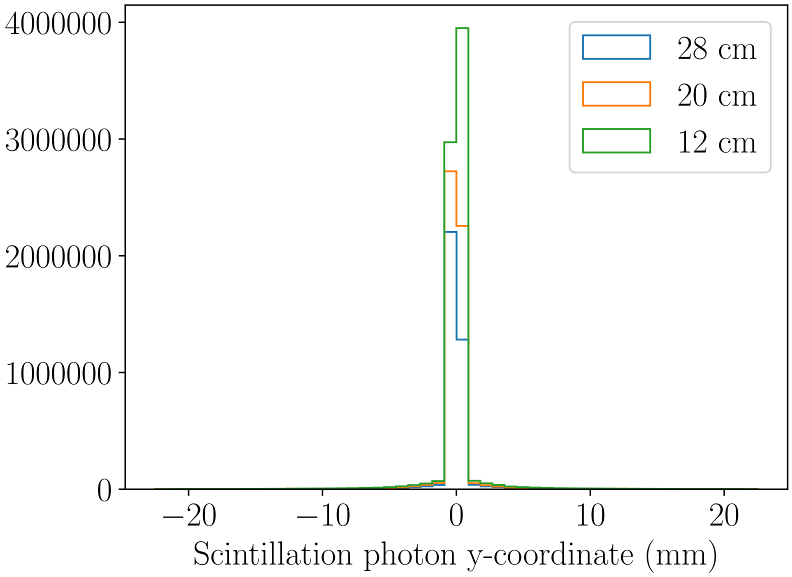

Figure 3.19: Scintillation photons starting location y-coordinate on coated cylindrical cells with lengths of 12, 20 and 28 cm.

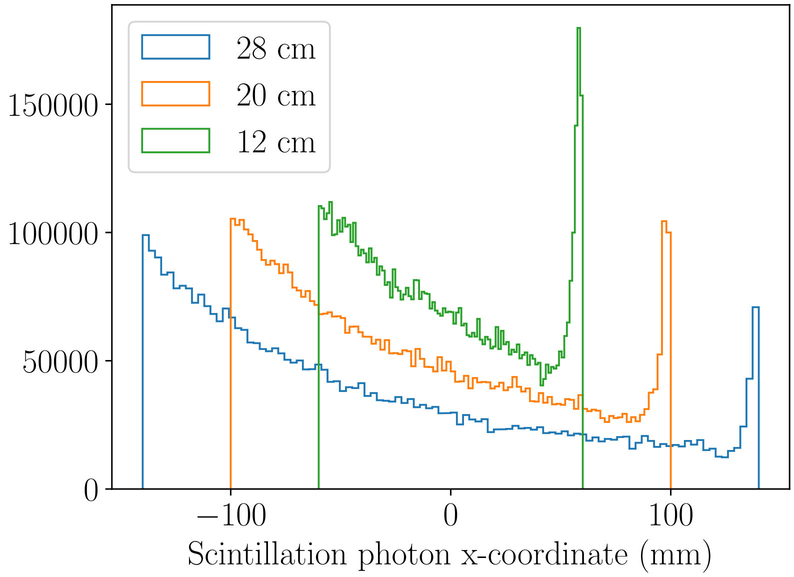

Figure 3.20: Scintillation photons starting location x-coordinate on coated cylindrical cells with lengths of 12, 20 and 28 cm.

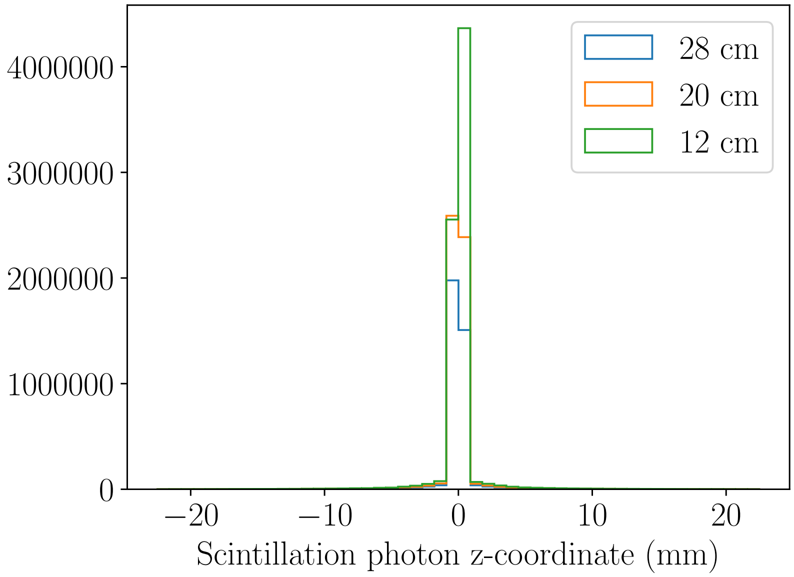

Figure 3.21: Scintillation photons starting location z-coordinate on coated cylindrical cells with lengths of 12, 20 and 28 cm.

Coordinate y and z represent the cross-section of the cylinders. From Figure 3.19 and 3.21, the majority of the detected scintillation photons originated from y and z equal to 0 mm. As the source and the SiPM y and z coordinate equals to zero, this comes as no surprise. When the 511 keV photon enters the cylindrical cell, it undergoes Compton scattering, and from the isotropically emitted scintillation photons, the ones that travelled straight to the SiPM without bouncing within the cell first have a higher chance to be detected. The starting x-coordinate of the scintillation photons see Figure 3.20, shows that the scintillation photons are detected across all the cylinders lengths with a higher number of scintillation photons detected at the entry point of the 511 keV photon into the cell, and also close to the SiPM. This is expected, as when the 511 keV photon enters the liquid argon volume will interact with it via Compton scattering generate the scintillation photons, and probably escape the vessel. On the other hand, the high number of scintillation photons which originate closer to the SiPM have a higher probability of being detected by the SiPM as they are closer to the photosensitive area, and therefore, will not undergo multiple reflections before their detection. This can be proven using Figure 3.22, which shows the x-coordinate of the scintillation photon split into two categories in a cylinder with 12 cm length. In the first category, only events that generated more than 200 scintillation photons had their x-coordinate histogrammed. In contrast, events that generated less than 200 scintillation photons had their x-coordinate histogrammed separately. From Figure 3.22, it can be seen that events that had a high number of scintillation events detected are originated close to the SiPM, whereas events that have a lower number of scintillation photons detected are originated close to the entry point of the 511 keV photons to the cylindrical cell.

Using the same configurations like the one in Figure 3.17 the same length cylinders are evaluated but in this time an array of 30 SiPM is placed on the right side of the cylinders instead of just one, see Figure 3.23. As already stated the diameter of the side flanges of the cylindrical vessels is 50 mm, and that is due to the CF50 flanges used in the experiment contacted in the laboratory. Figure 3.24 shows the detection efficiency of various length cylinders as a function of the scintillation photons threshold in the configurations of 30 SiPMs.

The highest detection efficiency is observed for a cylinder with a length of 28 cm. The increase in the number of the SiPMs resulted in a smaller decrease in the detection efficiency as a function of the scintillation photons threshold compared to the one SiPM setup, see Figure 3.25. In both tests, the detection efficiency dropped linearly with the increase of the scintillation photons threshold, but with different gradients. In the 30 SiPM configuration, the detection efficiency drops with a slope of -0.14, whereas in the one SiPM setup dropped with a slope of -0.92.

The scintillation photons starting location is also recorded as in the one SiPM configuration. The y and z coordinate (cylinder cross-section) does not show any variation compared to the one SiPM

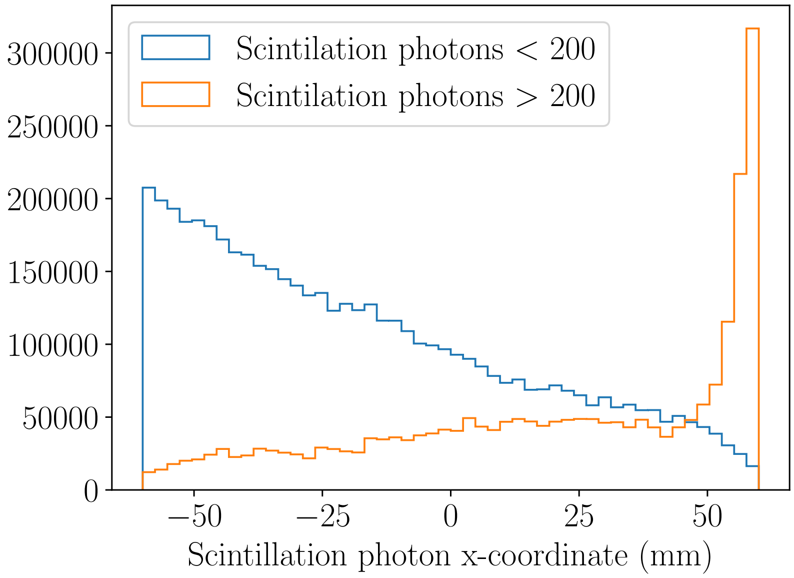

Figure 3.22: Histogram of the starting x-coordinate of the scintillation photons prior to their detection in a cylinder with a length of 12 cm. The orange histogram shows the x-coordinate of the scintillation photons on events which generated more than 200 detected scintillation photons. The blue histogram shows the x-coordinate of the scintillation photons on events which generated less than 200 detected scintillation photons.

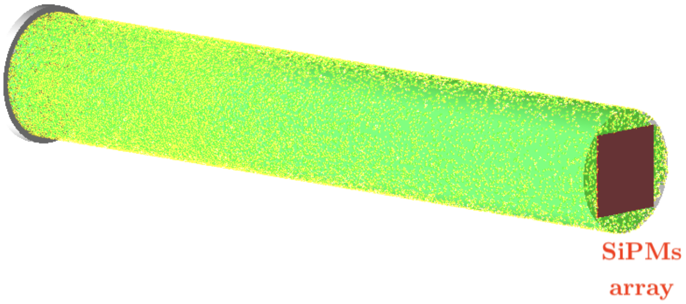

Figure 3.23: Visualisation of the LAr filled stainless steel cylindrical cell acquired from the GEANT4 simulation showing the 30 SiPMs array.

setup. However, with the increase of the photosensitive area, the effect which an event closer to the SiPM had a much higher probability of being detected (Figure 3.21), is not observed, see Figure 3.26 (cylinder of 28 cm length). Definitely scintillation photons generated closer to the SiPM will have

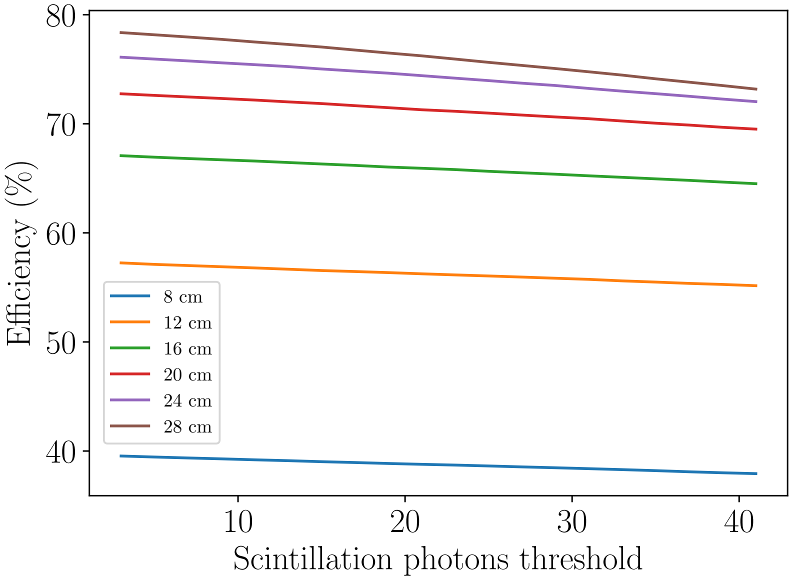

Figure 3.24: Detection efficiency of a various length cylinders as a function of scintillation photons threshold on a 30 SiPMs configuration.

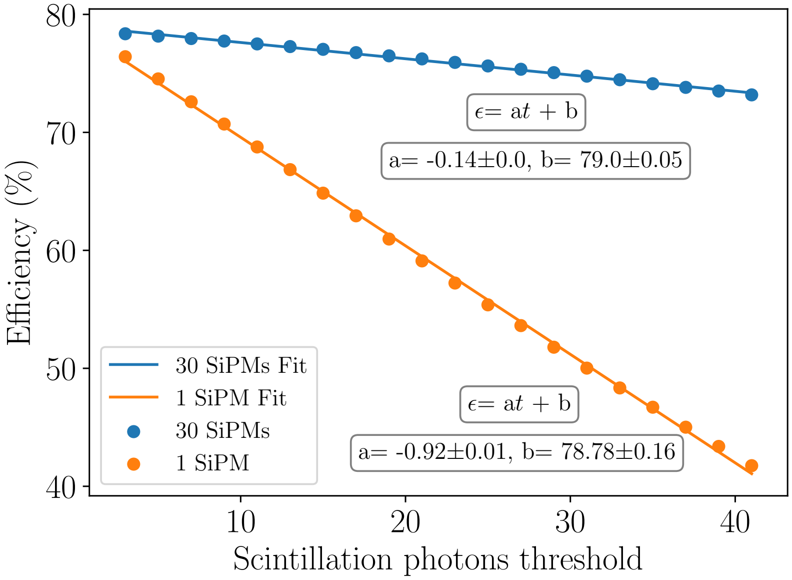

Figure 3.25: Comparison of the detection Efficiency as a function of the scintillation photons threshold in a 28 cm length cylinder using one and 30 SiPMs configurations.

a higher probability to be detected. However, the coating of the vessel along with the increase in number of SiPMs reduces this geometrical factor.

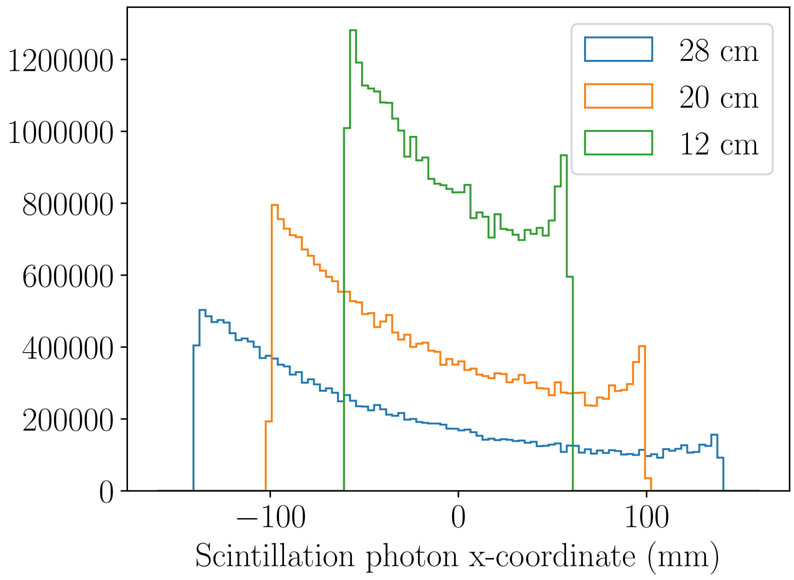

Figure 3.26: Scintillation photons starting location x-coordinate on coated cylindrical cells with a 30 SiPM configuration. Cylinder with a length of 12, 20 and 28 cm are histogrammed.

Box and Trapezoid Geometry

The second geometry under evaluation is the box shape, see Figure 3.27. As in the cylindrical cell geometry, 30 SiPMs are used, and that number of SiPMs is kept constant in all the geometries simulated. The box cell dimensions are 35 × 35 × l cm, where l is the variable length of the box. The LAr volume in each simulation is $30 \times 30 \times l$. The same coating material (Al+MgF$_2$) as in the cylindrical shape cell is used. The source is placed outside of the box cell at coordinates (-150, 0, 0) mm. As already stated, the box's length is varied with 4 cm increments during the detection efficiency evaluation simulations. The generated 100K 511 keV photons have their direction fixed towards the box cell, as in the cylindrical cell simulations.

Figure 3.28 shows the detection efficiency of various length boxes as a function of the scintillation photons threshold. As the length of the box shape cells increases, the detection efficiency increases as well. This is expected, as already shown in Figure 3.16, the probability of the 511 keV photons interacting with LAr volume increases with the length of the cell. The scintillation photons' starting location is also recorded as in the cylindrical cell simulations, but no notable behaviour is observed. The shape of the histograms of the x, y and z starting location coordinates of the scintillation photons

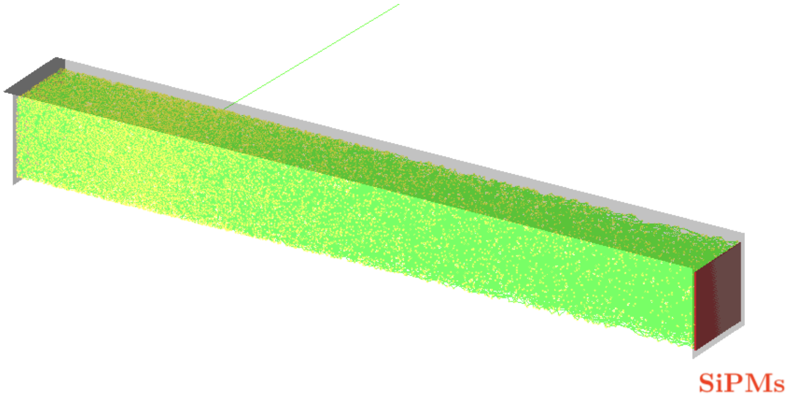

Figure 3.27: Visualisation of the LAr filled stainless-steel box shape cell acquired from the GEANT4 simulation.

is the same as in the cylindrical cell, see Figure 3.20, 3.19 and 3.21.

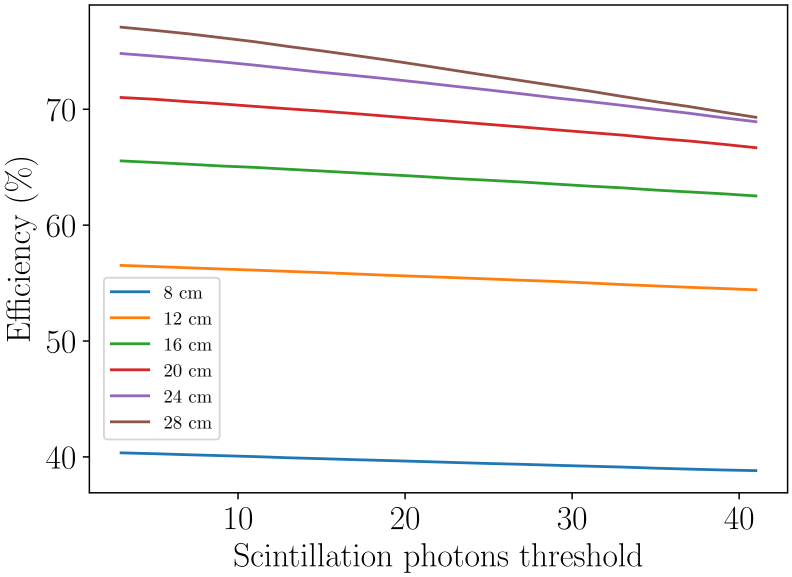

Figure 3.28: Detection efficiency of a various length boxes as a function of scintillation photons threshold.

The last geometry tested is a trapezoid cell, see Figure 3.29. The reasoning behind this shape is that the scintillation photons generated isotropically in the LAr will be guided towards the SiPMs and hopefully increase the detection efficiency. The number of SiPMs is kept the same (30) as in the other geometries. The dimensions of the side which the 30 SiPMs are attached is 17.5 × 17.5 cm and the second side is double that (35 × 35 cm). The length of the trapezoid is varied and increased with an increment of 4 cm. The source is placed outside of the trapezoid cell at the same location as in the cylindrical and box shape vessels.

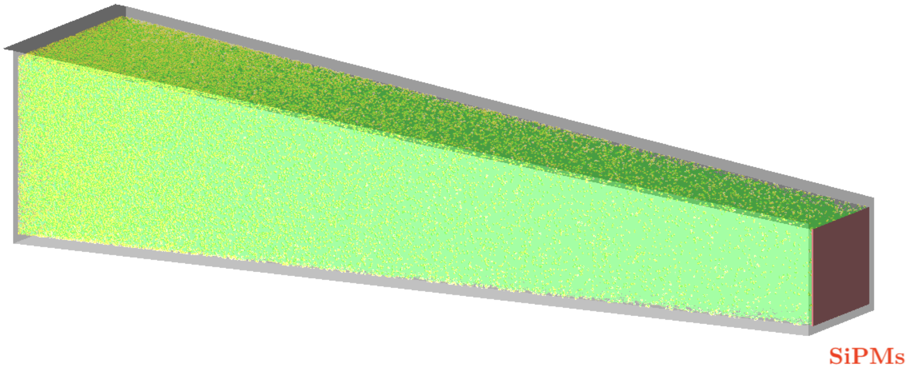

Figure 3.29: Visualisation of the LAr filled stainless-steel trapezoid cell acquired from the GEANT4 simulation. Note that the image of the trapezoid is rotated in the GEANT4 simulation to visualise the geometry better.

Figure 3.30 shows the detection efficiency of various length trapezoids as a function of the scintillation photons threshold. As in the other geometries, the detection efficiency increases with the increase of the cell's length. The increase of the scintillation photons threshold results in a linear drop of the detection efficiency, which is a similar behaviour observed on all geometries simulated. The scintillation photons starting location is also recorded as in the other geometries simulations, but no notable behaviour is observed. The shape of the histograms of the x, y and z starting location coordinates of the scintillation photons is the same as in the cylindrical cell, see Figure 3.20, 3.19 and 3.21.

To evaluate which geometry from the tested ones is the most suitable for a PET detector cell regarding to their detection efficiency, the gradient which the detection efficiency drops as a function of the scintillation photons is used. Figure 3.31 shows the detection efficiency as a function of the scintillation photons threshold in a 28 cm length box, trapezoid and cylindrical shape cells. The cylindrical shape cell has the smallest drop in the detection efficiency as a function of the threshold, compared to the other shapes. That is important because the number of the scintillation photons threshold represents the discarded scintillation photons detected by the SiPMs due to noise, see Section 2.10.

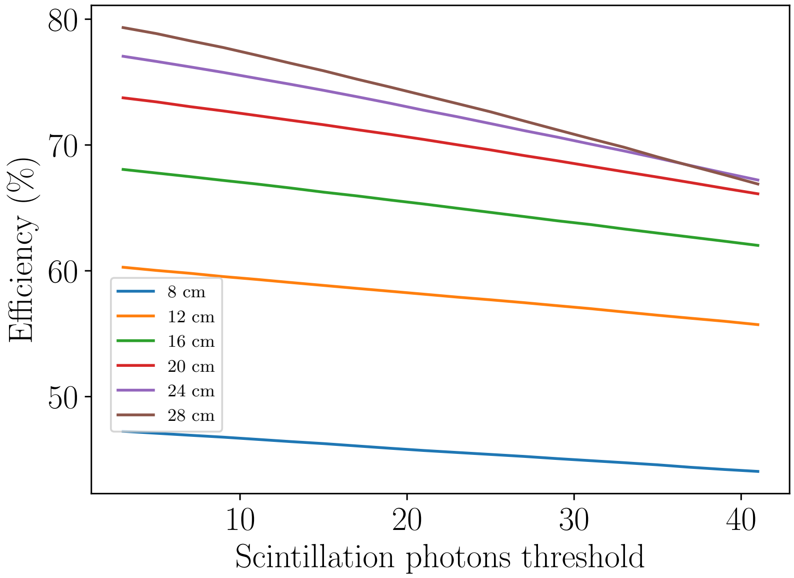

Figure 3.30: Detection efficiency of a various length trapezoids as a function of scintillation photons threshold.

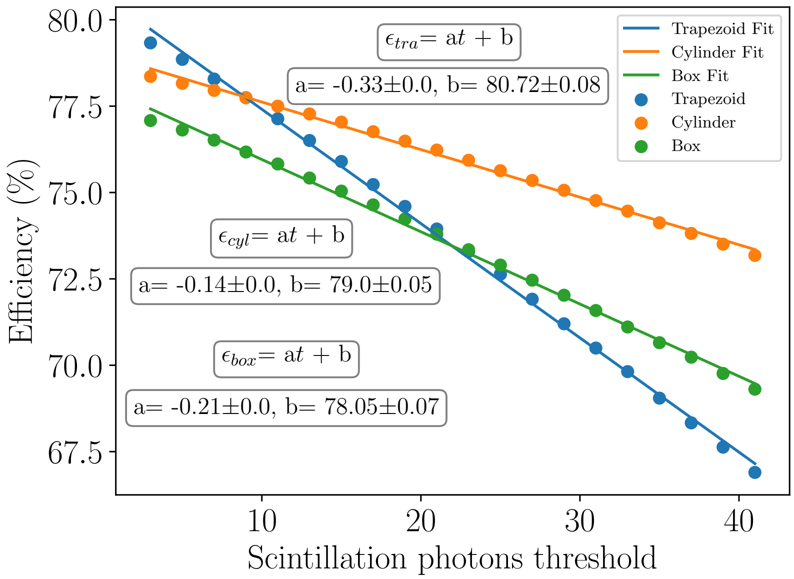

Figure 3.31: Detection efficiency as a function of scintillation photons threshold in a 28 cm length box, trapezoid and cylindrical shape cells. Fit lines are linear functions.

3.4 Energy Resolution

An essential property of scintillation detectors is the energy resolution. The energy resolution is the ability of a scintillation detector to precisely determine the incoming radiation's energy. Gaussian distributions usually describe the energy deposition of these detectors, and by using the standard deviation of the Gaussian distribution (σ) the energy resolution ΔE of a detector is equal to

$$\Delta E = \mathrm{FWHM} = 2\sqrt{2\ln 2}\ \sigma. \tag{3.4}$$

The relative energy resolution E_r is defined as the $FWHM$ divided by the value of peak centroid

$$E_r = \frac{\Delta E}{E} \tag{3.5}$$

where ΔE is equal to the $FWHM$ of the photopeak, and E the energy of the incoming radiation.

To evaluate the LAr cell's energy resolution, a 28 cm long cylinder is used with the 30 SiPMs configuration, which is the same setup used in the detection efficiency evaluation. To calculate the energy resolution of the cylindrical cell, the LAr volume is turned into a sensitive detector in the simulation, and the energy deposited to it is recorded. Figure 3.32 shows the energy deposited to the LAr volume from the two hundred thousand 511 keV photons emitted towards the LAr cell. In Figure 3.32, the Compton photopeak represents the events in which a full absorption of the incoming gamma ray occurred, and the Compton edge shows the events in which the 511 keV photons Compton scattered inside LAr, and therefore only a portion of the initial gamma-ray energy is deposited to the scintillation medium. From Figure 3.32, it can be seen that the energy of the incoming radiation is the 511 keV, as expected.

However, in a PET cell the energy resolution of a detector is calculated based on the data acquired from the SiPMs as this is the only data one can have. The scintillation photons emitted from LAr are proportional to the energy deposited in it. Each keV deposited to LAr can approximately emit 51 scintillation photons. From those photons some will be absorbed by the stainless steel wall as Al+$\mathrm{MgF_2}$ reflectivity is not 100%, some will be absorbed the SiPMs and not be counted as their detection efficiency is not 100%, and lastly some will be absorbed by LAr as the attenuation length of the scintillation photons in LAr is 66 ±3 cm [67]. Although, LAr is highly transparent to its own scintillation light the increase in LAr cell's length to increase the detection efficiency will inevitably result in a high number of scintillation photons be absorbed by LAr. The reabsorbed photons are not able to excite an electron from the valance band to the conduction band (Band gap: $E_g = 14.3$ ev).

By making the LAr volume which is the mother volume of the two SiPMs placed at the side of the LAr cylinder a sensitive detector, the number of the scintillation photons that deposit energy to LAr and the SiPMs can be measured. Figure 3.33 shows the histogram of the scintillation photons

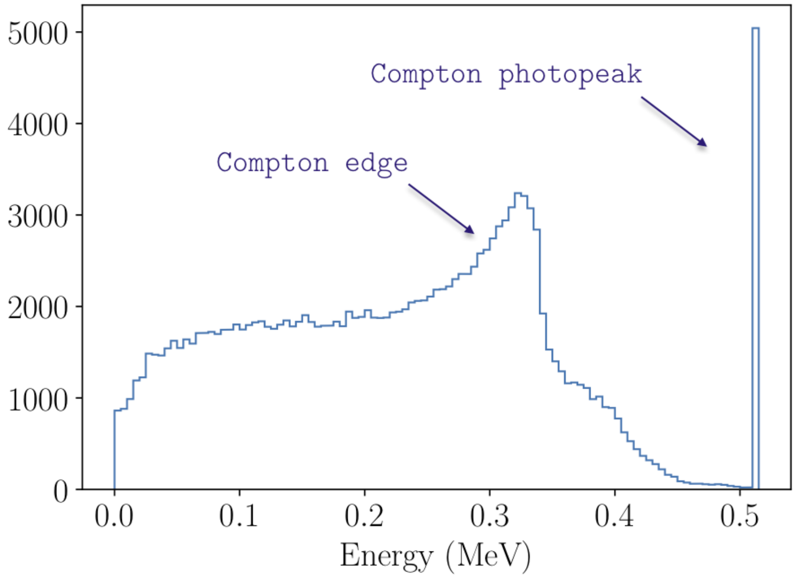

Figure 3.32: Histogram of the energy deposition of the two hundred thousand 511 keV photons emitted to the LAr cylindrical cell.

reabsorbed by LAr, and Figure 3.34 shows the histogram of the scintillation photons that deposited energy to the SiPMs. From the scintillation photons detected by the LAr volume (sensitive detector), 9.18% is detected by the SiPMs and 90.82% (100% - scintillation photons detected by the SiPMs) are reabsorbed back to LAr, see Figure 3.35. From Figure 3.34 it can be shown that the Compton absorption peak can not be distinguished from the Compton edge.

To confirm that the setup with the two SiPMs placed on the sides of the 28 cm cylinder and the Al+MgF$_2$ coating has a poor energy resolution, one more test is performed. A comparison of the detected scintillation photons by the SiPMs depending on the deposited energy of the 511 keV photons emitted toward the LAr volume is made, see Figure 3.36. Three categories are used to split the detected scintillation photons by the SiPMs, (a) detected scintillation photons originating from events that deposited all their energy to LAr (full absorption), (b) detected scintillation photons originating from events that deposited energy less than 511 keV, and (c) the sum of the two above categories which in fact is the SiPMs readout.

To evaluate if by increasing the reflectivity of the stainless-steel cylinder from ≈84% (Al+MgF$_2$) to 100% will improve the energy resolution, a simulation is performed using the same setup as in in the Al+MgF$_2$ test but the reflectivity is set to 100%. Once more, a high number of scintillation photons is expected to be absorbed by LAr, but as no scintillation photons will be absorbed by the stainless-steel

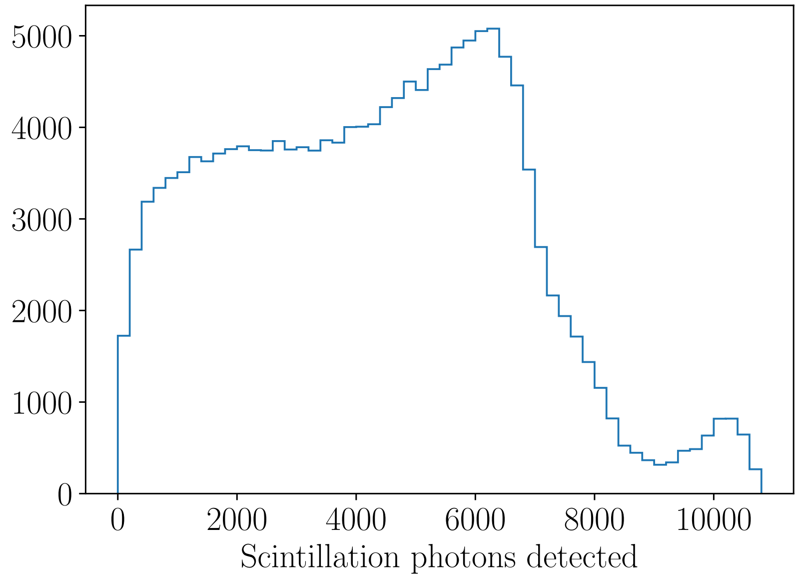

Figure 3.33: Histogram of the scintillation photons reabsorbed by LAr.

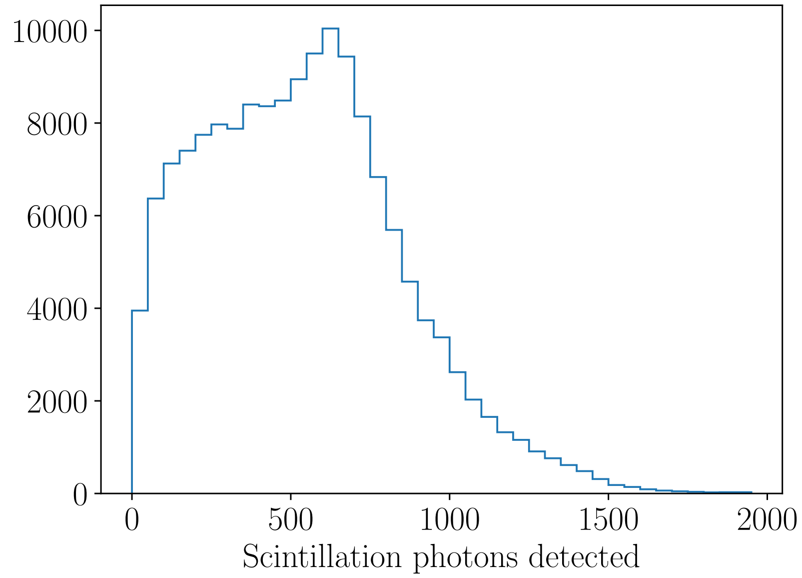

Figure 3.34: Histogram of the scintillation photons detected by the SiPMs.

walls it may be enough to distinguish the Compton edge from the Compton photopeak. A comparison of the detected scintillation photons by the SiPMs depending on the deposited energy of the 511 keV photons emitted toward the LAr volume is made, see Figure 3.37. The same three categories as

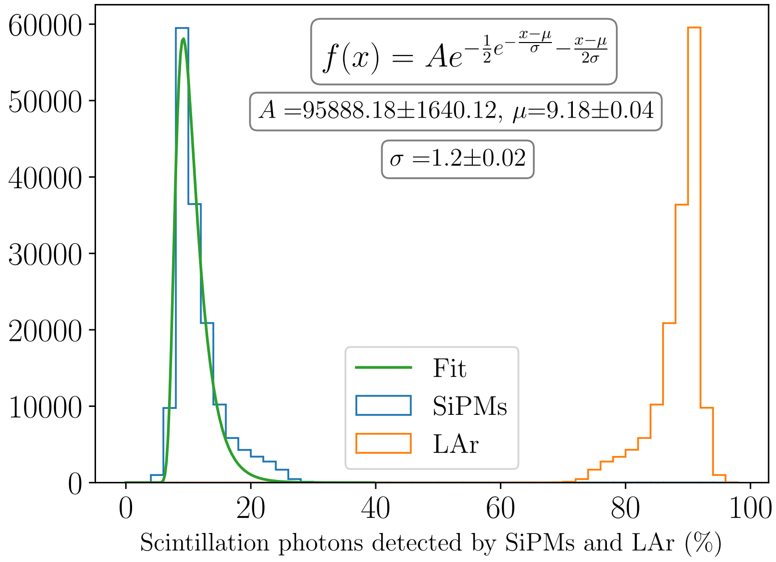

Figure 3.35: Histogram of the percentage of the scintillation photons detected by SiPMs and the scintillation photons reabsorbed by LAr.

before is used to split the detected scintillation photons, (a) detected scintillation photons originating from events that deposited all their energy to LAr (full absorption), (b) detected scintillation photons originating from events that deposited energy less than 511 keV, and (c) the sum of the two above categories which in fact is the SiPMs readout. From Figure 3.37 the 511 keV Compton photopeak can be distinguish from the Compton edge, and therefore the energy resolution can be calculated.

Figure 3.38 shows the fit of the histogram of the Compton photopeak measured by the SiPMs. Using Equation 3.5 and the fitted parameters in Figure 3.38 the relative energy resolution calculated is 1.14%. Although, commercial PET detectors have energy resolution well below 10% they use an energy resolution window of 30% (460keV - 560keV) [68] to allow a greater number of photons to be detected, and reduce the scan time of the patient. Therefore using this cell configuration, a single ring PET detector can be built, see Chapter 5. Although, Al+MgF$_2$ greatly increases the detection efficiency of the detector compared to no coating at all, does not have a good energy resolution. As the stopping power of LAr is low and therefore a long LAr volume is needed to increase the interaction probability of the 511 keV photons with LAr. The long length cylinder results also in a high number of scintillation photons to be reabsorbed by LAr and without a coating material with a reflectivity 100% a good energy resolution can not be achieved.

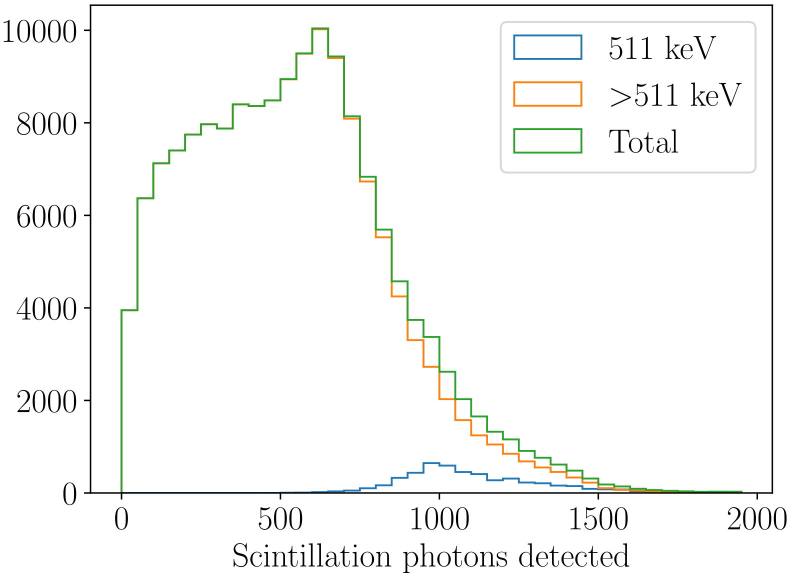

Figure 3.36: Histogram of the detected scintillation photons by SiPMs depending on the deposited energy of the 511 keV photons emitted toward the LAr volume. The blue histogram shows the detected scintillation photons originating from events that deposited all their energy to LAr. The orange histogram shows the detected scintillation photons originating from events that deposited energy less than 511 keV. The green histogram shows the SiPMs readout which is the sum of the histogram blue and orange. The Compton photopeak can not be distinguish from the Compton edge.

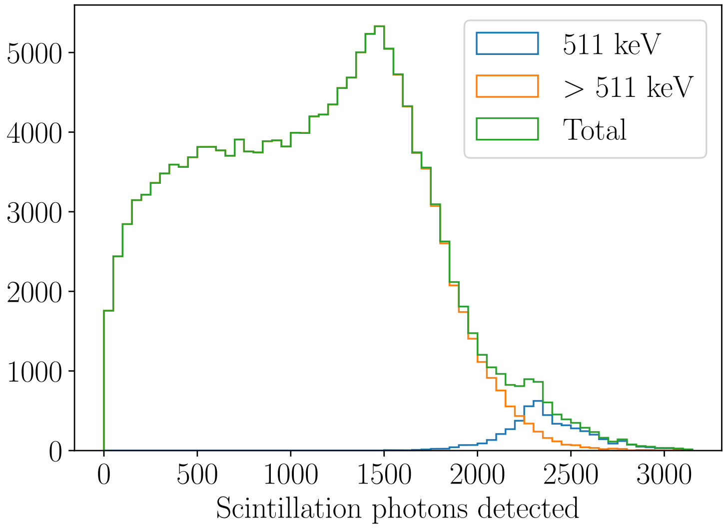

Figure 3.37: Histogram of the detected scintillation photons by SiPMs depending on the deposited energy of the 511 keV photons emitted toward the LAr volume. The blue histogram shows the detected scintillation photons originating from events that deposited all their energy to LAr. The orange histogram shows the detected scintillation photons originating from events that deposited energy less than 511 keV. The green histogram shows the SiPMs readout which is the sum of the histogram blue and orange. The Compton photopeak can be distinguish from the Compton edge.

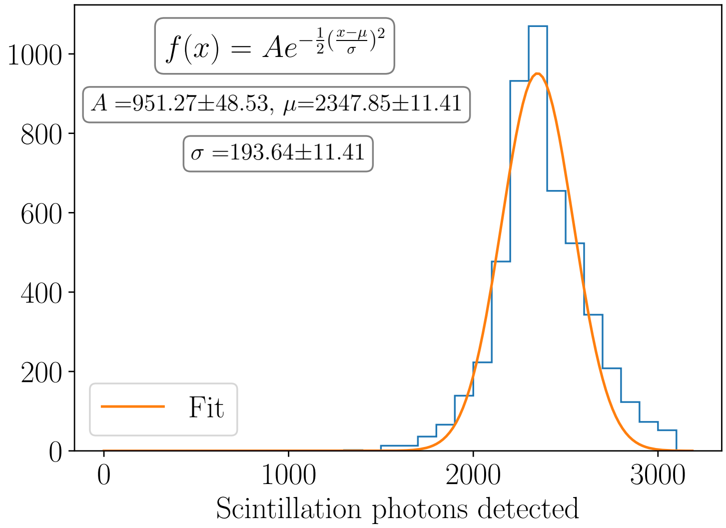

Figure 3.38: Histogram of the scintillation photon detected buy the SiPMs when a full absorption of the 511 keV photons occurs within the LAr volume.

3.5 Depth of Interaction and Time of Flight

As shown in Figure 3.16 to increase the probability that the 511 keV photons will interact with LAr, a long cell is needed. The dominant electromagnetic interaction which produces the scintillation photons is the Compton scattering following by the photoelectric effect. In Section 1.7.3 the concept of time of flight (TOF) is described, and using that principle, the depth in which the 511 keV photon interacted within the cell can be found. To calculate the depth of interaction, SiPMs must be placed on both sides of the vessel, see Figure 3.39.

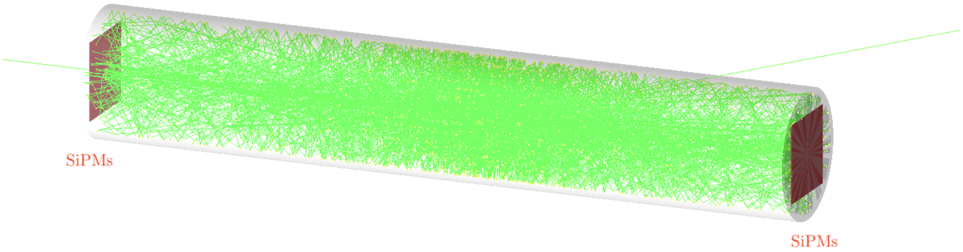

Figure 3.39: Visualisation from the GEANT4 simulation showing the two 30 SiPM arrays placed on the side of the cylindrical cell for the calculation of depth of interaction.

In a cylindrical cell that can be used in a PET scanner, the data which are recorded from the SiPMs is the energy of the scintillation photons and the time at which the scintillation photons are detected. Using the time information recorded from the SiPMs, the location at which the scintillation photons originate inside the cell can be estimated. For example, when a 511 keV photon is emitted towards the cylindrical cell, it will interact with LAr in a certain depth inside the cell, and then the scintillation photons will be emitted. As the scintillation photons that are detected first travelled the shortest distance, the starting x-coordinate of the scintillation photons can be estimated and then compared with the true starting x-coordinate of the scintillation photons acquired through the GEANT4 simulation. Before showing the equation used to calculate the starting location of the scintillation photons, the concept of TOF is shown in Figure 3.40.

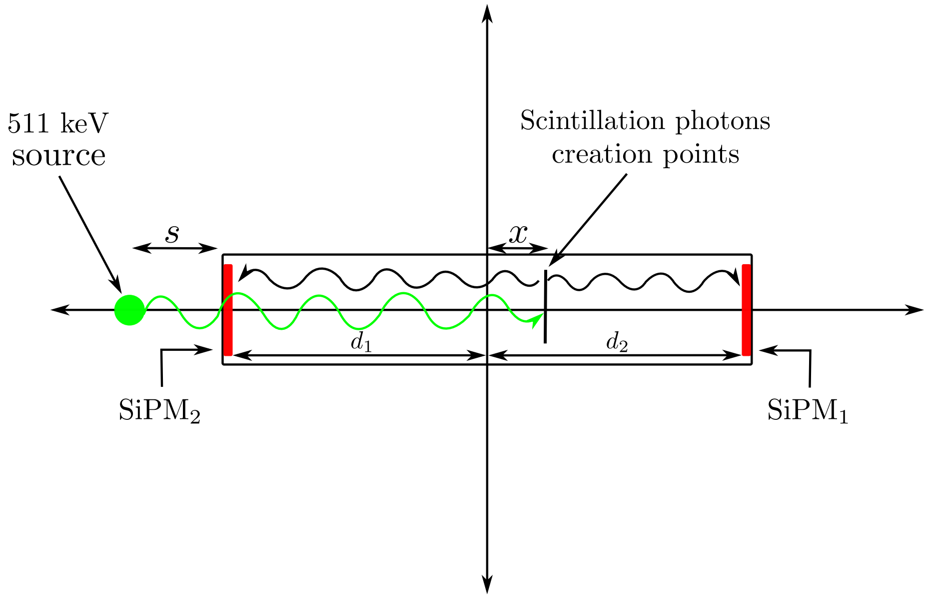

Figure 3.40: Schematic of the Time of Flight (TOF) model used to estimate the starting x-coordinate of the scintillation photons within a PET cell.

In the GEANT4 simulation, the clock starts from the moment that the 511 keV photon is generated. Therefore, the time t_1 and t_2 represents the time at which the scintillation photons are detected from the SiPM$_1$ and SiPM$_2$ respectively, and are equal to

$$t_1 = \frac{s + d_1 + x}{c} + \frac{d_2 - x}{u_1} \tag{3.6}$$

$$t_2 = \frac{s + d_1 + x}{c} + \frac{x + d_1}{u_2} \tag{3.7}$$

$$u_1 = u_2 = \frac{c}{n} \tag{3.8}$$

$$d_1 = d_2 \tag{3.9}$$

where s is the distance of the source from SiPM$_1$, d_1 the distance of the SiPM$_1$ from the centre of the cylinder, d_2 the distance of the SiPM$_2$ from the centre of the cylinder, c the speed of light and n the refractive index of the LAr's scintillation photons wavelength. Using Eq. 3.8 and Eq. 3.9 and by subtracting Eq. 3.6 from Eq. 3.7 the starting x-coordinate of the scintillation photons is equal to

$$x = \frac{c(t_2 - t_1)}{2n}. \tag{3.10}$$

As already stated, the true x-coordinate of the scintillation photons is recorded in the GEANT4 simulation, and therefore it can be compared with the estimated x-coordinate from the TOF model shown in Eq. 3.10. Before comparing the two models, the data have undergone two cuts. First, the events in which both SiPMs have detected scintillation photons are kept, and second, events in which the estimated x-coordinate is outside of the cylinder boundaries are discarded (≈20% of the events). Figure 3.41 shows a comparison between the true x-coordinated of the scintillation photons reached fastest the SiPMs recorded from GEANT4 simulation and TOF model. The red line shows the linear fit of the true x-coordinate.

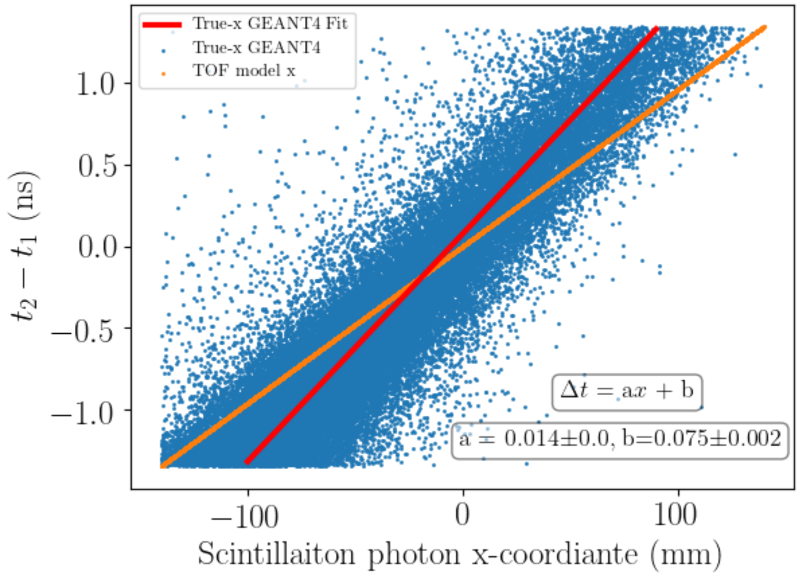

Figure 3.41: Comparison between the true x-coordinate of the scintillation photons recorded from the GEANT4 simulation and the TOF model. The red line shows the linear fit of the true x-coordinate.

As expected, the TOF-model is not a perfect match with the GEANT4 simulation. From the isotropically generated photons, the two scintillation photons that reached the fastest the SiPMs have not always travelled a straight path as in the Figure 3.40. For Example, a scintillation photon starting location is close to the SiPM_1, and the fastest detected photon bounced first on the cylinder's wall and then it was detected. That will result in misplacing the starting x-coordinate of the scintillation photons using the TOF-model as the photon seems that travelled a longer distance. Using the Root Mean Square Error (RMSE), the TOF-model prediction error can be estimated, and therefore, give the predicted x-coordinate resolution.

$$\text{RMSE} = \sqrt{\sum_{i=1}^{n} \frac{(\hat{x}_i - x_i)^2}{n}} = 24.18 \text{ mm} \tag{3.11}$$

where the $\hat{x}$ is the TOF model x-coordinate prediction, x the true x-coordinate acquired from the fitted data of the GEANT4 simulation, and n the number of events. Therefore, in a 28 cm long cylinder, the true-x coordinate of the scintillation photons can be estimated with a resolution of ±3.3 cm.

Chapter 4

PET Photon Detector Prototype

An experiment was developed to validate the results shown in Chapter 3, where the LAr scintillation detector was simulated in GEANT4. This Chapter describes the development of the LAr cell prototype defined as LArCell throughout this Chapter. As the boiling point of argon lies in the cryogenic temperature range, a careful design of the cryogenic system is essential. In these temperatures, the slightest design flaw will not allow the LArCell prototype to drop to the desired cryogenic temperature, which is 87.15 K (argon boiling temperature). For the development of the LArCell prototype, except the cryogenic system design, a series of various systems had to be developed, such as the vacuum, monitoring and data acquisition systems. First, the two vacuum systems were designed, to bring the volume surrounding the LAr cell prototype and the LAr cell itself under vacuum. Second, a slow control system was designed to monitor the state of the prototype during the experiment and continuously stores the data from all instruments connected to the LArCell, such as the temperature and pressure of the system. Lastly, to store the data from the digitiser, which is connected to the submerged SiPM in LAr, a Digital to Analogue Converter (DAC) code was written.

4.1 Vacuum Systems

As already stated, two vacuum systems are designed. The two vacuum systems are isolated from each other, and therefore, their design is different. The first vacuum system role is to evacuate the volume surrounding the LAr cell prototype, and throughout this thesis, this system is defined as the external vacuum system. The air molecules surrounding the LAr cell act as a heat sink and therefore must be removed from the system. Section 4.1.1 outlines the correct operation of the external vacuum system. Next, a vacuum system responsible for the vacuum of the LAr cell itself is designed separately. This system is defined as the internal vacuum system throughout this Chapter. The LAr cell and the gas lines which the argon gas will flow prior to its liquefication must be free from any leaks, see Section 4.1.3, and contaminations. To establish a system with as few contaminants as possible, one must first evacuate the air inside the LAr cell and second remove any oxygen and nitrogen gas molecules trapped in the walls using more advanced techniques described in Section 4.3.4, such as cold and warm flashing.

4.1.1 Vacuum System Surrounding the LAr Cell

Figure 4.1 shows the design of the vacuum system surrounding the LAr cell. The material used for the construction of the external vacuum system is stainless steel 304L and the reason for that choice is the very low rate of outgassing of stainless steel in a vacuum, and also its ability to withstand high vacuum pressures without any deformations. The LAr cell is placed inside the external vacuum system, and therefore, the volume around the LAr cell must be in a vacuum. The external vacuum system consists of a scroll pump, turbomolecular pump, two mechanical valves, one vent valve, one overpressure relief valve, the cryocooler, and the electronics feedthroughs.

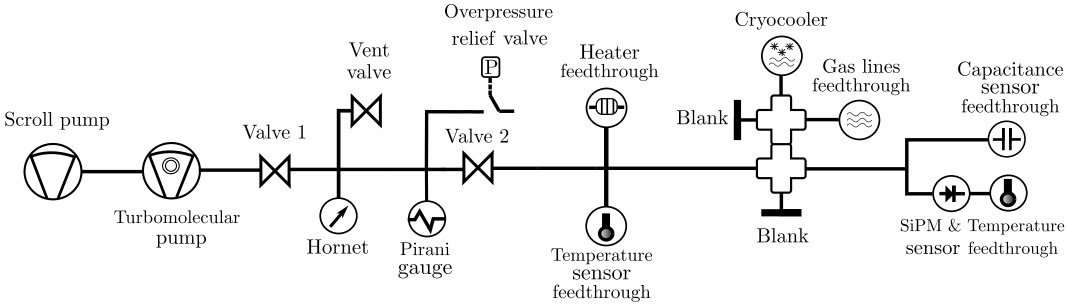

Figure 4.1: Diagram of the vacuum system responsible for vacuum the volume around the LArCell and the gas lines.

The procedure to start the vacuum of the external vacuum system, see Figure 4.1, is:

1. Close the vent valve to isolate the vacuum system from the atmosphere.
2. Open valves 1 and 2.
3. Turn ON the Hornet pressure monitor instrument.
4. Turn ON the scroll pump and wait until the pressure of the system is at 23 mbar, which is the operating pressure of the turbomolecular pump.

5. Turn ON the turbomolecular pump until the pressure of the system reaches a pressure of 5×10^{-4} mbar.

Assuming the vacuum system has reached the desired pressure, it strongly indicates that no major leaks are present in the system, such as not adequately sealed joints. However, the quality of the vacuum system is tested using multiple leak tests, see Section 4.1.3. As already stated, the LAr cell photon detector prototype is inside the vacuum system described above. Since 430 litres of argon gas are needed to fill the LAr vessel (expansion ratio 1:800), a safety pressure relief valve is attached to the vacuum system. In the event of system failure, the overpressure relief valve will open automatically at 1.2 bars, and the build-up pressure in the system will be vented safely.

Apart from the recommended start-up procedure of the external vacuum system defined above, its correct shut-down is also essential. To ensure the safety of the personnel operating the LArCell prototype and the safety of the equipment, the following steps must be performed:

1. Close valve 1 to isolate the turbomolecular and scroll pump from the rest of the external vacuum system.
2. Turn off the turbomolecular pump and wait until its rotating speed is zero.
3. Turn off the scroll pump.
4. Open the vent valve slowly and allow the external vacuum system to reach atmospheric pressure.

4.1.2 Vacuum System of LAr Cell

Figure 4.2 shows the design of the vacuum system design responsible for the vacuum of the LAr cell and the gas lines. This vacuum system is defined as the internal vacuum system and consists of a scroll pump, a turbomolecular pump, seven mechanical valves, one vent valve, one pressure regulator valve, one flow control valve, four overpressure relief valves, one pressure monitor system used during the vacuum process, one overpressure monitor system used during the argon liquefication process, see Section 4.3.4, a getter (gas purifier), a residual gas analyser (RGA), two temperature sensors and the SiPM. The materials of the flanges used to construct the internal vacuum system are stainless steel (304L and 316L) and cooper. The solid orange lines show where copper is used in the system, whereas the solid black lines show where stainless steel is used. The dotted black line indicates the pre-existing manifold. This manifold was pre-install in the laboratory, and its purpose is to supply the LArCell prototype with argon gas through valve 6. The argon gas pressure, fed into the LArCell is adjusted from the pressure regulator valve located inside the manifold. Standard pressure regulator valves are designed to roughly set the input gas pressure into the system, but they can not ensure repeatable gas flow adjustments and accuracy. Therefore, a vernier handle flow control valve is installed in the system.

The pre-existing manifold has two overpressure relief valves. The overpressure relief valve 4 opens at 10 bar and releases the argon gas outside of the laboratory in the event of a failure. Furthermore, a second overpressure relief valve is installed in the manifold, which opens if the overpressure relief valve 4 fails to open. This valve is the overpressure relief valve 3, and its difference from the overpressure relief valve 4 is that the argon gas will be released in the laboratory and not outside. As argon is heavier than oxygen, an oxygen depletion assessment is performed, see Section 4.3.4. In the event that all the argon gas stored in the manifold is released into the room, the safety of the personnel operating the LArCell prototype is ensured.

In addition to the two overpressure relief valves 3 and 4, two more overpressure relief valves are installed in the internal vacuum system. These valves are the overpressure relief valves 1 and 2, opening automatically at 1.04 bars. As the liquefication of argon will be done at a pressure of 1 bar, these overpressure relief valves are chosen for two reasons. First, it will ensure that the pressure in the gas lines and the LAr cell will not exceed the desired 1 bar pressure, and also, in the event of a failure, will act as a safety mechanism, see Figure 4.2.

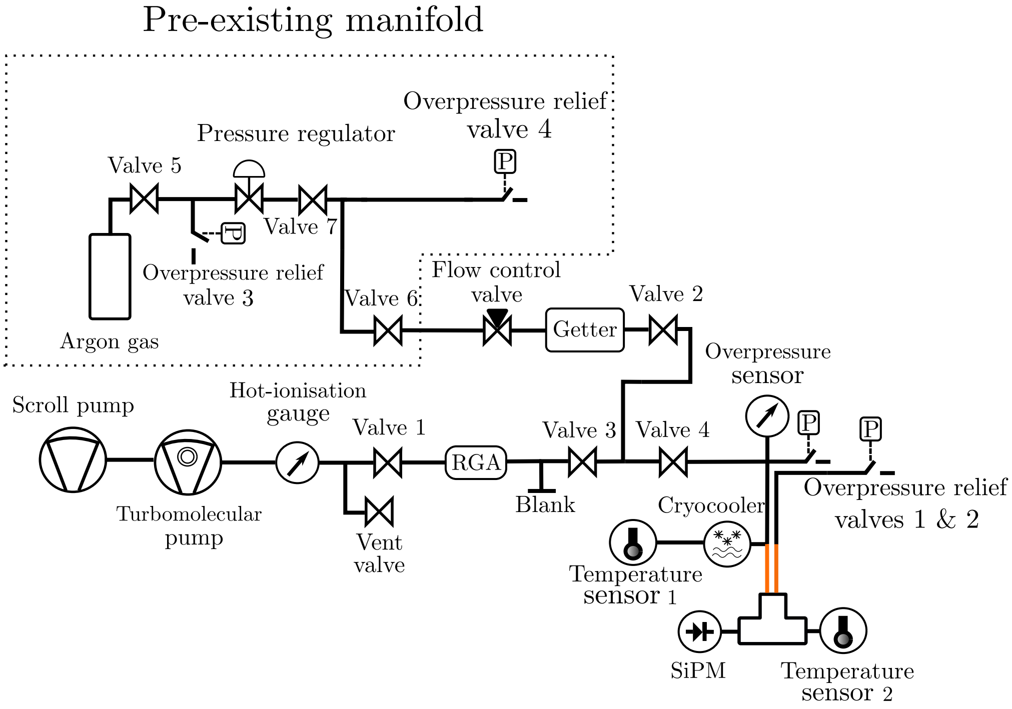

Figure 4.2: Diagram of the vacuum system responsible for the LAr celll and the gas lines volume.

Before flowing the argon gas into the LArCell prototype, the internal vacuum system must be in a vacuum. The process to vacuum the internal vacuum system is:

1. Close valve 6 and the vent valve.
2. Open valves 1, 2, 3, and 4.
3. Turn ON the hot ionisation gauge.
4. Turn ON the scroll pump and wait until the pressure of the system is at 23 mbar, which is the operating pressure of the turbomolecular pump.
5. Turn ON the turbomolecular pump until the pressure of the system reaches a pressure of 5×10^{-7} mbar.

As already stated, if the vacuum system has reached the desired pressure, it is a strong indication that no major leaks are present in the system. However, the quality of the vacuum system was tested using multiple leak tests, see Section 4.1.3.

Apart from the recommended start-up procedure of the internal vacuum system, the recommended shut-down of the vacuum system is also important. To ensure the safety of the personnel operating the LArCell prototype and also safely shut off the equipment, the following steps must be followed:

1. Close valves 6 and 1.
2. Switch off the turbo-molecular pump and wait until the rotation speed of the pump is equal to zero.
3. Switch-off scroll pump.
4. Open the vent valve slowly and allow the internal vacuum system to reach atmospheric pressure.

4.1.3 Leak Tests

Before moving to Section 4.3.4, which illustrates the procedure of introducing argon gas into the gas lines, one must ensure that there are no leaks in both systems. In the current set-up of the prototype, two different methods are chosen for leak testing. A rate-of-rise test is used for the volume around the gas lines, whereas, for the volume inside the gas lines, a helium leak test is performed. This discrimination is because, in the internal vacuum system, a Residual Gas Analyser (RGA) is installed, which has an embedded leak test mode and provides live monitoring on the purity level of the argon gas fed in the system. By applying helium to all joints that make up the internal vacuum system, one can immediately determine if there are any leaks in the system and also be able to pinpoint the location of the leak.

On the other hand, in the external vacuum system, a rate-of-rise test is used to determine if there is a leak in the vacuum system. Rate-of-rise (Q) is equal to

$$Q = \frac{V\Delta P}{\Delta t} \tag{4.1}$$

where V is the volume under test, ΔP is the pressure difference between the last and the first pressure recorded during the leak test, and Δt is the time difference between the last and the first pressure value recorded. As already stated, if the system can not reach the 23 mbar, which is the pressure that the turbo-molecular pump can be switched on, one can immediately assume that the system has a leak without performing rate-of-rise test. The system is designed with multiple valves, which gives the ability to the user to check for leaks progressively by isolating small sections of the system without the need for a helium leak detector. However, if the user has managed to bring the system under a vacuum, a detailed rate-of-rise test has to be performed. To perform a rate-of-rise test, one must close the valve which separates the scroll and turbomolecular pumps from the rest of the vacuum volume. The reason behind this is twofold. One, it allows the pressure to rise so the rate-of-rise can be calculated, and second, it prohibits the vacuum pump from backing leak air into the system when it is switched off.

The external vacuum system in which the rate-of-rise test is performed consists of Klein Flange (KF) and Conflat Flange (CF) fittings. KF fittings consist of stainless steel centring ring and a rubber o-ring placed around the centring ring. The KF fittings are not ideal in a high vacuum system as the rubber o-ring reduces the quality of the vacuum due to the trapped gas and vapour inside the rubber walls, which is slowly released back into the system (outgassing). Furthermore, gas or vapour that is dissolved, trapped, frozen, or absorbed in the vacuum system walls reduces even further the quality of the vacuum. To mitigate the effect of the outgassing, the vacuum process can be repeated multiple times, allowing the trapped gas to be removed from the system. Figure 4.3 shows an example of a leak test performed on the external vacuum system. One can immediately see that the fourth run of the vacuum process resulted in a higher quality vacuum.

The procedure of performing a rate-of-rise test in the external vacuum system, see Figure 4.1, is:

1. Start the vacuum process following the steps stated in Section 4.1.1.
2. Leave the system running for 5-8 hours and then follow the shutdown procedure stated in Section 4.1.1 with two exceptions:
    (a) Before switching off the scroll pump, close vale 1.

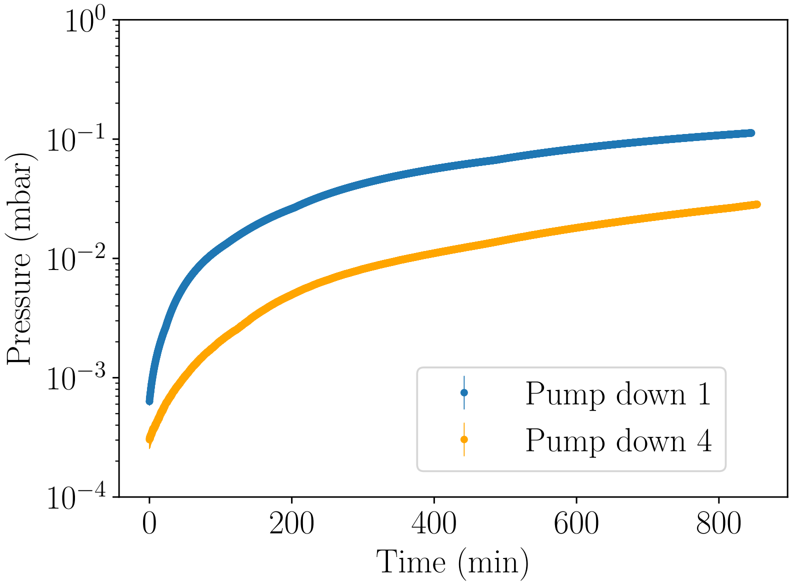

Figure 4.3: Plot of pressure versus time during a leak test. The blue lines show how pressure varies over time during the first pump down of the leak test. Orange line shows the fourth pump down of the leak test which the outgassing effect of the system is reduced due to the multiple vacuum runs.

   (b) Vent valve must remain closed.

3. Repeat the above steps four times.
4. After the end of the last run, the rate-of-rise is calculated.

For high-vacuum systems which is the systems used in the PET prototype, the following rule of thumb applies. If the leak rate value is:

- $Q < 10^{-6}$ mbar.l/s: System is “very tight”.
- $Q < 10^{-5}$ mbar.l/s: System is “sufficiently tight”.
- $Q > 10^{-4}$ mbar.l/s: System is “leaky”.

4.2 Data Acquisition System

To monitor the state of the LArCell prototype and store the data acquired from the SiPM, a Data Acquisition System (DAQ) system was built. The DAQ system consists of the slow control system and the digitiser. The slow control system consists of the monitoring instruments such as pressure, temperature and level sensors. Its purpose is centralised around the safety requirements and reliability of the PET photon detector. The digitiser also called as Digital to Analog (DAC) system throughout this thesis, is responsible for the digitising and readout of the scintillation photons produced from the interaction of the 511 keV gamma-rays with LAr. To ensure the reliability and stability of the experiment, the software infrastructure of EPICS (Experimental Physics and Industrial Control System) [41] was chosen.

4.2.1 EPICS

EPICS is a versatile, reliable and standard control system based on the concept of databases and input-output controllers (IOCs). A database is a program to store values from multiple devices. IOCs provide instrumental data to the databases. These data are called process variables (PVs). The number and the record type of the data which will be stored in the databases must be defined prior to the data acquisition. EPICS support a large extensible set of record types such as "ai" (analog input) and "ao" (analog output). When a user wants to access or save the PVs from an instrument, by using preset commands such as "caget" and "camonitor", a path to that PVs is created by EPICS, called a channel. Channels are connections established over a virtual circuit between a server and client through which a single PV is accessed. Hence all the preset commands start with the acronym "ca" which means channel access, and then the desired command needed from the user, such as get, put and monitor. The versatility of using EPICS comes from the fact that EPICS does not constrain the user to use a specific programming language for its communication with the instruments. For example, in this thesis, all the scripts which are related to the slow control system are written in Python programming language, whereas the scripts related to the DAC system are written in C [45].

Figure 4.4 shows a schematic of the LArCell prototype EPICS design. The instruments used in the LArCell prototype are (a) the Crycon24C [42], which monitors the temperature of the gas lines and tee shape vessel, (b) the Hornet that monitors the pressure of the external vacuum system [43], (c) an Omega PX219 pressure transducer which monitors the pressure inside the gas lines and the tee-shape LAr vessel [44], and (d) a custom made level sensor which measures the change in the capacitance of the sensor as a function of LAr fill level within the vessel.Each instrument has it's unique script to communicate with the slow control system. Then the data are stored in each instrument unique database using the command "caput". Lastly, a python script is used to monitor the state of the slow control system, raise alarms based on the thresholds set on the instruments, and store the data.

The DAC system EPICS structure is similar to that of the slow control system with two exceptions, see Figure 4.4. In contrast with the slow control where all the scripts are written in python, the software script which monitors and stores the data from the digitiser to the EPICS database is written in C.

The C programming language is chosen as the manufacturer [47] provided libraries are written in C, and therefore it was easier to develop the DAC system code in C. The second exception is the record type of epics database in which the data from the digitiser are stored. The type is called waveform and allows the storage of array like PVs at the same time, whereas in the slow control system, the record type is analog-input, and it allows the storage of one PV each time. The two PVs stored in the digitiser epics database is the number of ADC counts stored in each buffer block and their value. The range of the ADC values for the digitiser is 4096 (12-bit), and it will be described further in Section 4.2.3.

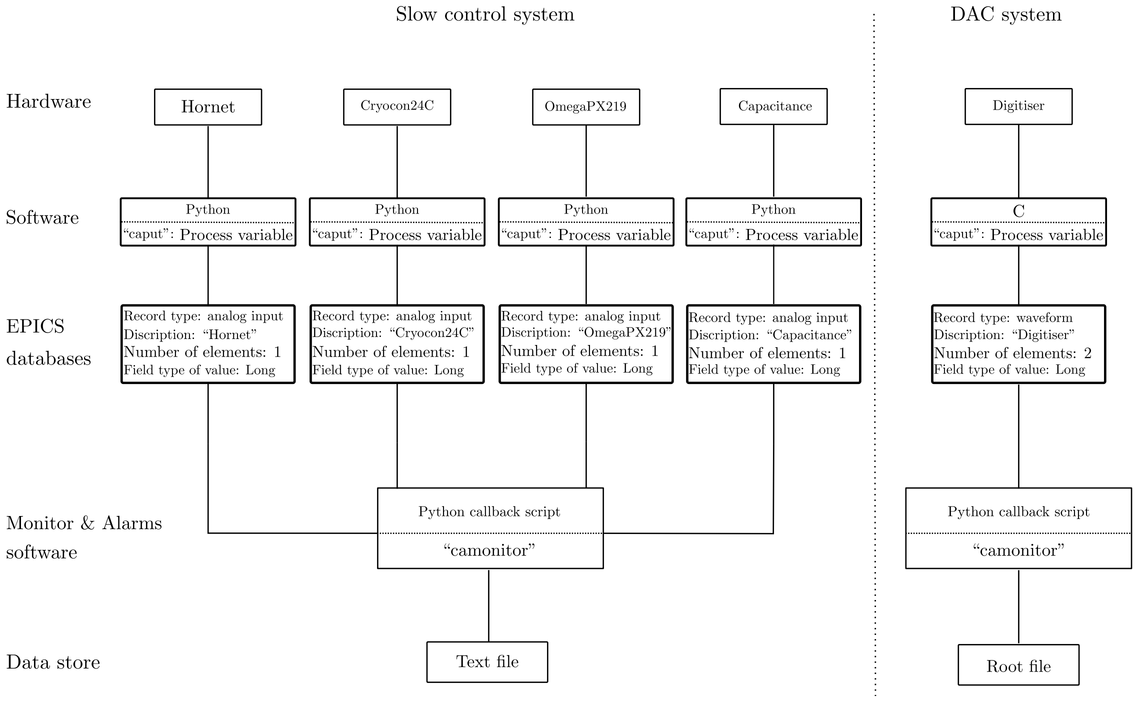

Figure 4.4: Diagram showing LArCell prototype EPICS infrastructure.

4.2.2 Slow Control

As already stated, the slow control system consists of four instruments that monitor the vacuum pressures, the temperatures, the gas lines pressure, and capacitance which indicates when the argon gas has changed phase from gas to liquid. Figure 4.5 shows the live updated plots of the slow control system during the LArCell prototype operation.

Before the run of the experiment, all instruments are tested. As the Cryocon24C and the Hornet had live updated values shown on their control panel, the comparison between the python script, which updates the process variables (PVs) in EPICS and the values shown on the instrument's screen

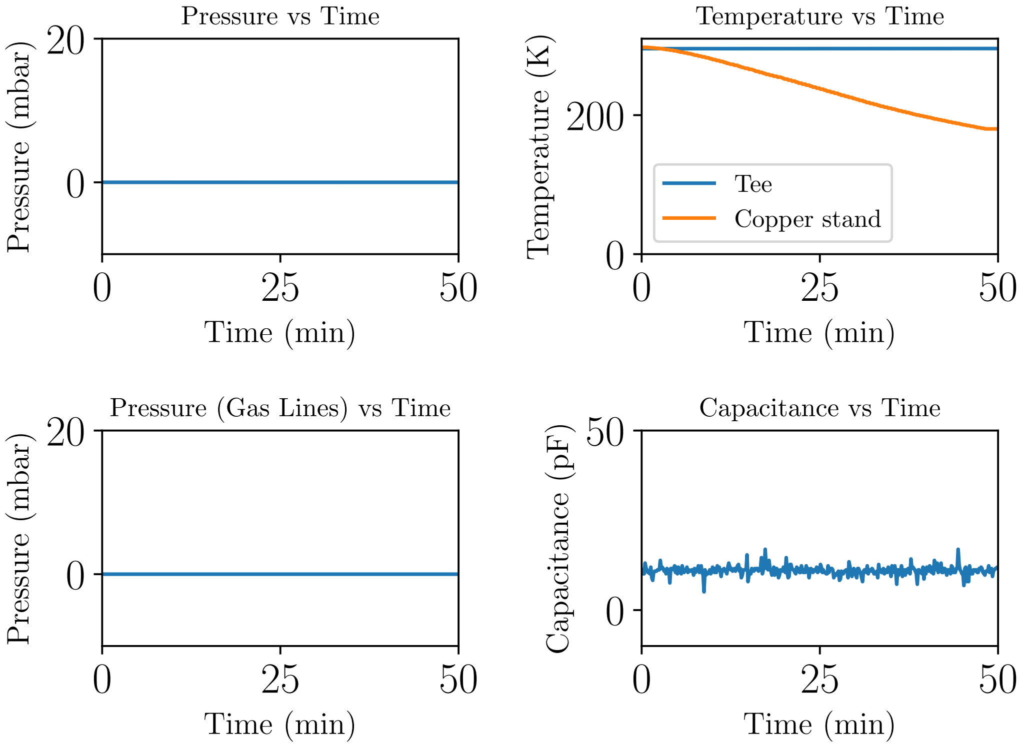

Figure 4.5: Screenshot of the live updated plots of the slow control system during the LArCell prototype operation.

was easy to compare. On the other hand, the Omega PX219 pressure transducer and the custom made level sensor needed thorough testing and calibration.

The pressure transducer consists of a diaphragm which deforms when pressure is applied to it, and then it converts it into an electrical signal. The PX219 pressure range is from 0-60 psi which is converted to a voltage between 0-5 V. An Arduino Uno device is used to measure the voltage change during the diaphragm deformation. To calibrate the PX219, two tests are performed. First, the internal vacuum system is placed under vacuum, and then the vent valve is opened, see Figure 4.6. Then the voltage output is calibrated to show the atmospheric pressure (1013 mbar). Furthermore, to test the overpressure relief valves, argon gas with a pressure of 1700 mbar flows into the system. The overpressure spring relief valves open automatically at 15 psi (1034 mbar), and therefore, they should open and release the excess argon gas, see Figure 4.6. As the overpressure relief valves use springs internally, they degrade over time, and as shown in Figure 4.6, they had opened at 1250 mbar instead of the 1034.21 mbar (15 psi). As this deviation is acceptable, there is no need to replace the springs;

however, this small deviation is accounted for during the argon liquefication process, see Section 4.3.4.

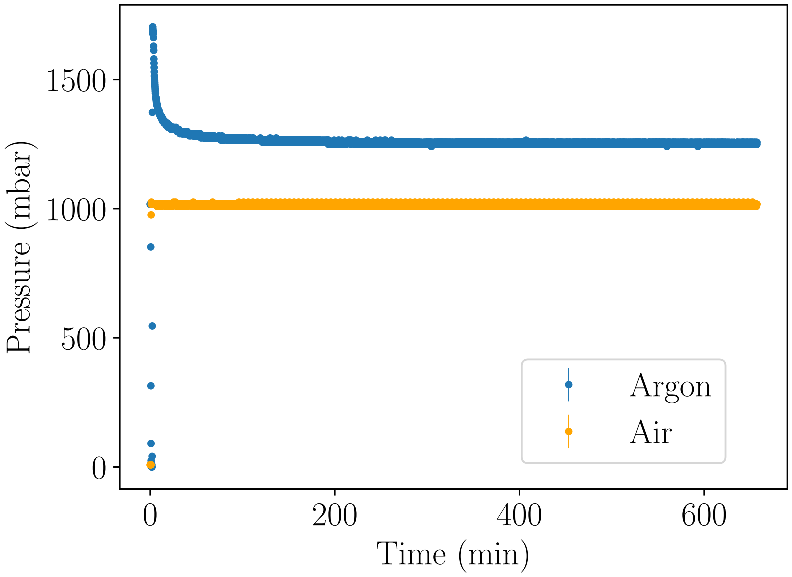

Figure 4.6: Plot of pressure as a function of time during the calibration of the Omega PX219 pressure transducer. The error bars are smaller than the points on the plot.

Moreover, the last instrument for testing is the custom made capacitance sensor. On the top CF flange of the tee-shape LAr vessel, a 0.5 inch diameter stainless steel pipe is welded. Inside this 0.5 inch pipe, a 0.25 inch diameter stainless steel pipe is inserted with a Vacuum Coupling Radiation (VCR) fitting and a metal gasket to ensure a tight vacuum seal. To ensure that the two pipes are not touching each other, a 0.125 inch diameter Teflon tube is wrapped around the 0.25 inch pipe in a spiral configuration. The voltage between the two cylinders is measured using an Arduino Uno, and it can be shown that the capacitance C between the two cylinders is equal to:

$$C = \frac{Q}{V} = \frac{2\pi k \epsilon_o L}{\ln(\frac{R_b}{R_a})} \tag{4.2}$$

where Q is the electric charge, V the measured voltage, ϵ_o the permittivity of free space, k the dielectric constant, L the length of the cylinders, R_b the radius of the 0.5 inch diameter cylinder, and R_a the radius 0.25 inch diameter cylinder. Figure 4.7 shows a test in which the cylindrical capacitance sensor is submerged in liquid nitrogen (LN_2). The dielectric constant of air is equal to 1, whereas liquid nitrogen is 1.5 [46], and therefore as expected when the capacitance sensor is submerged in liquid nitrogen, a steep increase in capacitance must be observed, see Figure 4.7. The dielectric constant of LAr is 1.6, see Table 2.1, and as a result, when the tee vessel is filled with LAr, a similar steep increase in capacitance as in the liquid nitrogen test will also be observed.

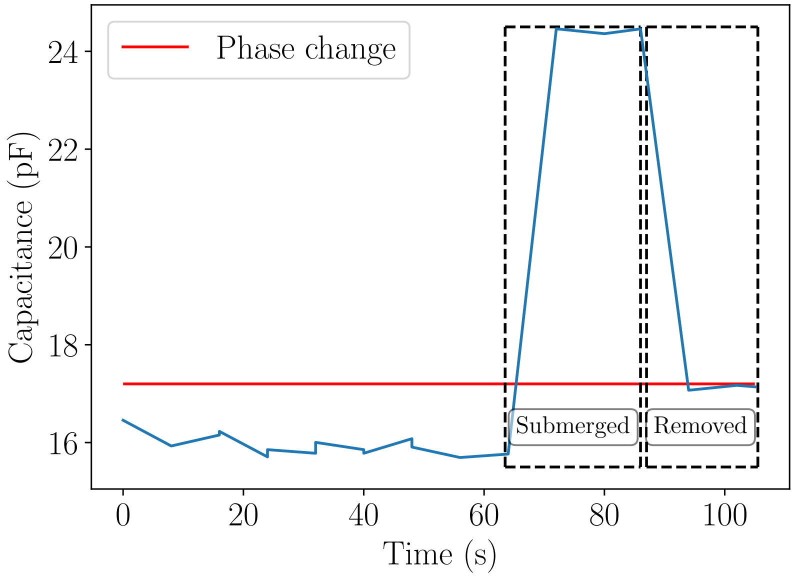

Figure 4.7: Plot of the capacitance as a function of time. At time equal to 63.5 seconds the capacitance sensor is submerged in LN_2, and at time equal to 86 seconds is lifted out of the LN_2.

4.2.3 Digitiser

The digitiser module used was CAEN V1720 [47]. The V1720 is an 8 channel 12 bit 250 MHz ADC waveform digitiser. This digitiser is chosen due to its fast digitising capabilities (4 ns between samples), which, as already stated, see Table 2.2, is faster than the fast decay time of argon which is 6 ns. The V1720 is connected via an optical link to a PC, and it is housed in a VME 6U unit with a discriminator [49] and a Fan-In Fan-Out [48] module. The discriminator sets the threshold voltage to be accepted as a true signal during the operation of the experiment. The Fan-In function is to add or combine multiple analog signals for later processing, and the Fan-Out function makes multiple outputs from one or more analog inputs. Depending on the number of inputs, there is a propagation delay. For example, when there are four input signals, the delay is 4 ns ± 1 ns. During the first run of the experiment, the number of SiPMs attached to the LAr cell is one, and that number will progressively increase. Figure 4.8 shows the DAC system configuration.

The digitiser code is created from scratch, and as already stated, is written in C programming language, and it can be found in the Git repository [50]. To verify the correct function of the digitiser, a function generator is used. Figure 4.9 shows an example of a sine wave that is digitised using the V1720 and plotted, showing the DAQ worked as expected.

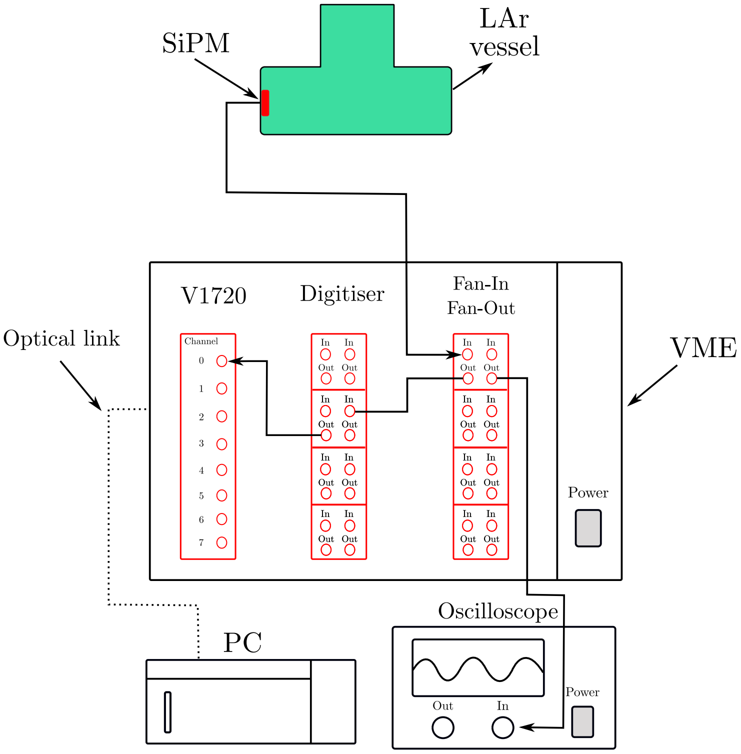

Figure 4.8: Diagram of the DAC system configuration.

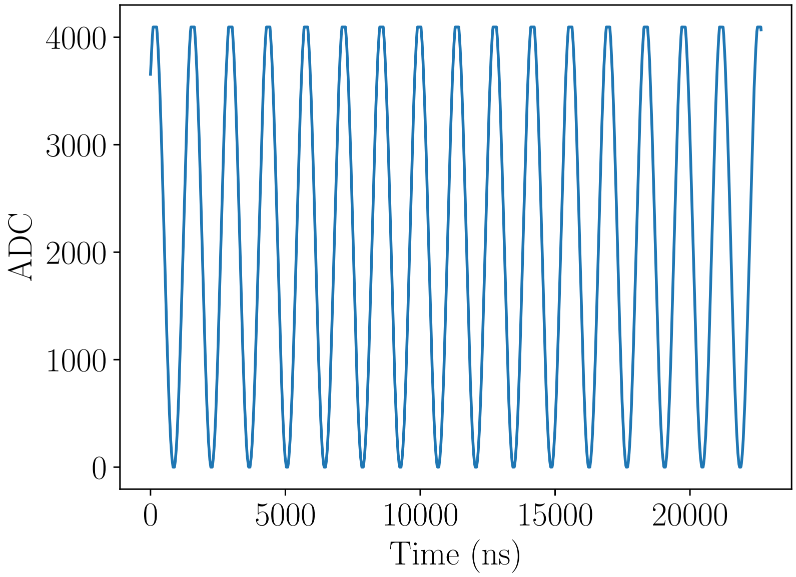

Figure 4.9: Plot of ADC as a function of time, during a test of the V1720 digitiser code using as an input signal a sine-wave created by a function generator. The input signal voltage is ±1 V which is the maximum input voltage the V1720 can digitise. The purpose of this plot is to confirm that the digitiser is working as intended.

4.3 Cryogenic System Design

To reach a cryogenic temperature in general, the design of the cryogenic system is of paramount importance. This thesis uses a cryogenic refrigeration system based on a closed-loop helium expansion cycle cryocooler. The argon gas input gas line and the tee cell are in thermal contact with the cold head, and therefore, the argon gas will be condensed and drip inside the tee shape vessel, see Figure 4.10. The basic idea is shown in Figure 4.10, but to successfully reach the boiling temperature of argon, a careful choice of the materials used in the construction of the experiment and the reduction of any heat leaks in the system are crucial. This Chapter describes the design of the cryogenic system and the process of liquefying argon.

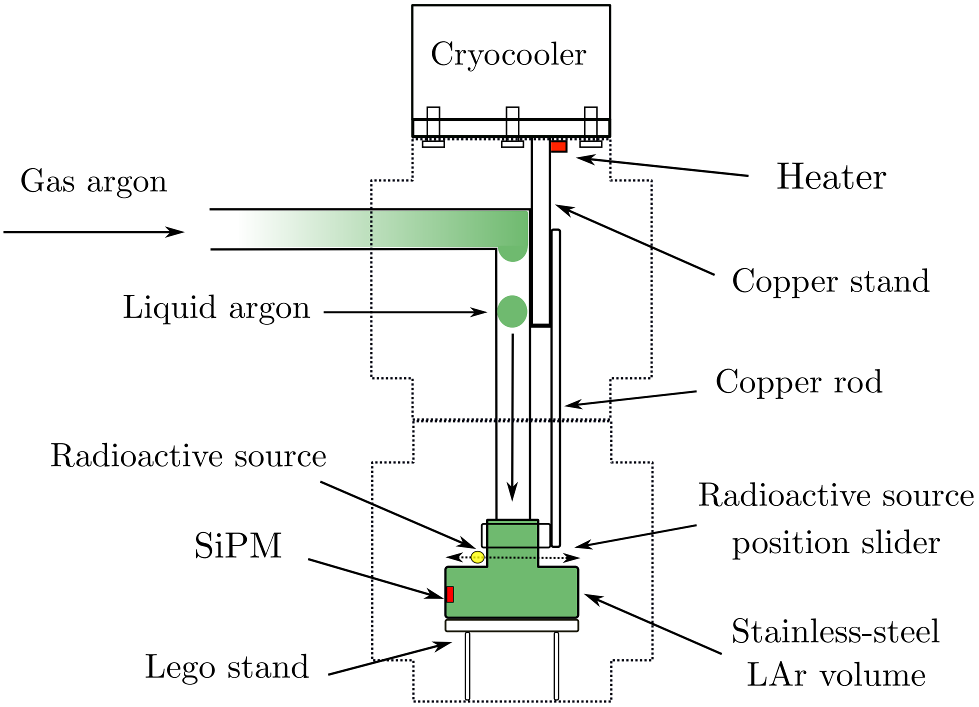

Figure 4.10: Drawing showing the basic concept of liquifying argon gas.

4.3.1 Cryocooler

The cryogenic refrigeration system consists of two major components, one is the compressor package, which compresses the refrigerant and removes heat from the system, and second is the cold head (cryocooler), which takes the refrigerant through one or more additional expansion cycles to cool it down to cryogenic temperature. A detailed system drawing of the compressor and the cold head can be found in reference [52]. The cold head consists of two heat exchange stages, see Figure 4.11, and combining the two stages; the cold head can reach a temperature of 10 K with no load in 60 minutes [53]. Figure 4.12 shows the cryorefrigerator capacity curve [54]. As the cryocooler does not have the capability to adjust its cooling power to maintain a constant temperature at the boiling point of argon, a power of approximately 87 W must be given to the system (assuming there are not any heat leaks), see Figure 4.12. Therefore, a heater is attached to the second stage of the cold head, which allows to adjust the temperature of the cold head, see Figure 4.10. Besides, the heater also reduces the time that the system requires to reach room temperature from the cryogenic temperature when adjustments to the system are needed.

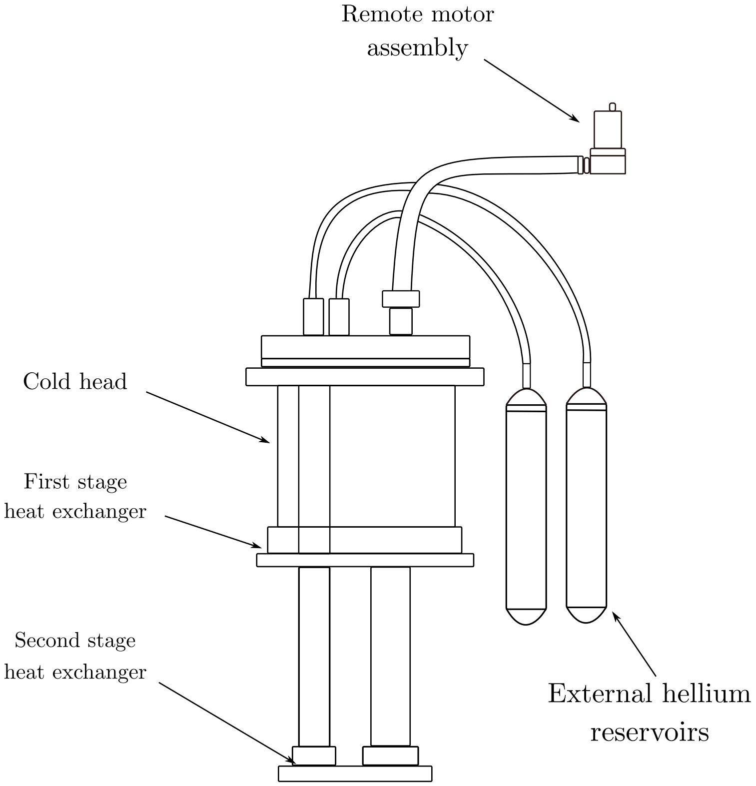

Figure 4.11: Schematic of the PT810 cold head.

4.3.2 Materials Choice

Before designing a cryogenic system, an understanding of the properties of the materials chosen in the design is essential. Properties such as thermal conductivity and specific heat are crucial when designing the cryogenic system, as they will approximately express the time needed to cool down the

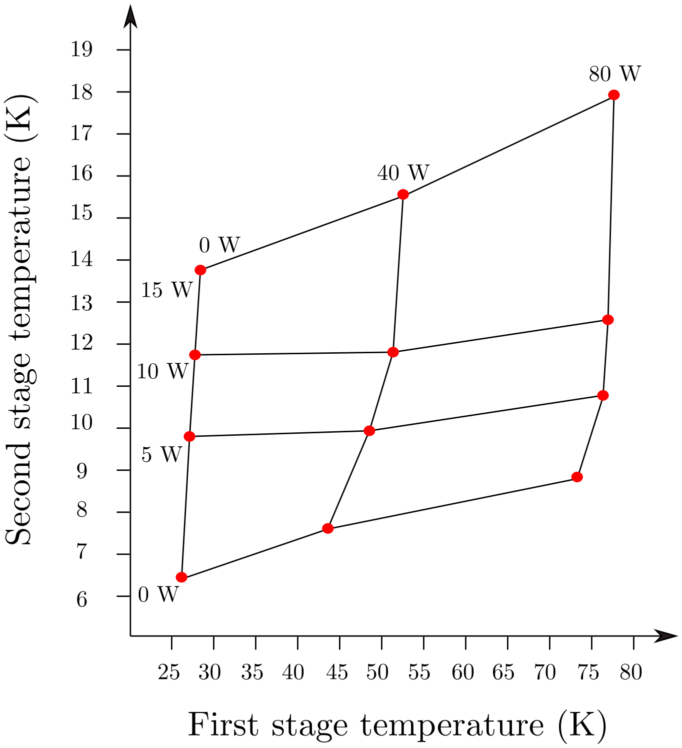

Figure 4.12: Cryorefrigerator PT810 cooling capacity curve [53].

cell which LAr will be contained, using thermal conduction. Thermal conductivity (k) is defined as the rate at in which heat is transferred by conduction through a unit of a cross-section area of a material when a temperature gradient exists. The second important material property is the specific heat at constant pressure (C_p), defined as the amount of heat per unit mass required to raise the temperature of the material by one Kelvin (K). The time needed to reduce the temperature of a material from room temperature to the desired cryogenic temperature (cool down) is five times the time τ (same principle as capacitor's charge time), which is equal to

$$\tau = R_{\text{thermal}}(T) \cdot C_p(T) \cdot m \tag{4.3}$$

where $R_{\text{thermal}}(T)$ is the thermal resistance as a function of temperature, $C_p(T)$ the specific heat as a function of temperature, and m the mass of the material. R_{thermal} of a material is equal to

$$R_{\text{thermal}} = \frac{L}{Ak(T)} \tag{4.4}$$

where L is the length of material, A the cross-sectional area of the material, and $k(T)$ the thermal conductivity as a function of temperature.

As shown in Section 4.1.2, the two materials used for constructing the LArCell prototype are stainless steel and copper. The reason behind this mix of materials is the cool-down time. To successfully liquify argon and fill the vessel with it, it is apparent that the temperature of the vessel which contains LAr must be at the same temperature. Stainless steel is chosen due to its very low rate of outgassing in a vacuum and also its ability to withstand high vacuum pressures without any deformations. However, stainless steel has a comparatively high thermal resistance, and therefore, to cool it down from room temperature to a cryogenic temperature is going to be very long. Therefore, adjustments to the cryogenic system are needed to reduce the cool-down time. Copper thermal conductivity is very low compared to stainless steel, see Figure 4.13, and by introducing it to the system, the cool-down time of the LAr cell is going to be reduced.

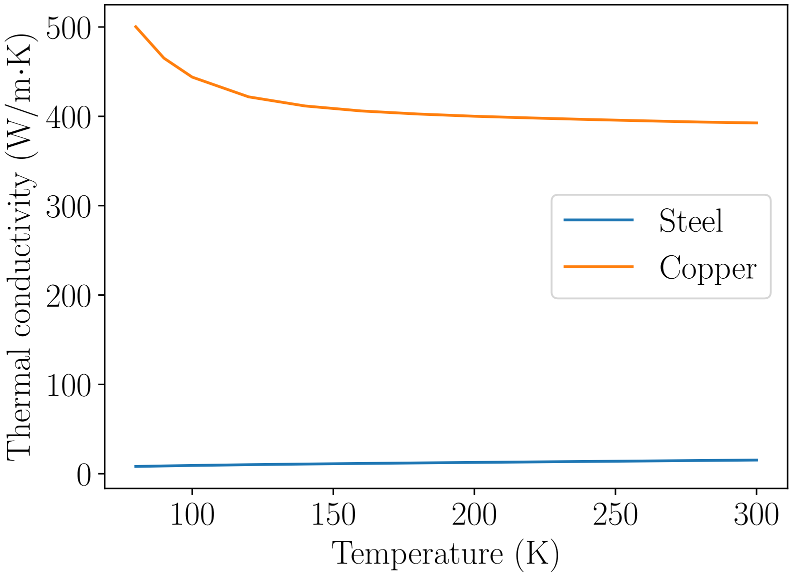

Figure 4.13: Comparison between the thermal conductivity of stainless-steel and copper [51].

Moreover, the specific heat of stainless steel is also greater than that of copper, see Figure 4.14. As a result, the addition of copper into the system reduces even further the cool-down time of the LAr cell. However, as copper has high levels of outgassing and can be deformed in high vacuum pressures, only some sections of the prototype are chosen to be copper. The cool-down time of the stainless steel cell at the boiling point of argon is evaluated mathematically at first and then experimentally. It is worth noting that latent heat also plays a role in the cool down time of the LAr cell, and it will be described in Section 4.3.5.

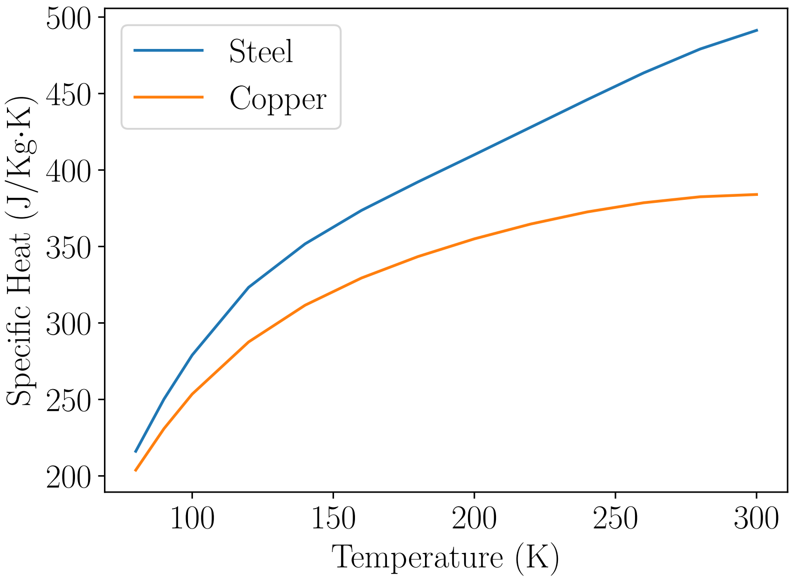

Figure 4.14: Comparison between the specific heat of stainless-steel and copper [51].

4.3.3 Cool-down Time

Theoretical Calculation

To ensure that the process to liquify argon will occur in a short time frame, the theoretical time to bring the stainless steel tee vessel and the copper gas lines from room temperature to argon boiling point is calculated using equation 4.3. As the thermal conductivity and the specific heat of a material change with temperature, the mean thermal conductivity and specific heat are used in the calculations of bringing the copper gas lines and the stainless steel tee vessel from room temperature to the boiling point of argon. The mean thermal conductivity $\overline{K(T)}$ is equal to

$$\overline{K(T)} = \int_{T_C}^{T_H} \frac{K(T)dT}{T_H - T_C} \tag{4.5}$$

where T_H is the temperature of the hot side of the material, T_C the temperature of the cold side of the material, and $K(T)$ the thermal conductivity as a function of temperature. The NIST data [51] was fitted using a fourth-order polynomial, see Figure 4.15 and 4.16.

The mean specific heat $\overline{C(T)}$ is equal to

$$\overline{C(T)} = \int_{T_C}^{T_H} \frac{C(T)dT}{T_H - T_C} \tag{4.6}$$

where T_H is the temperature of the hot side of the material, T_C the temperature of the cold side of the material, and $C(T)$ is the specific heat as a function of temperature. Using the same process

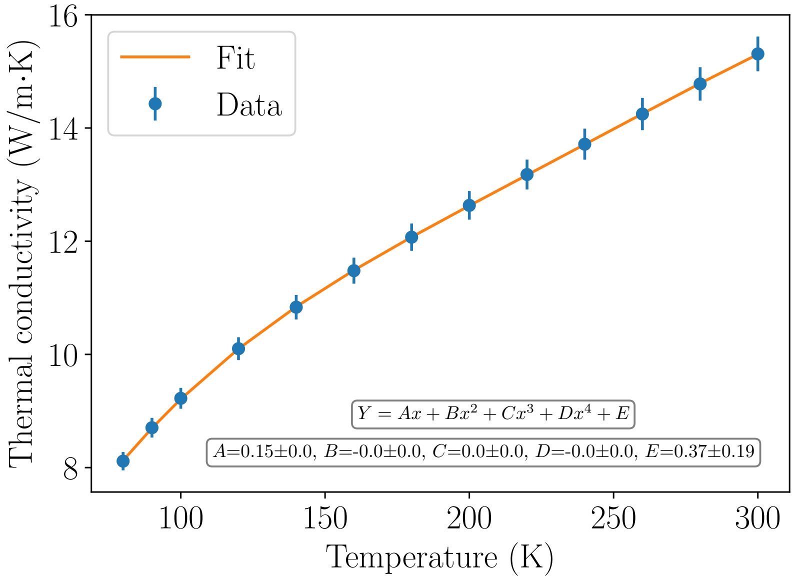

Figure 4.15: Stainless steel thermal conductivity as a function of temperature [51].

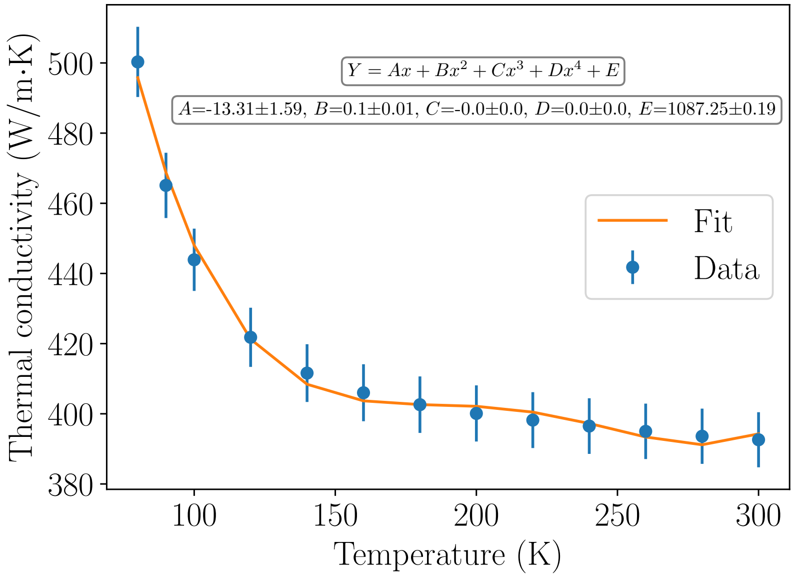

Figure 4.16: Copper thermal conductivity as a function of temperature [51].

for fitting the thermal conductivity function, the data acquired from NIST [51] are fitted, and the equations describing the change of specific heat with temperature for stainless steel and copper is a fourth-order polynomial, see Figure 4.17 and 4.18.

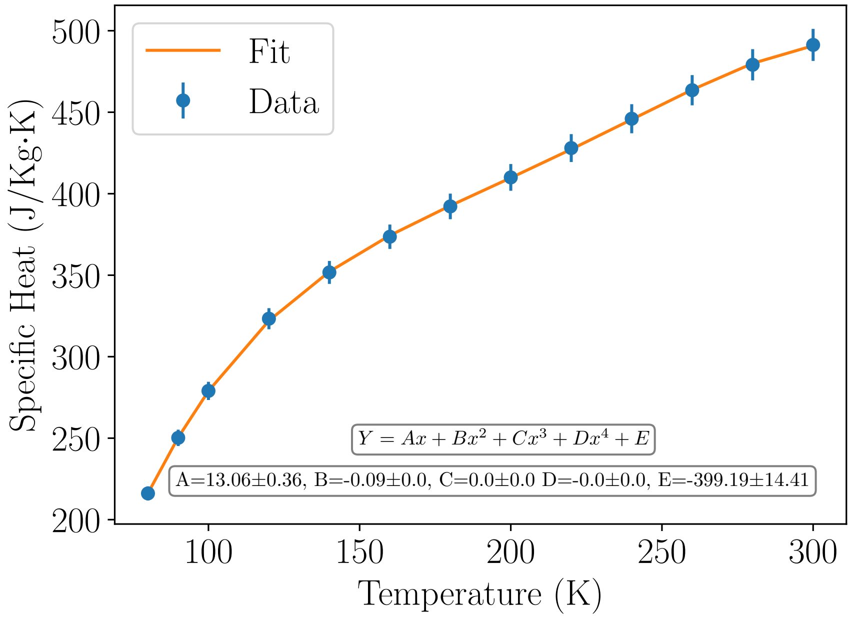

Figure 4.17: Stainless steel specific heat as a function of temperature [51].

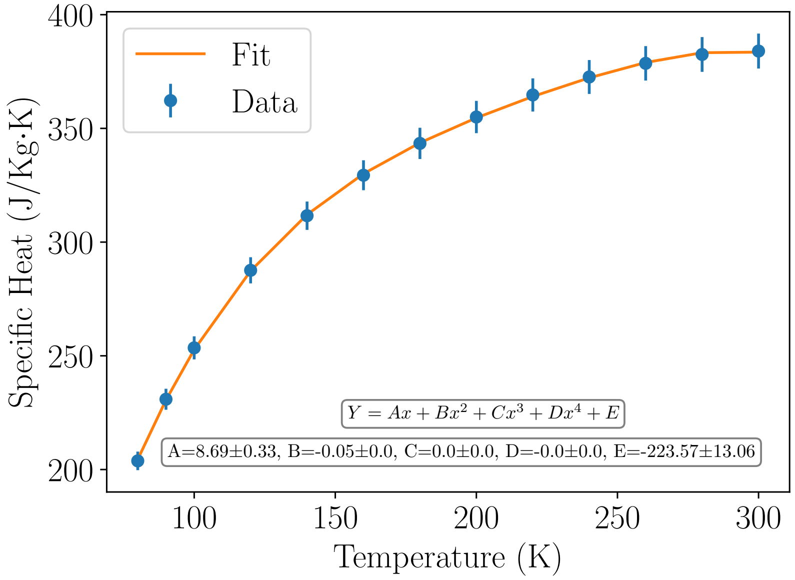

Figure 4.18: Copper specific heat as a function of temperature [51].

Using Equations 4.3, 4.5 and 4.6, the theoretical time to bring the system to the boiling point of argon is 1258.5 min. The stainless steel tee has a mass of 2.65 kg, a wall thickness of 1.65 mm, and a length that is not in direct contact with the cold head of 45 mm. The mean thermal conductivity and specific heat of the stainless steel tee vessel are 12.3 $\frac{W}{m \cdot K}$ and 398.9 $\frac{J}{Kg \cdot K}$, respectively. The copper gas line is in direct contact with the cold head and as copper thermal conductivity is high, see Figure 4.16, its temperature changes almost alongside the cold head, and therefore is not included in the calculations. It is worth noting that this theoretical calculation assumes that there are no heat leaks in the system, and its purpose is to give an approximate expected time for bringing the stainless steel tee vessel to the boiling point of argon. As already stated, the latent heat of vaporisation will reduce even further the cool-down time of the system, and the detailed calculation is shown in Section 4.3.5.

Experimental Calculation

Before flowing argon into the system, the cool-down time of the stainless steel vessel from room temperature to the boiling point of argon was measured. During the construction of the experiment, factors such as heat leaks and poor thermal conduct can affect dramatically the cool-down of the tee vessel, a test which first ensures that the vessel can successfully reach the boiling point of argon, and second the cool-down time is in a reasonable timescale (less than a day). By successfully bringing the tee vessel from room temperature to the boiling point of argon, it means that it can contain argon in its liquid phase. To test that, two temperature sensors (silicon diodes) are used [56]. The first temperature sensor is placed on the copper stand with which the argon gas line is in thermal conduct, and the second temperature sensor is placed on the outer wall of the tee vessel.

During the construction of the experiment, the initial plan was that the copper stand on which the argon gas line is attached and the stainless steel tee vessel are going to be held directly on the cold head without any support below the tee vessel. However, as the maximum load which the cold head can support is 5 Kg, and the total weight of the copper stand, gas line, tee vessel and LAr which will be contained in the vessel is 6 Kg, a support stand had to be placed underneath the tee vessel, see Figure 4.10. As a result, a material that will act as a thermal break between the outer stainless steel flange, which is at room temperature, is needed. Acrylonitrile Butadiene Styrene (ABS) modules, known as LEGO blocks, is used as a thermal break. LEGO blocks have a very poor thermal conductivity at 87.15 K (≈ 0.21 $\frac{W}{m \cdot K}$), see Figure4.19, and it makes it a good choice for a thermal break material [55].

During the first run of the cool-down process, to ensure good support of the tee vessel, solid LEGO blocks with a total area 90.25 cm^2 and length of 12 cm are used. Although the support for the tee vessel was good, the surface area of the LEGO stand was too big, and therefore the heat leak in the system was too high, see Figure 4.20. The rate of heat transfer $\dot{Q}$ is equal to

$$\dot{Q} = \frac{kA(T_H - T_C)}{L} \tag{4.7}$$

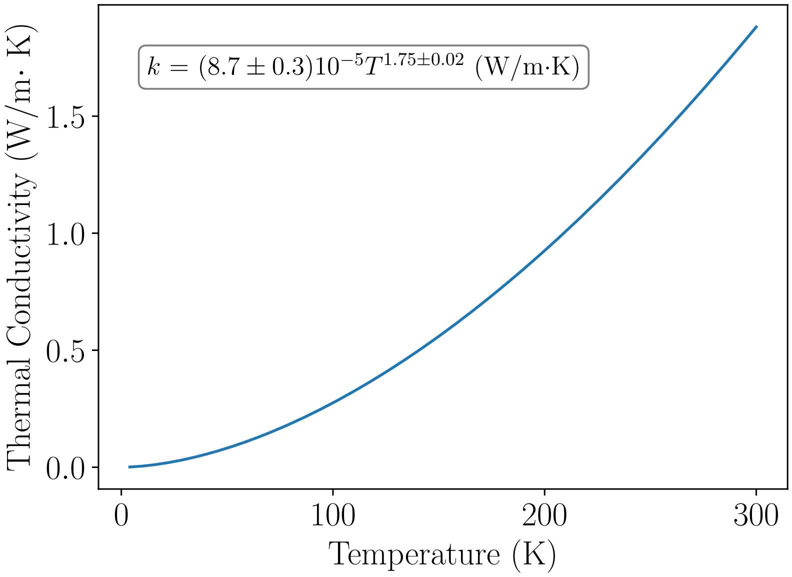

Figure 4.19: Lego blocks thermal conductivity as a function of temperature [55].

where k is thermal conductivity, A the area, T_H the hot side of the material, T_C the cold side of the material, and L the length of the material. As a result, to reduce the heat loss of the system, the area of the LEGO blocks needed to be reduced, as the length from the tee vessel to the bottom outer flange can not be changed. The area of the LEGO blocks in thermal conduct with the outer flange (room temperature) was reduced by a factor of two, and the cool-down process was performed again. As shown in Figure 4.20, the temperature of the tee vessel plateau at 210 K, which means the heat loss in the system is greater than the heat which the cold head removes from the system, see Figure 4.12. Consequently, the LEGO blocks support is changed more dramatically to ensure as little heat loss as possible. By building 8 LEGO blocks legs with dimensions 5×5 mm, the tee stand was able to be supported, and the total area which is in thermal conduct with the outer flange is 2 cm^2. As shown in Figure 4.20, the temperature on the tee vessel is dropped to 125 K, which proves that the reduction of the LEGO stand surface managed to reduce the heat loss in the system, but still, the temperature of the boiling point of argon is not reached. Lastly, in the fourth run, only four LEGO block legs are used with the same dimension as in the third run to support the tee vessel but to ensure that the legs can steadily support the tee vessel, cyanoacrylate (super glue) is used to glue the LEGO blocks together. Figure 4.20 shows that in the fourth run, the lowest temperature the tee cell reached was 81.7 K which is below the boiling point of argon. This result ensures that the stainless steel cell can successfully contain LAr. As already stated, a heater placed under the cold head ensures that the temperature can be adjusted and stabilised at the boiling point of argon. Using the stainless steel tee vessel fitted data of the fourth run, the cool-down time from 300 K to 81.8 K is 1434.5 minutes (5τ), see Figure 4.21.

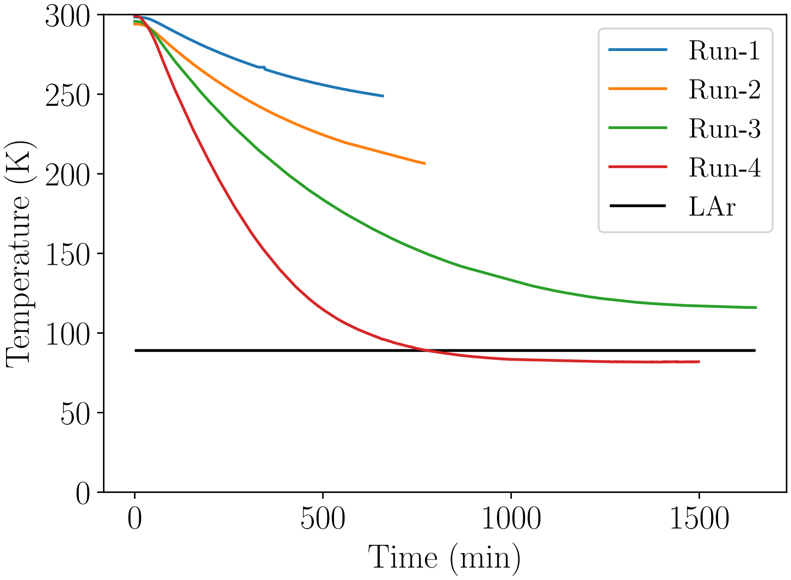

Figure 4.20: Comparison between the cool-down time of the stainless steel tee cell runs.

As already stated, one more temperature sensor is placed on the copper stand, which is bolted directly underneath the cold head. The argon gas line is in thermal conduct with the copper stand, and Figure 4.22 shows the comparison of the temperature as a function of time during the four cool-down runs. From the fitted data of the fourth run, the cool-down time from 300 K to 23.6 K is 170.5 minutes (5τ), see Figure 4.23.

4.3.4 Argon Liquefication

To ensure that the gas lines and the tee vessel walls are not contaminated with water or nitrogen molecules, a warm and cold flush process is needed prior to the argon liquefication process. During a warm flush, the internal vacuum system, see Figure 4.2, is filled with warm, room temperature argon gas at 1 Bar. Then the system is vacuum purged until the pressure in the internal vacuum system is at 5×10^{-2} mbar. This process is repeated three times. After the warm flush is completed, the cold flash process is performed. During the cold flash, the cryocooler is switched on, and the heater is set at 150 K. Then argon gas is fed into the system, and when both temperatures of the copper stand and the tee vessel are stabilised at 150 K, the system is vacuum purged as in the warm flush. Again

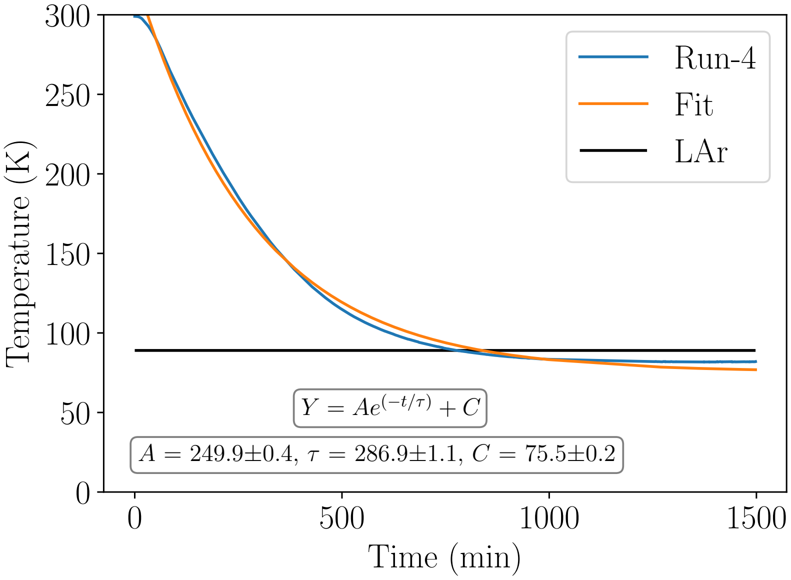

Figure 4.21: Cool-down time of the stainless steel tee cell.

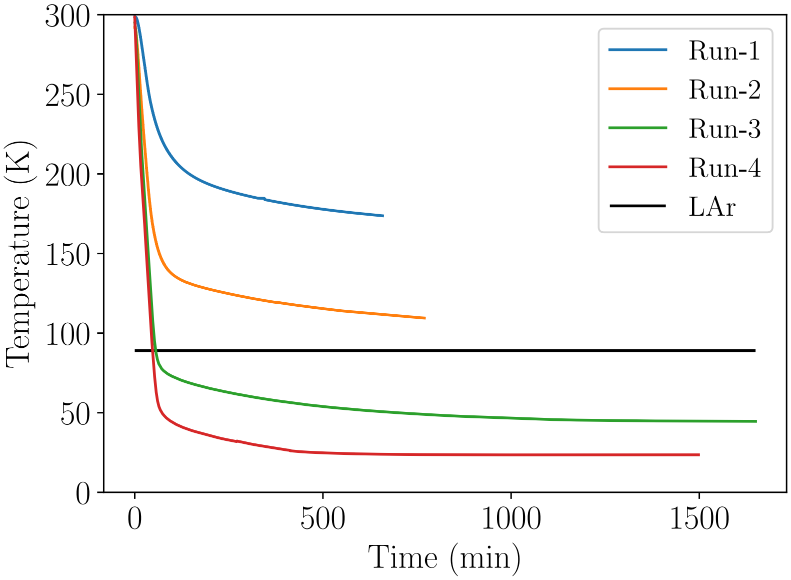

Figure 4.22: Comparison between the cool-down time runs of the copper stand which the argon gas line is in thermal conduct with, during the change of the area of the LEGO stand.

this process is repeated three times. After the warm and cold flush process is completed, the system is ready, and the tee vessel can be filled with LAr.

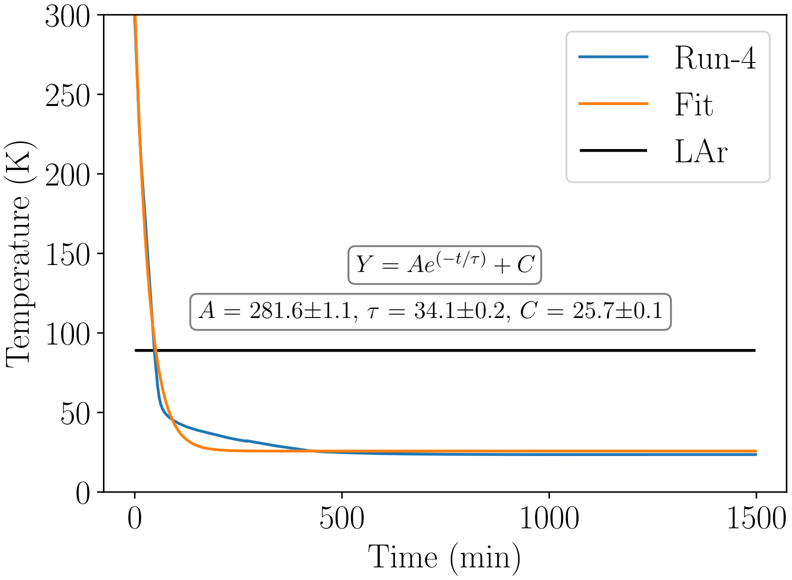

Figure 4.23: Copper stand cool down time.

To ensure that the change in temperature from room to the boiling point of argon, does not occur too quickly, the heater is set at 150 K, and the system is allowed to thermally stabilise. Then the heater temperature is dropped with increments of 10 K until a temperature of 87.15 K is reached. As the spring relief valves are stabilising the pressure in the system at 1 Bar, and sometimes they lose their firmness, it is important to always monitor the pressure of the gas lines and the tee vessel and adjust the boiling point accordingly using the Cassius-Clapeyron equation. The boiling point temperature at the pressure of interest T_B is equal to

$$T_B = \left(\frac{1}{T_o} - \frac{R \ln(\frac{P}{P_o})}{\Delta H_{vap}} \right) \tag{4.8}$$

where T_o is the boiling point temperature at pressure P_o, R is the ideal gas constant, P the new pressure which the new boiling point is calculated, and ΔH_{vap} the heat of vaporisation. Table 4.1 shows argon boiling points at various pressures.

Oxygen Depletion Assessment

The bottle stored in the manifold has 10000 litres of argon gas stored in it. Although only 312 litres of argon gas is needed to fill the tee vessel with 0.39 litres of liquid argon, an assessment of which all the argon gas stored in the manifold is released into the room where the experiment is contacted is

Temperature (Kelvin)	Pressure (bar)
87.15	1.00
89.30	1.25
91.80	1.60
94.20	2.00
96.80	2.50

Table 4.1: Argon boiling points based on pressure [16].

performed. The remaining volume of oxygen in the room V_{O_2} is equal to

$$V_{O_2} = O_{2\%}(V_{\text{room}} - V_{\text{bottle}}) \tag{4.9}$$

where $O_{2\%}$ is the percentage of oxygen in the atmosphere and is equal to 20.85%, V_{room} is the volume of the room which the experiment is contacted and is equal to 360 m^3, and V_{bottle} is the volume of argon gas stored in the bottle (10 m^3). The remaining volume of oxygen in the room V_{O_2} is 73.33 m^3, and by dividing it by the volume of the room, it is found that the remaining oxygen percentage left in the room is 20.87%, and this value is above the lower limit of 18% set by the department safety regulation.

4.3.5 Latent Heat

Argon latent heat of vaporisation can be used to decrease the cool-down time of the stainless steel tee vessel even further than just using the method of conduction. Latent heat of vaporisation is defined as the energy needed to add to a liquid substance to transform a quantity of the substance into gas under standard pressure. Assuming that the tee vessel is at room temperature initially and LAr is fed into the system, heat will flow from the tee cell to the liquid argon droplets. As a result, the heat will be removed from the tee, and LAr will change phase from liquid to gas. For example, using Equation 4.6, the energy needed to bring stainless steel from 295 K to 87 K is 3884.12 J/mole. The mass of the stainless steel tee vessel is 2.6 Kg or 46.5 moles, and therefore the total energy that needs to be removed is 180.61 KJ. Argon latent heat of vaporisation is 224.9 KJ, and by dividing the total energy needed to be removed from the stainless steel tee vessel by the latent heat of vaporisation of argon, 0.8 litres of LAr are required to cool down the tee vessel. Combining the fact that the stainless steel tee vessel is in thermal conduct with the cold head and LAr is going to be fed into the system at the same time, the cool-down of the tee is going to be also reduced.

Unfortunately, due to COVID19 restrictions the access to the laboratory was restricted and the flow of argon gas to the LArCell prototype was not possible. However, as during the cool-down test of the stainless-steel tee cell the liquefication temperature of argon was reached, the probability of successfully liquefying argon is high.

4.4 SiPM Characterisation

The SiPMs used in this thesis are the S13370-6050CN and are manufactured by Hamamatsu [34], see Figure 4.24. As in a SIPM, the overvoltage defines the dark current, and the gain of the SiPM, the overvoltage point of the Hamamatsu SiPM at room temperature, was tested. A picoamperometro is connected in series with the SiPM, and the current along the depletion region is measured. Figure 4.25 shows a diagram of the test setup made for the SiPM characterisation. Measurements between 50 and 58.5 Volts are taken with a step of 0.5 Volts, and using Equation 2.11, the dark current as a function of the bias voltage is plotted, see Figure 4.26. The overvoltage of the SiPM starts at 52 V, and the dark current increases exponentially with overvoltage (voltage above SiPM breakdown voltage).

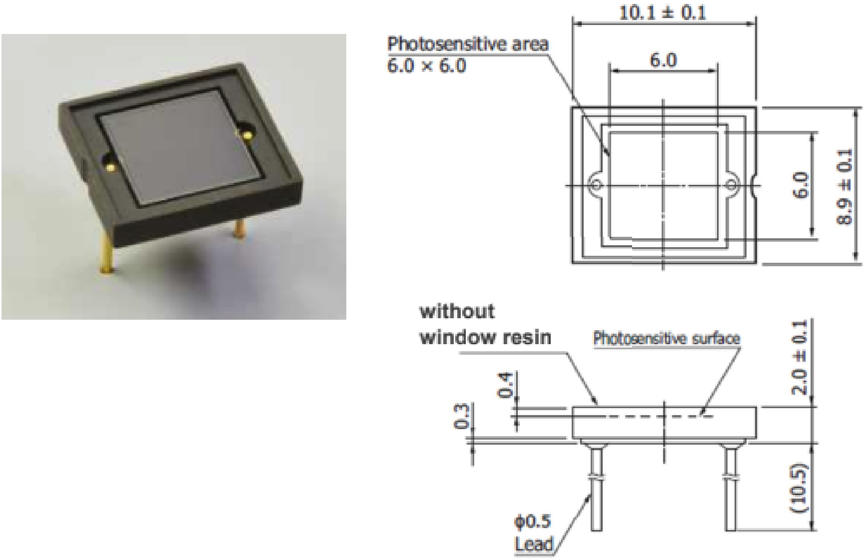

Figure 4.24: SiPM S13370-6050CN design drawings [34].

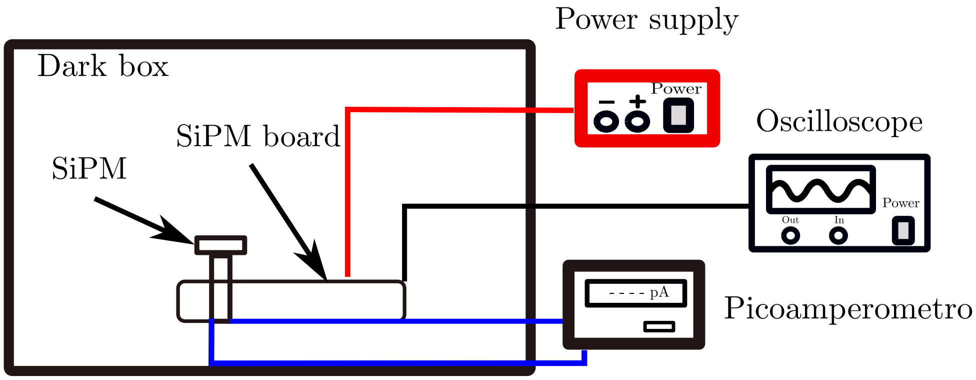

Figure 4.25: Diagram of the setup used for the SiPM characterisation.

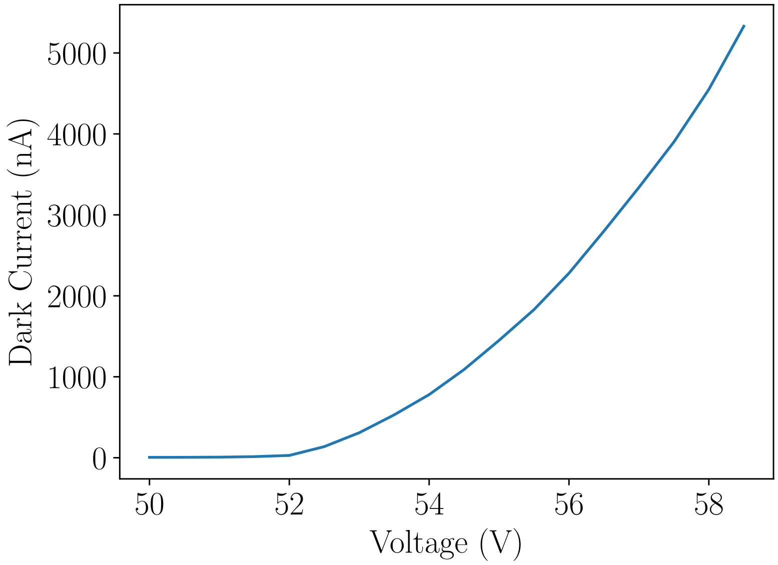

Figure 4.26: Plot showing the dark current as a function of bias voltage in a Hamamatsu MPPC S13370-6050CN. At 52V the overvoltage of the MPPC is started.

Moreover, the gain of the SiPM as a function of overvoltage at room temperature is shown in Figure 4.27. The junction capacitance C_j of the SiPM is 102 Femtofarad and is given by the manufacturer. Using the junction capacitance, the gain μ is equal to

$$\mu = \frac{(C_D + C_Q)(V_{\text{Bias}} - V_{\text{Br}})}{e} = \frac{(C_D + C_Q)\Delta V}{e} = \frac{C_J \ \Delta V}{e} \tag{4.10}$$

where C_D is the capacitance of the reversed biased diode, C_Q is the stray capacitance, V_{Bias} is the applied voltage, V_{Br} is the breakdown voltage, ΔV is the overvoltage, and e is the electron charge.

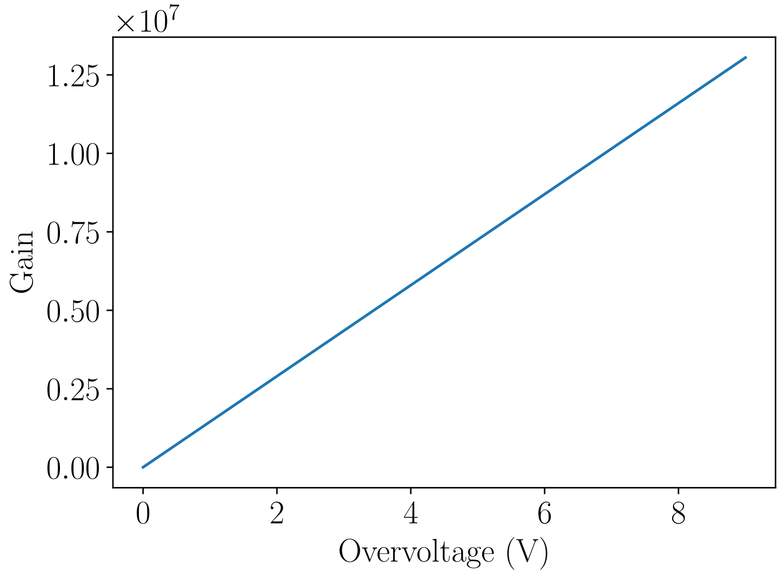

Figure 4.27: Plot of gain as a function of overvoltage in a Hamamatsu MPPC S13370-6050CN.

The dark current noise is expected to approach zero when the SiPM is submerged in LAr. The cryogenic temperature of LAr is expected to significantly reduce the thermal excitation of electrons close to the depletion region of the SIPM, and as a result, the dark current noise should be negligible. Using the tee shape cell prototype built in the laboratory, the reduction in the dark current and the evaluation of noise coming from after pulsed and cross talk was expected to be tested by submerging the SiPM in the LAr filled tee cell. A radioactive source was going to be placed outside of the tee cell, and the generated scintillation photons from LAr were going to be detected by the SiPM and analysed. However, due to the COVID restrictions, the test could not be made as access to the laboratory was restricted.

Chapter 5

LAr Ring PET Detector

5.1 GATE

GATE (GEANT4 Application for Emission Tomography) combines the well-validated GEANT4 [57] physics models, sophisticated geometry descriptions and 3D visualization [63]. GATE simulations consist of 4 layers, see Figure 5.1. The core layer encapsulates the GEANT4 kernel, where the geometry and physics processes are defined. On top of the core layer comes the application layer, where the user defines its user classes derived from the GEANT4 classes. Lastly, the user layer uses a dedicated scripting macro mechanism that does not require C++ programming. These macro commands execute the necessary GEANT4 functions, leading to the construction of the detector and performing the Monte Carlo simulations. One of the most innovative features of GATE is its ability to synchronize all time-dependent components in order to allow a coherent description of the acquisition process. This allows for modelling time-dependent processes such as count rates, random coincidences, or detector dead-time on an event-by-event basis.

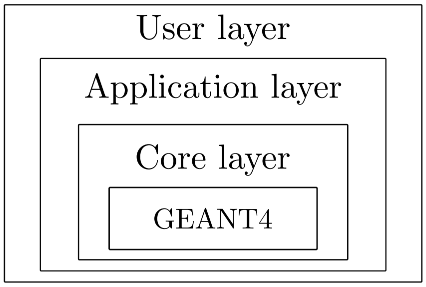

Figure 5.1: GATE layers structure.

The GATE simulation architecture for imaging applications has to include four mandatory classes. In the first class, the user must define the scanner geometry, such as the cell's geometry that will make up the detectors' ring around the patient, see Figure 5.2, and the optical properties of the materials used. Second, the physics processes must be defined, which for a PET scanner, are the electromagnetic interactions (photoelectric effect, Compton scattering, bremsstrahlung, ionisations and multi scattering). Third, the user must define the type of radioactive source, such as a volumetric/point source or a human/animal body phantom. Lastly, the user can start the acquisition, but first, it must define the source properties and specify the data output format.

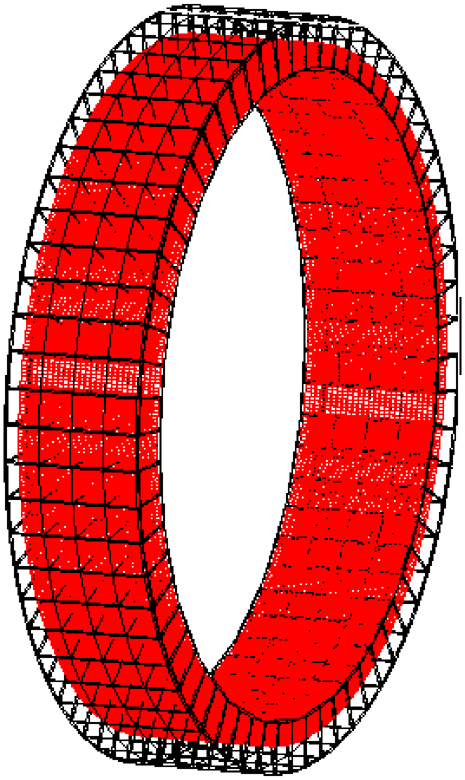

Figure 5.2: Visualisation of a typical multi-ring cylindrical PET scanner geometry in GATE that consists of LYSO scintillation crystals. The LYSO crystals are arranged in a cubic array, and using the *repeat* command of GATE; they form a single Ring detector. Then the single-ring detector is repeated to form a multi-ring visualisation of a typical multi-ring cylindrical PET scanner that consists of LYSO scintillation crystals.

5.2 Single Cell Properties

In Chapter 3, a test of Al+MgF_2 coating is made, which showed that coating the stainless-steel cell with Al+MgF_2 increases the detection efficiency of the LAr cell, but it is not sufficient to provide a good energy resolution. The reason is twofold, one as the reflectivity of Al+MgF_2 at the LAr scintillation photons wavelength is not 100%, and as a result, scintillation photons are absorbed into the stainless-steel walls (which have poor VUV wavelength reflectivity). Second, as the length of the cylinder has to be long so that the interaction probability of the 511 keV photons with LAr is increased, it results in a high number of LAr scintillation photons to be reabsorbed by LAr. The way to improve the energy resolution is to coat the LAr cell with a material with 100% reflectivity and reduce the radius of the LAr cylinder so that the LAr scintillation photons will travel a shorter path within LAr prior to their detection by the SiPMs. The SiPMs size determines the smallest radius possible, and in this Section, a single cell with a reflectivity of 100% and a radius of 5 mm is simulated. Its detection efficiency is based on the scintillation photons threshold, and energy resolution is tested. Its worth noting that the expected spatial resolution, see Equation 1.20 of the single ring PET detector is mainly determined by the diameter of the cylindrical cell. Therefore, reducing the cylinder's radius is expected to increase both the energy and spatial resolution.

Before calculating the detection efficiency, energy, and spatial resolution of the LAr cell used to build the single ring LAr PET detector, a test of the GATE simulation is made. GATE is based on GEANT4, but to ensure that physics, optical and material properties are working the same in Chapter 3, a test simulation is performed first. A stainless-steel cylinder with a radius of 25 mm and a length of 280 mm is coated with Al+MgF_2 in GATE, see Figure 5.3, and its detection efficiency is compared with the results acquired from the GEANT4 simulation performed in Chapter 3. Thirty SiPMS are placed on both sides of the cylinder, and 100K 511 keV photons are emitted towards the cylinder.

Figure 5.4 shows the detection efficiency of the cylindrical cell simulated in GEANT4 and GATE as a function of the scintillation photons threshold. The mean detection efficiency deviation $\overline{\epsilon}_{\mathrm{dev}}$ between the two simulations is 0.69%, see Equation 5.1, which is acceptable.

$$\overline{\epsilon}_{\mathrm{dev}} = \frac{\sum_{n}^{i=1} \left| \frac{\epsilon_i \mathrm{GEANT4} - \epsilon_i \mathrm{GATE}}{\epsilon_i \mathrm{GEANT4}} \right|}{n} \times 100 \tag{5.1}$$

where $\epsilon_{\mathrm{GEANT4}}$ is the detection efficiency calculated from the GEANT4 simulation, ϵ_{GATE} the detection efficiency calculated in the GATE simulation and n the scintillation photons threshold.

The radius and the length of the cylinder which the detection efficiency and energy resolution are going to be calculated are 5 mm and 280 mm, respectively. The reflectivity of the coating material is set to 100%, and one SiPM is coupled in each side of the cylinder with dimensions of 6 x 6 mm, see Figure 5.5. To calculate the detection efficiency and the energy resolution of the LAr cell, 200K

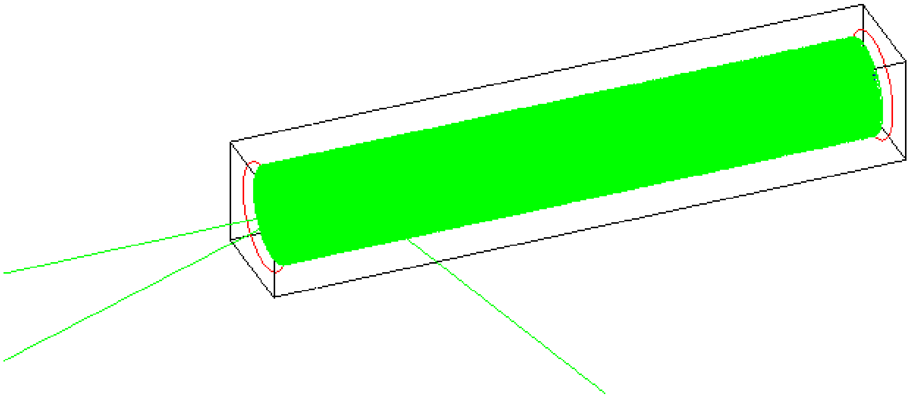

Figure 5.3: Visualisation of a single-cell cylindrical cell simulation in GATE enclosed in a vacuum box. The green lines within the cylindrical cell illustrate the scintillation photons trajectories. The red wireframe on the sides shows the stainless-steel cell.

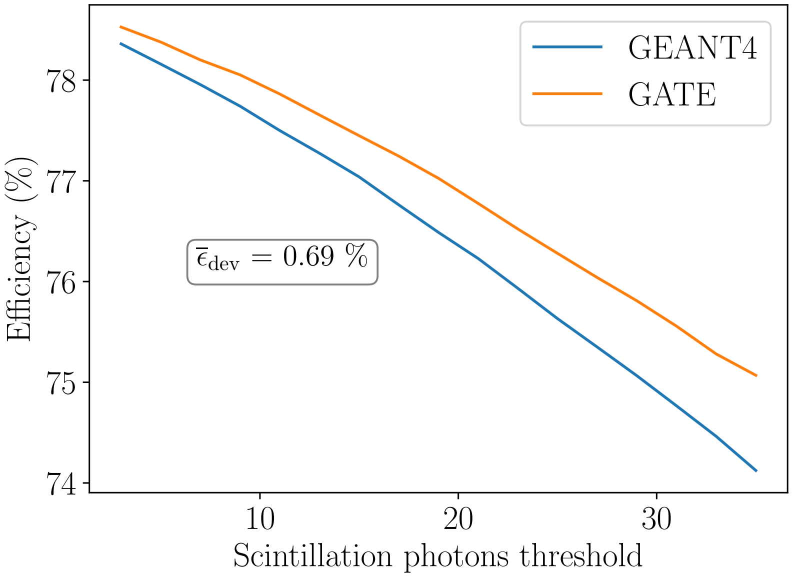

Figure 5.4: Comparison between the detection efficiency of the cylindrical cell simulated in GEANT4 and GATE as a function of the scintillation photons threshold.

511 keV photons are emitted towards the cell. Figure 5.6 shows the detection efficiency as a function of the scintillation photons threshold. As expected, the detection efficiency is dropped linearly as the scintillation photons threshold increases.

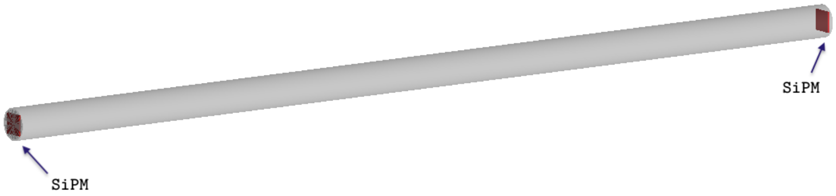

Figure 5.5: Visualisation of cylinder used to build the single ring LAr PET detector. Its radius and length are 5 mm and 280 mm, respectively.

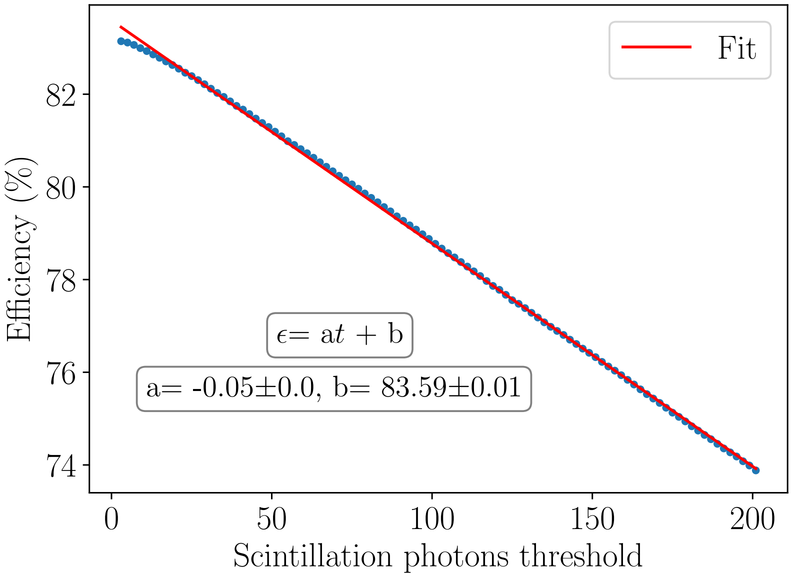

Figure 5.6: Detection efficiency as a function of the scintillation photons threshold. The detection efficiency is reduced linearly with the increase of the scintillation photons threshold.

As already stated, increasing the reflectivity of the coating material to 100% and reducing the size of the cylinder to the smallest size possible will result in a good energy resolution. Figure 5.7 shows a histogram of the detected scintillation photons by the SiPMs split into two categories. The first category (blue colour histogram) shows the scintillation photons detected by the SiPMs when the 511 keV photons deposited all their energy to LAr. The second category (orange histogram) shows events in which the emitted 511 keV photons did not deposit all their energy to LAr. There is a clear separation between the two histograms as they do not overlap, and therefore, a very good energy resolution is expected. Figure 5.8 shows the fit of the blue coloured histogram (full energy deposition) so that the energy resolution can be calculated. Using Equation 3.5, the relative energy resolution calculated is 0.87%.

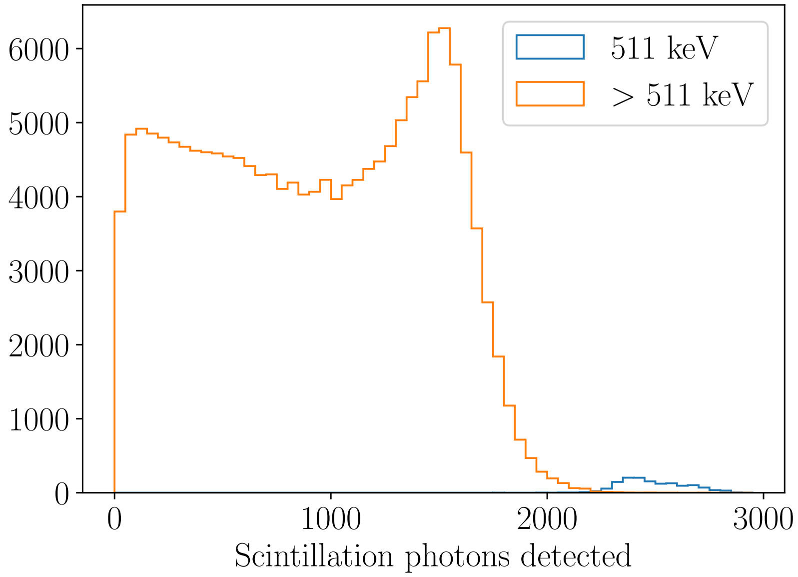

Figure 5.7: Histogram of the detected scintillation photons by the SiPMs. The blue colour histogram shows the scintillation photons detected by the SiPMs when the 511 keV photons deposited all their energy to LAr. The orange colour histogram shows events in which the emitted 511 keV photons did not deposit all their energy to LAr.

Lastly, the spatial resolution of the single ring LAr PET detector can be estimated using Equation 1.20. For simplicity reasons in the GATE simulation, back-to-back 511 keV photons are used as sources (tumours) and, therefore, image degradation due to positron range, noncollinearity, electronics decoding error, and radial elongation (sources placed near the centre) can be eliminated from Equation 1.20. The simplified version of Equation 1.20 becomes equal to

$$\Gamma = \frac{ad}{2} = \frac{1.25 \times 10}{2} = 6.25 \text{ mm} \tag{5.2}$$

where a is a multiplicative factor that accounts for the resolution degradation that occurs during the backprojection reconstruction and is equal to 1.25, and d is the diameter of the cylindrical cell and is equal to 10 mm. As a result, the spatial resolution of the detector is expected to be greater or equal to 6.25 mm. Figure 5.9 illustrates the impact of the image degradation (sampling error) due to the backprojection image reconstruction in a PET detector with 24 evenly spaced crystals (dark spots at the perimeter of the ring). The pixels at the exact centre are very well sampled (many LORs

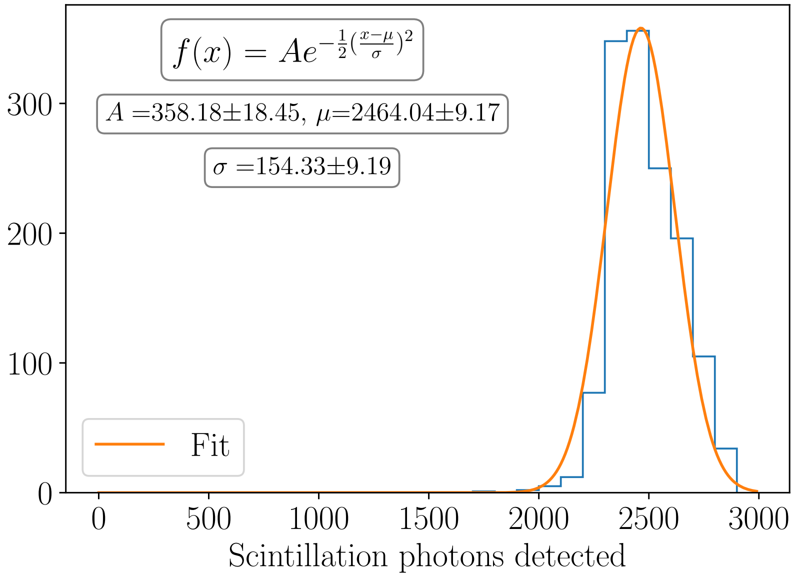

Figure 5.8: Fit of the histogram of the detected scintillation photons by the SiPMs when the 511 keV photons deposited all their energy to the LAr cell.

going through it), compared to nearby pixels, which are poorly sampled (only a few LORs go through them).

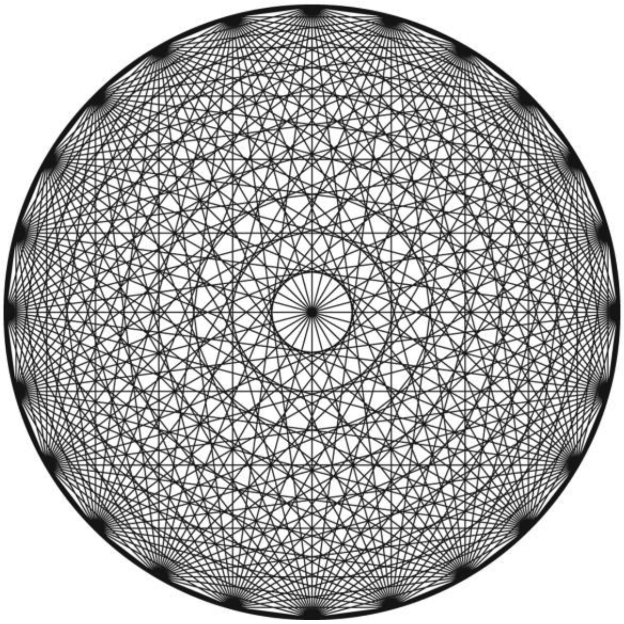

Figure 5.9: Illustration of the sampling error of PET detector with 24 evenly spaced crystals (dark spots at the perimeter of the ring). The Pixel at the exact centre is very well sampled (many LORs going through it) compared to nearby pixels which poorly sampled (only a few LORs go through them) [66].

5.3 Single Ring LAr PET Detector

Apart from good detection efficiency spatial and energy resolution, a PET detector must have a small coincidence window determined by the scintillation medium decay time and electronics. Especially, if PMTs or SiPMs are placed on both sides of the scintillation medium for TOF calculations. Clinical PET detectors have a coincidence time window of 6 - 10 ns. The fastest scintillation crystal (LYSO) has a decay time of 36 ns, which is six times larger than that of the fast decay of LAr (6 ns). Therefore using an accepted coincidence time window of 6 ns in the single ring LAr PET detector simulation is a safe assumption, although the electronics processing time is not known yet.

To build a PET detector in GATE in which information regarding particle interactions and properties are stored, one must define a *system* [64]. A *System* is a key concept of GATE, which provides a template of predefined scanner geometries. The most common scintillation materials used in PET scanners are crystals whose shape is a box, see Figure 5.2. As a result, all PET scanner *systems* developed in GATE requires that the scintillation material shape is a box, except the *genericscannersystem*, which does not have a fixed geometry requirement for the scintillation medium. As the liquid argon is stored in a cylindrical stainless-steel cell, the use of the *genericscannersystem* in GATE is mandatory. The disadvantage of this *system* is that the user must write its own image reconstruction algorithm as the GATE third party image reconstruction algorithms do not support the *genericscannersystem*. As a result, to evaluate the feasibility of a LAR PET detector, a Python script that performs a ray-driven backprojection is written. The process behind the ray-backprojection is explained in Section 1.7.1.

To be able to start a GATE imaging application, own must:

1. Define the *system* template that will be used, which is the *generic* scanner for this test.
2. Define the sensitive detector volume in which particle information is stored. During a GATE simulation, a file called $gate - Hits$ is automatically created, containing information regarding the detected scintillation photons by the sensitive detectors, such as energy deposition, detection time and position.
3. Choose a digitiser module.

As the data stored in a sensitive detector does not correspond to the data acquired by a real detector, a digitiser module's role is to build the physical observables from the $gate - Hit$ file information, which includes energy, position, and detection time of an annihilation event. A digitiser module called optical ladder is used for this project, which adds the energy deposited from all the scintillation photons created from each annihilation event within the cylindrical cells and stores the coordinates and the detection time of the fasted scintillation photon that reached the SiPMs. This information is automatically stored in a file called $gate - Singles$ by the GATE software. Lastly, GATE offers the creation of a third file called $gate - Coincidences$ which, based on user time and energy accepted window, chooses which events are considered true coincidence and discards events that are scattered or multiple, see Section 1.5.1 for a detailed explanation of these events. True coincident events occur when two photons resulting from the same annihilation point are detected within a preset time and energy window. On the other hand, scattered events that have undergone Compton scattering are expected to be detected with an energy less than 511 keV and a longer detection time (as they travel a longer distance than a non-scattered annihilation photon). Multiple coincidence events occur when multiple detector pairs have detected annihilation events within the same time window. In this case, the event's position becomes ambiguous, and therefore these events are discarded. Figure 5.10 shows a visualisation of a true coincidence event in GATE. Its worth noting that in GATE, to exclude coincidence coming from the same particle that is scattered within the cells, a coincidence event becomes valid only if the difference between the cells volume IDs is greater or equal to two. Also, the ring repeater function that repeats the LAr cell in a ring format around the centre axis, demands that the geometry of the cell is a box shape, and thus, the cylindrical cells are enclosed in a vacuum box which will not affect the result in any way. The macro file of the single ring PET detector can be found in the Git repository [69].

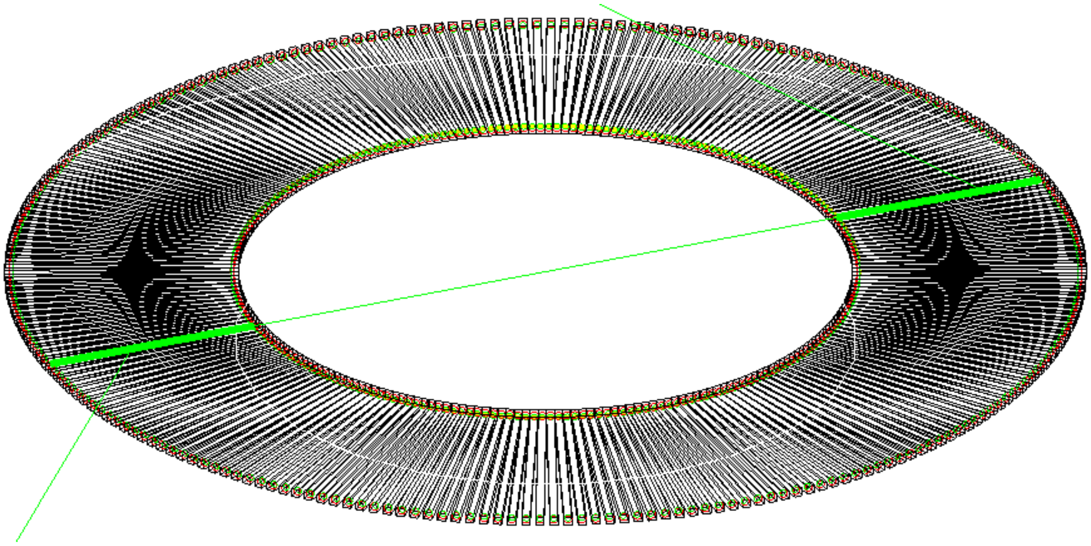

Figure 5.10: Visualisation of true coincidence event in a single ring LAr PET detector. Cylindrical cells have a radius of 5 mm and a length of 28 cm, and they are coupled with a single 6 × 6 mm SiPM on each cylinder side.

5.4 LAr PET Image Reconstruction

As already stated in Section 1.7, there are a lot of image reconstruction algorithms in the field of PET medical imaging. The two main approaches for imaging reconstruction are the analytical (backprojections) and the iterative algorithms, with iterative algorithms, be the chosen method. Analytical image reconstructions are mostly used in early-stage research PET detectors. The best and the most accurate method is the Time of Flight (TOF) method, which is briefly explained in Section 1.7.3, but due to limitations, has not achieved its maximum potential yet. Major PET manufacturers such as Siemens and Philips are continually investigating new ways to improve the image quality using the TOF-PET. However, as the TOF image resolution depends on crystal length (depth of interaction), electronic front end, digitiser timing, detector architecture (panel or block), crystal assembly, crystal surface and reflective coating material, it needs a constant search for optimisation and development. Also, the scientists who are focused on the improvement of PET image reconstruction have proposed the use of combined image modalities such as PET-CT (Computed Tomography) and PET-MRI (Magnetic Resonance Imaging) [65]. CT and MRI can solve the poor spatial resolution of PET scans, and therefore during patient imaging, both the anatomical and functional information (with excellent soft-tissue contrast) can be recorded. Most hospitals use the PET-CT combination but now are shifting to PET-MRI as this will reduce the patient exposure to ionising radiation and therefore allow multiple scans if needed without concerns about additional radiation exposure. Conventional PET scanners have spatial resolution limitations due to positrons range, noncolinearity and DOI, see Section 1.1.2 of ≈ 6-9 mm [66]. PET-CT and PET-MRI overcome these limitations, and the spatial resolutions range from 4.7 to 5.3 mm [65].

In this Section, the spatial resolution of the single ring LAr PET detector is evaluated using three point sources placed inside a human body phantom, see Figure 5.11. The radius of the single ring LAr PET detector is 40 cm, and a total of 262 cylindrical cells are needed to complete a full ring. The length and the radius of the human body cylindrical phantom are 30 and 7 cm, respectively. These dimensions reflect a small to mid-size human, and Figure 5.12 shows the interaction probability of the 511 keV photons with the human body phantom ($\rho = 1$ g/cm ^{3}, $\mu_{511 \text{ keV}} = 0.096$ cm $^{-1}$). As spatial resolution refers to the ability of an imaging detector to differentiate adjacent structures as being distinct from one another, this test can give a conclusive result on the spatial resolution of the single ring PET detector. As already stated, the images are reconstructed using ray-driven backprojection.

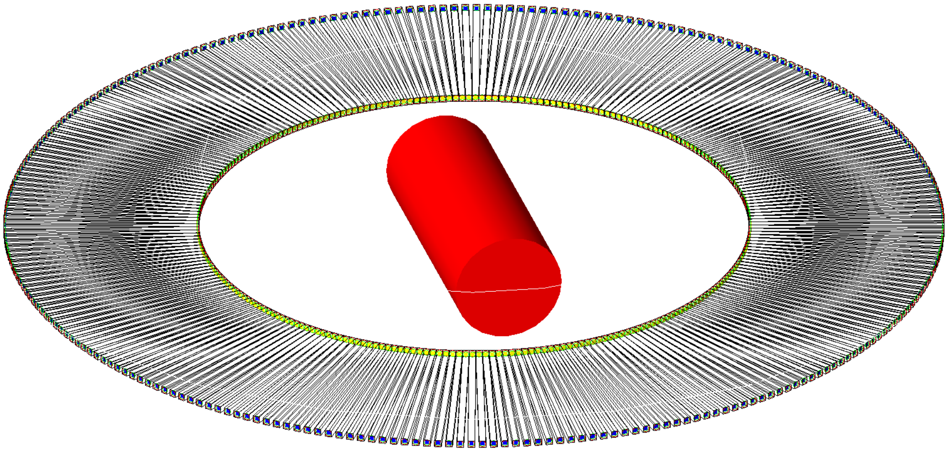

Figure 5.11: Visualisation of the single ring LAr PET detector (262 cylindrical cells). The red cylinder in the middle is the human body phantom with a radius of 7 cm and a length of 30 cm.

5.4.1 Ray-driven Backprojection

In ray-driven backprojection, lines are drawn between the detector pairs in which true coincidence events are registered, see Figure 1.10. Using the x and y coordinates of the fastest scintillation photons of the true coincidence events that reached the SiPMs, a line is drawn. Based on the grid size, the

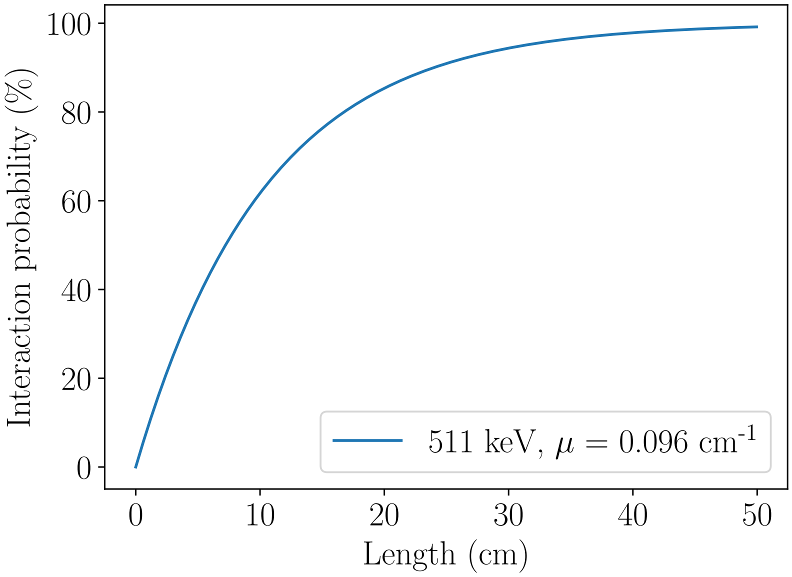

Figure 5.12: Interaction probability of 511 keV photons with a human body phantom.

points at which the line intersects the grid are calculated. Then the length of the line which connects the two adjacent points is calculated. Lastly, the sum of the length of each line that fills each pixel is multiplied by the number of the lines that intersect each pixel, see Equation 1.22. To test that the Python script correctly performs the ray-driven backprojection image reconstruction, a line with a slope of -8 and an intersection point of 0 mm is used, see Figure 5.13(a). The pixel grid size used for the test is 8×8, and Figure 5.13(b) shows the pixels filing of the reconstructed image. Each pixel represents a 1×1 mm box, therefore by default, the image resolution is caped at $\pm$ 1 mm and therefore objects smaller than 1 mm can not be accurately imaged. A post-processing filter can be applied to improve the image quality contrast when the image is reconstructed, such as high pass filters.

Before testing the spatial resolution of the single ring PET detector, a simulation of only one point source located at the middle of the detector is made, and the ray driven backprojection is performed. Five million back-to-back 511 keV photons are generated isotropically, and the image is reconstructed on a 20×20 image grid. Figure 5.14 shows the image reconstruction of a point source placed at the centre of the LAr PET detector. As expected, due to the limitation of the pixel grid size, the image resolution is ± 1. To ensure that the image is reconstructed correctly, the histograms of the x and y coordinates of the points in which the lines of response have intersected the grid are plotted. Figure 5.15 shows the histogram of the x-coordinate of the intersection points with the grid; each bin is equal to 1 mm. As expected, the bins of $\pm$ 1 mm, close to the point source, have the most events. Figure

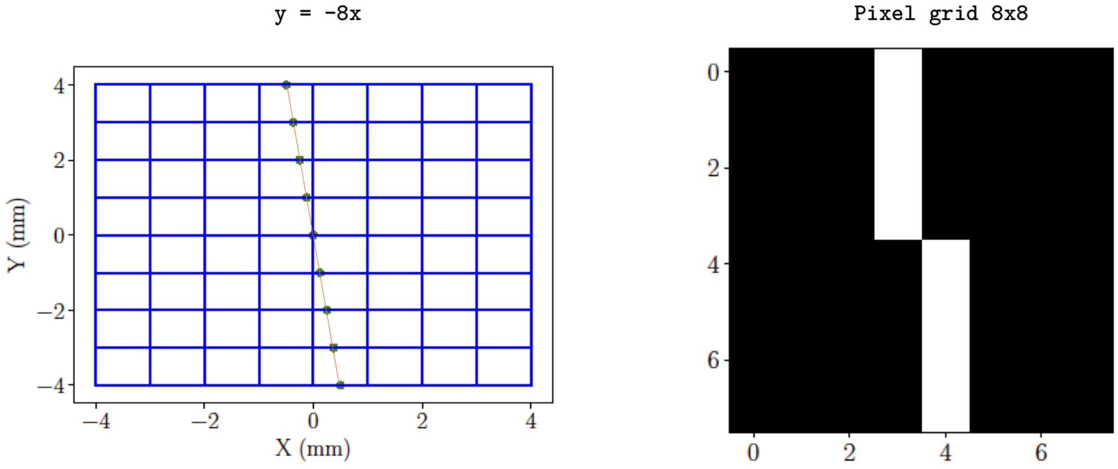

(a)

(b)

Figure 5.13: Ray-driven backprojection script test. Plot (a) shows the intersection points of a line with a pixel grid of 8×8, and image (b) shows the pixel filling based on the length of the line within a pixel.

5.16 shows the histogram of the y-coordinate of the intersection points with the grid. Also, bins of ± 1 mm have the most events as they are closer to the point source. This good image resolution, is expected as the point source is located at the centre of the PET detector where the centre pixels are well sampled (many LORs passing through them).

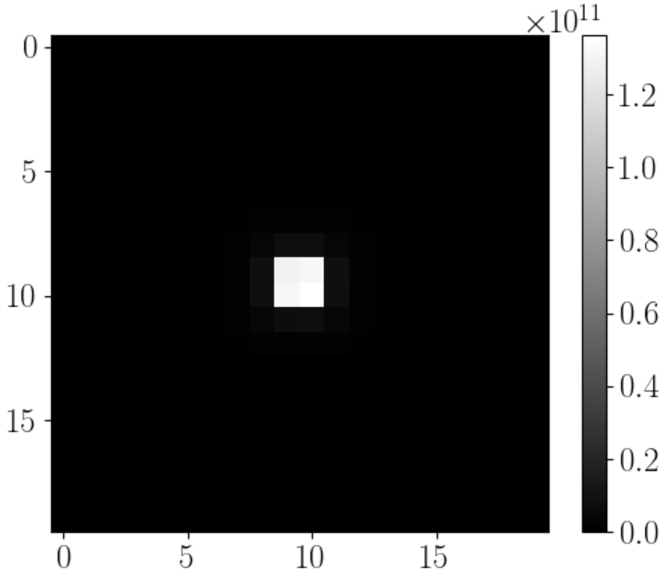

Figure 5.14: Ray-driven backprojection of a point source placed at the centre of the LAr PET detector.

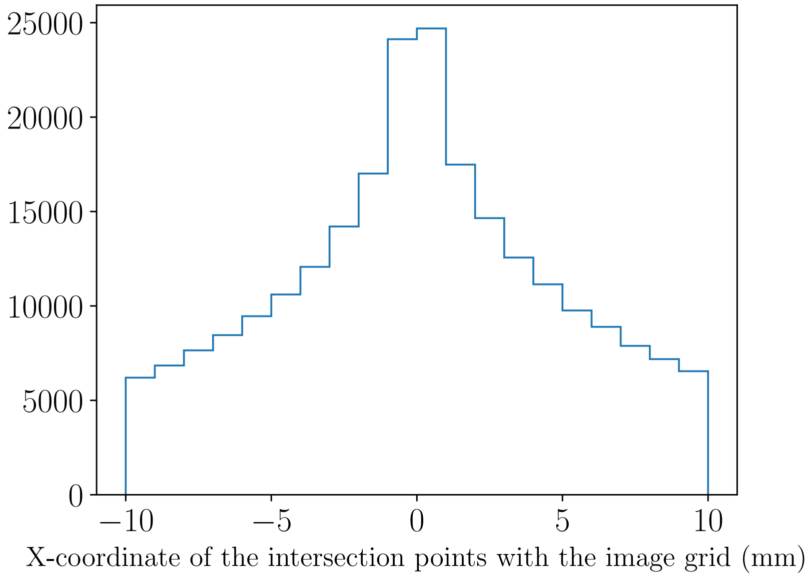

Figure 5.15: Histogram of the X-coordinate of the LORs intersection points with the 20×20 pixels image grid.

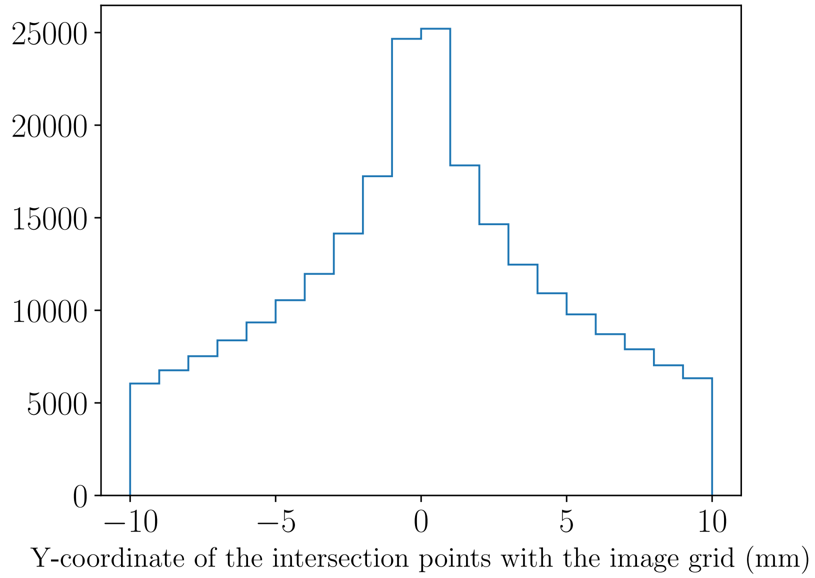

Figure 5.16: Histogram of the Y-coordinate of the LORs intersection points with the 20 × 20 pixels image grid.

Based on the dimension of the cylindrical cell, the spatial resolution of the detector must be greater or equal to 6.25 mm, see Equation 5.2. Any sources located at a distance less than 6.25 mm can not be differentiated. As already stated, the ring detector's spatial resolution is evaluated using three point sources. The first point source is located at the centre of the detector (x, $y = 0$ mm), and the other two sources are placed $x = \pm\ 7$ mm and $y = 0$ mm. The sources are not placed exactly at 6.25 mm (except the DOI degradation) due to the limitation of the pixel grid size (±1), and therefore placing them at ± 7 mm is chosen. Although it is known that a source located at a distance less than the width of the detector can not be differentiated, a simulation is made to confirm that. A source was placed at the centre of the PET detector, and a second source was moved along the x-axis with a step of 1 mm. As expected, the reconstructed images show that sources placed at a distance less than the LAr cell width could not be differentiated.

For the spatial resolution test, 1.2 billion events are generated isotropically from all three sources. The energy resolution cut window of 30% is chosen as in most clinical PET detectors, and a coincidence time window of 6 ns. Figure 5.17 shows a comparison between the reconstructed images when no energy cut windows are used and when it is used. The image in which no energy cut windows is used is noisier than that of the 30% energy resolution cut (460 - 560 keV) as Compton scattered events within the patient are also accepted as coincidence events. It is worth noting that the noise is proportional to the size of the patients. Lastly, as already explained in Figure 5.9, the two sources that are not located at the centre of the LAr ring PET detector appear less bright than that of the centre as fewer LORs pass through them.

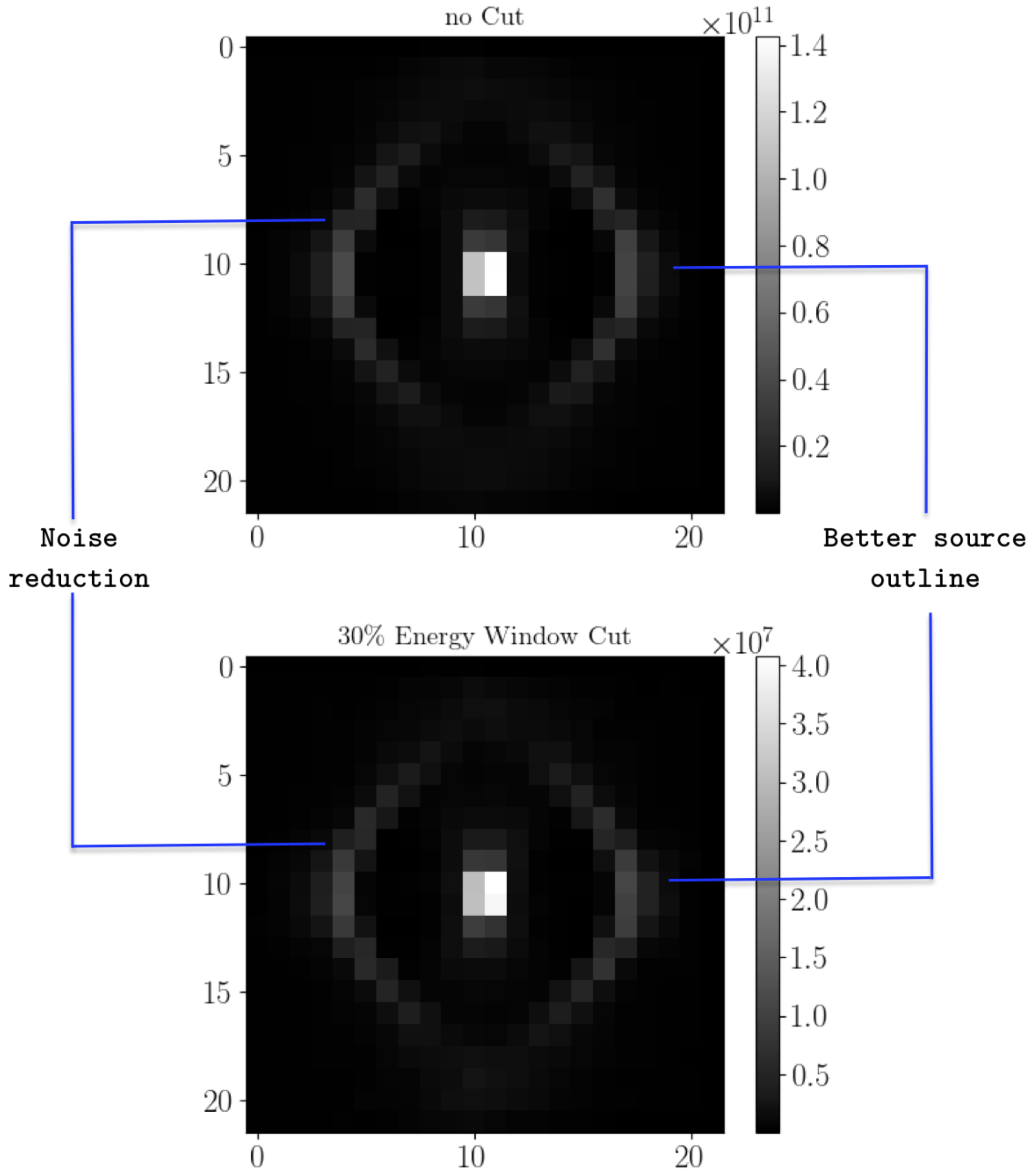

Figure 5.17: Comparison between the reconstructed images when an energy resolution window cut is applied and when it is not. The reconstructed image with the energy resolution window cut has reduced noise and better contrast by applying an energy resolution window cut.

The spatial resolution is measured by slicing a pixel row through the centre of the pixel grid and then checking if the point sources are distinguished. Figure 5.18 shows the slice through the pixel grid which a histogram of the x-coordinate of the interaction points with the image grid is used to evaluate the spatial resolution. By fitting the histogram, each point source follows a Gaussian distribution and can be clearly distinguished. The peaks of the Gaussian distribution of the two sources that are offset from the centre are within the expected resolution limitation of the pixel grid ($\pm$ 1) and therefore, a spatial resolution of 7 mm is achieved by the single ring LAr PET detector.

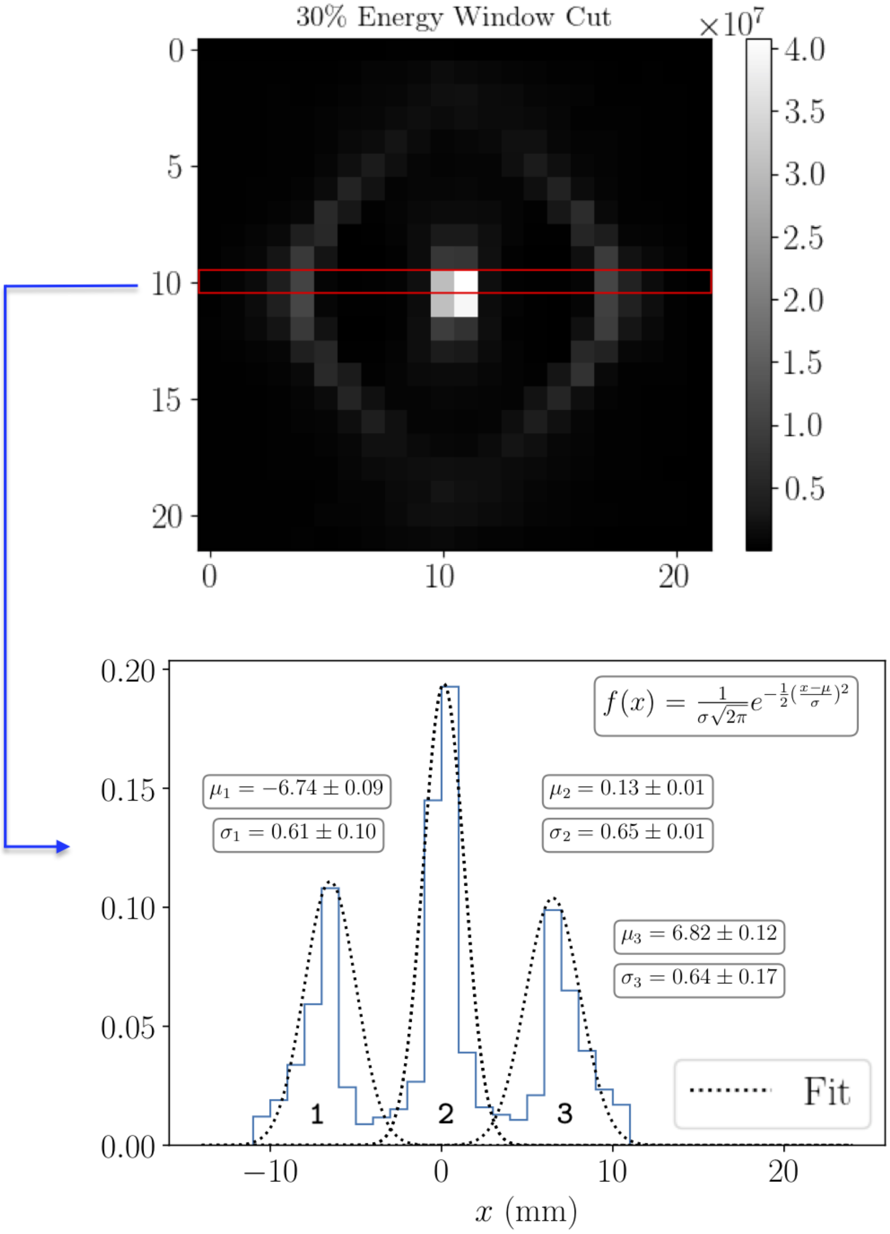

Figure 5.18: Using a slice through the pixel grid (red rectangle), a histogram of the x-coordinate of the interaction points of LORs with the image grid is used to measure the spatial resolution. The Gaussian fits of each source show that the point sources can clearly be distinguished.

As already stated, the TOF concept can greatly improve the image resolution of a PET detector. This can be proven using the fact that the point at which the 511 keV interacted with the LAr can be recorded in GATE. As a result, instead of performing the image reconstruction using the scintillation photons energy deposition position coordinates, it is reconstructed using the position coordinates of the point which the 511 keV photons interacted with LAr and the scintillation photons are emitted. Figure 5.19 shows a comparison between the TOF and non-TOF images. It is apparent that the TOF image has much less noise compared to the non-TOF image, and as a result, the image quality is better. As TOF provide significant improvement in the image quality, after the multi-ring LAr PET detector construction, a reconstructed image algorithm that uses the TOF is planned to be developed. GATE does not provide such an algorithm yet, and therefore is something that is needed. This introduces more complexity to the system which adjustments may have to be made to the ring cells. Furthermore, the spatial and energy resolution of the detector will be re-evaluated based on the sampling system image reconstruction algorithm. All these factors add a high complexity to a clinical PET detector which, with the new generation of detectors such as PET-CT and PET-MRI this becomes even more complicated.

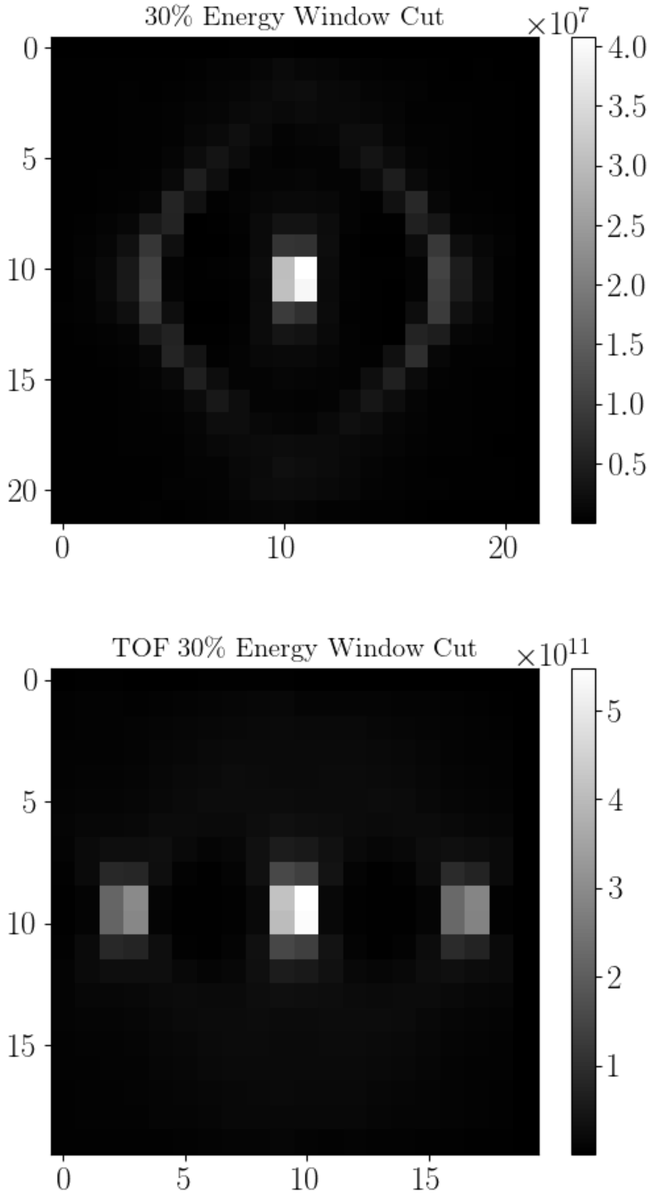

Figure 5.19: Comparison between a TOF and non-TOF image.

Chapter 6

Conclusion

In this thesis, using the GEANT4 simulations, a single ring LAr cell is optimised to give the best possible detection efficiency. From all the shapes tested, the cylindrical cell of 280 mm length and radius 25 mm coated with Al+MgF$_2$ and an array of 30 SiPM on each cylinder side gave the best detection efficiency (scintillation threshold greater than one). Detection efficiency depends on the accepted scintillation photons threshold, and it reduces linearly as the accepted scintillation photons threshold increases. Using the SiPMs array on both sides of the cylindrical LAr cell, the DOI is estimated utilising the TOF concept, and the spatial resolution is found to be 24 mm.

The energy resolution of the optimised cell is calculated, and the result was not adequate as the 511 keV full absorption peak could not be distinguished from the Compton edge. The reason is twofold, the reflectivity of Al+MgF$_2$ is only $\approx$84% at the LAr scintillation photons wavelength of 128 nm and, as a result, a number of scintillation photons is absorbed by the stainless-steel walls. Second, a high number of scintillation photons is reabsorbed by LAr as they have to travel a long path within the LAr prior to their detection by the SiPMs. Using the same radius and length cylinder (that fits in the prototype setup), the cell is coated with a material of reflectivity of 100%, and the full absorption peak of the 511 keV photons is distinguishable from the Compton edge. The measured relative energy resolution is 1.14%.

A test stand in which cells filled with LAr can be evaluated is built. A state of the art monitoring and data acquisition system is built from scratch using EPICS. The cryogenic system design of the prototype can successfully reach LAr cryogenic temperature, and therefore the detection efficiency and energy resolution of various shaped cells can be measured. Also, SiPMs manufactured from different suppliers can be tested using this prototype.

The single ring LAr PET simulation in GATE consist of 262 cylinders of 5 mm radius and 280 mm length. The SiPM size determines the cell's radius as one SiPM is placed on each side of the cylinder.

The single ring LAr PET detector achieved a relative energy resolution of 0.86%, detection efficiency of ≈ 84%, and a spatial resolution of 7±1 mm.

6.1 Future Work

Before constructing a second-generation LAr-PET detector, a brief outline of all the properties a PET detector must have will be defined. A prototype PET detector has a set of requirements that ideally must be met before it enters the field of clinical PET detectors. These requirements are:

1. High detection efficiency (>84%).
2. Good spatial resolution (6-10 mm).
3. Small coincidence window (<12 ns).
4. High energy resolution (<10%).
5. Able to measure the depth of interaction in a cell for TOF image reconstruction.
6. A scintillation light detector (e.g. SiPM) that can operate under strong magnetic fields, as MRI-PET detectors are beginning to have a vote of preference in the hospital environment due to the reduced patient dose.
7. Low manufacturing cost.

This thesis is focused on the detection efficiency of a LAr cell that will make up the cell PET rings placed around the patient. As already stated, PET imaging requires high detection efficiency as it directly impacts the amount of radiation a patient is exposed to obtain an accurate and informative image. A higher detection efficiency translates to a lower dose of radioactive tracers required, which is crucial for patients undergoing repeated scans or those with higher sensitivity to radiation, such young children. Optimisation of detection efficiency in PET imaging is essential to ensure that patients receive the lowest possible radiation dose while still obtaining high-quality diagnostic images. This improves patient safety and comfort and reduces the risk of long-term side effects and complications associated with radiation exposure. Ultimately, healthcare providers can provide high-quality care by optimising the detection efficiency in PET imaging, thus benefiting the patient's overall health outcomes. The cell's geometry and reflective coating are the most important parameters in detection efficiency optimisation.

The reflective material tested in the simulations is Al+MgF_2 which at 128 nm (LAr scintillation light) has 84% reflectivity. Finding a material that has a reflectivity greater than 84% and as close to

100% as possible improves the detection efficiency and energy resolution substantially (see Section 3.4). Also, as LAr must be contained in a vessel, a percentage of the annihilation photons will inevitably interact with that outer material and reduce detection efficiency. For Example, this thesis uses stainless steel as the LAr container. The CF50 fitting of the cylindrical cell has a length of 4 mm, and as a result, the interaction probability of the 511 keV annihilation photons with it is 23.7%. Finding a suitable window material that balances low interaction probability with high vacuum stability is crucial to increasing the detection efficiency of the annihilation photons.

The cylindrical geometry had the best results for building a PET detector with this cell geometry. Although more geometries than the ones tested in this thesis can be tested, the cylindrical geometry seems a very good candidate as, like a torch, it guides the scintillation photons towards the SiPMs placed on the sides of the cell. However, as the SiPMs have a rectangular shape and the cells are cylindrical, a smaller size SiPMs than the 6×6 mm, we will increase the detection efficiency even further as the dead space will be reduced (see Figure 3.23).

In order to validate the effectiveness of the proposed LAr PET detector design, the first step is to make two cylindrical cells and position them in opposite directions. A movable radioactive source will then be placed between the two cells to simulate the positron emission process that occurs during a PET scan. This step aims to calculate the detection efficiency and energy resolution of the detector, which are crucial factors in producing a high-quality diagnostic image and always compare the results with the GEANT4 simulations. The image reconstruction techniques, such as Filtered back projection and Time of Flight, will also be used to visualise the annihilation photons start location and produce a three-dimensional image of the source. Lastly, the accepted scintillation photons threshold can be tested as well.

As shown in Chapter 5, the detection efficiency depends on the scintillation photons threshold. As the SiPMs are submerged to LAr and, according to the manufacturer, can operate without a problem at 87 K, their dark count rate should be essentially negligible. However, noise from after-pulses and cross-talk should be present, and therefore, the accepted scintillation photons threshold needs to be decided based on the experimental results. The best scintillation photons threshold was going to be tested in this thesis, but due to the Covid-19 pandemic, that was not possible as access to the laboratory was restricted. As a result, an exact calculation of the LAr-PET detector sensitivity was not possible. However, using Figure 3.31, which shows the detection efficiency as a function of the scintillation photons threshold, own can estimate the detection efficiency and compare it with the experimental results.

Once the two-cell configuration has been optimised and validated, the next step is to build a full detector for small animals. This is something that can be built in the laboratory as the internal diameter of a standard PET scanner for small animals is 150 mn. This will allow us to evaluate the engineering complexity of a LAr PET detector which needs to operate in cryogenic temperatures and high vacuum. Also, how easily the cells can be filled with LAr and how this argon will be released outside of the laboratory in case of a failure. Next, how will it be best to fill the cylindrical cells with argon without affecting the detection efficiency or energy resolution of the LAr PET detector? Also we will be able to test the electronics of the PET detector and optimise this part as well. Argon as a material is very cheap as it is abundant in the atmosphere, but as argon liquefies in the cryogenic region, engineering difficulties and the cost is something that is currently unknown. LAr light yield depends on its level of purity, and therefore, a high level of vacuum system is required. Commercial PET detectors use scintillation crystals, which are as high as 60 times more expensive than LAr per cc, but it remains unknown if that price difference is covered by the extra equipment needed (getter, cryogenic and vacuum system) for a LAr PET detector. Lastly, the SiPMs tested in this project can operate in strong magnetic fields, and their price is £300 per SiPM, which is much cheaper than PMTs (> £1500), which also need special equipment for shielding against strong magnetic fields. To conclude, constructing a PET detector for small animals will be extremely helpful for tackling engineering problems in constructing a PET detector for Humans as its construction cost is definitely smaller than a full-size Human PET detector with an inner diameter of 800 mm. For Example, we can see that the length of the cylinders (28 cm) is too big, and the escaped annihilation photons from adjacent cells can degrade our Image quality. Then we can try doping LAr with a material such as liquid Xenon, which has higher stopping power and, as a result, reduces the length of the cells and re-evaluate our setup.

Furthermore, constructing a PET detector for small animals can allow as a measure of detection purity. Detection purity, in general, measures the detector's efficiency in correctly identifying the desired particle type while rejecting other particles that may produce similar signals in the detector. In PET imaging detection, purity refers to the effectiveness of the PET scanner in identifying true coincidences between two gamma rays emitted from positron annihilation events while rejecting random coincidences and other types of noise. Detection purity is essential for PET imaging because random coincidences and other sources of noise can degrade the image quality and reduce the accuracy of the quantification of the tracer concentration. A high detection purity ensures that the PET scanner detects only the true coincidences and rejects the false ones, leading to more accurate and reliable PET images. The detection purity is typically expressed as a ratio of true coincidences to the total number of detected events.

Reaching a point where one can build a commercial PET detector takes time, as outlined above, as many parameters need to be tested individually and combined, such as high detection efficiency, high purity, good spatial resolution, small coincidence window, ability to use the TOF concept, engineering feasibility and cost. Moving from the single-cell prototype to the two-cells prototype and then to the small size PET (diameter 180mm) is the best approach to tackle each step stated and finalise a prototype for a human size PET scanner.

References

[1] INTERNATIONAL ATOMIC ENERGY AGENCY, “Physical principles and technology of clinical PET imaging”, IAEA, Vienna (2009).

[2] S.R. Cherry, J.A. Sorenson and M.E. Phelps, “Physics in Nuclear Medicine”, Third Edition, page 310-314 (2003).

[3] Simon R. CherryMagnus Dahlbom, “PET: Physics, Instrumentation, and Scanners”, page 9-12, In: Phelps M.E. (eds) PET. Springer, New York, NY (2006).

[4] Tarantola G, Zito F, Gerundini P, “PET instrumentation and reconstruction algorithms in whole-body applications”, J Nucl Med 2003;44:756.

[5] Evans R.D, “The Atomic Nucleus”, New York, page 711-712, McGraw-Hill, (1955).

[6] INTERNATIONAL ATOMIC ENERGY AGENCY, “Radiation Oncology Physics”,page 38-39 , IAEA, Vienna (2005).

[7] Klein O, Nishina, Y, “On the scattering of radiation by free electrons according to Dirac’s new relativistic quantum dynamics”, Z. Physik 52, 853-868 (1929).

[8] Simon R. CherryMagnus Dahlbom, “PET: Physics, Instrumentation, and Scanners”, page 15, In: Phelps M.E. (eds) PET. Springer, New York, NY (2006).

[9] G. Tarantola et al., “PET instrumentation and reconstruction algorithms in whole-body applications”, Journal of Nuclear Medicine 45 (2003) 756-769.

[10] Brambilla M et al, “ Performance characteristics obtained for a new 3-dimensional lutetium oxyorthosilicate-based whole-body PET/CT scanner with the National Electrical Manufacturers Association NU 2-2001 standard”, J Nucl Med. (2005) Dec;46(12):2083-91.

[11] Derenzo, S. E., Moses, et al, “ Quantification of brain function: Tracer kinetics and image analysis in brain PET” Elsevier. Chap. Critical instrumentation issues for ¡2 mm resolution, high sensitivity brain PET., pages 25–40. 2.4.1, (1993).

[12] G. Saha, " Basics of PET Imaging, Physics, Chemistry and Regulations", page 84 , Springer, (2010).

[13] Simon R. CherryMagnus Dahlbom, "PET: Physics, Instrumentation, and Scanners", page 70-72, In: Phelps M.E. (eds) PET. Springer, New York, NY (2006).

[14] A.J. Reader et al. "One-pass list-mode EM algorithm for high-resolution 3-D PET image reconstruction Into large arrays", IEEE Trans. Nucl. Sci. 49 (2002) 693-698.

[15] M. Berger, J. Hubbell, S. Seltzer et al., National Institute of Standards and Technology, PML, Radiation and Biomolecular Physics Division.

[16] E.Lemmon, M.McLinden, and D.Friend NIST Chemistry WebBook, NIST Standard Reference Database Number 69, ch. Thermophysical Properties of Fluid Systems (National Institute of Standards and Technology, Gaithersburg, MD, 2009), chap. Thermophysical Properties of Fluid Systems.

[17] A. Gedanken, J. Jortner, B. Raz et al.,"Electronic Energy Transfer Phenomena in Rare Gases", The Journal of Chemical Physics 57 (1972) 3456–3469. doi:10.1063/1.1678779.

[18] Marlo Martin, "Exciton Self-Trapping in Rare-Gas Crystals", J. Chem. Phys. 54, 3289 (1971).

[19] A. Hitachi, T. Takahashi, N. Funayama et al.,"Effect of ionization density on the time dependence of luminescence from liquid argon and xenon", Phys. Rev. B 27 (1983) 5279–5285. doi:10.1103/PhysRevB.27.5279.

[20] Peter V. E. McClintock, "Fundamentals of fluorescence microscopy: exploring life with light", by Partha Pratim Mondal and Alberto Diaspro, Contemporary Physics, 58:2, 181-182, DOI: 10.1080/00107514.2016.1262905.

[21] V. Boccone, on behalf of the ArDM collaboration The ArDM project: "A Liquid Argon TPC for Dark Matter Detection", Physik-Institut der Universit at Zurich, Winterthurerstrasse 190, CH-8057 Zurich, Switzerland.

[22] A.Hitachi and T.Doke, "Luminescence quenching in liquid argon under charged-particle impact: Relative scintillation yield at different linear energy transfers", Phys Rev B Condens Matter, (1992) Nov 1;46(18):11463-11470.

[23] Agnes, P. et al."Measurement of the Liquid Argon Energy Response to Nuclear and Electronic Recoils", Physical Review D 97.11 (2018).

[24] Werner F. Schmidt and Eugen Illenberger, “Electronic Excitations in Liquefied Rare Gases”, page74-75, American Scientific Publishers, (2005).

[25] Advatech - Radiation Detection/Imaging and Photonics Properties of BGO LYSO and LSO https://www.advatech-uk.co.uk.

[26] E R Dobbs and G O Jones, “Theory and properties of solid argon”, Reports on Progress in Physics, 20(1):516, (1957).

[27] P.J. Linstrom and W.G. Mallard, “NIST Chemistry WebBook”, NIST Standard Reference Database. National Institute of Standards and Technology, 69 edition, (2016).

[28] S.M. Sze and Kwok K. Ng, “Physics of Semiconductor Devices”, page 7-16, JOHN WILEY & SONS, JNC., PUBLICATION, (2006).

[29] S.M. Sze, “Physics of Semiconductor Devices”, John Wiley & Sons, (1981).

[30] G. Parker, “Introductory Semiconductor Device Physics”, Taylor & Francis, (2004).

[31] P. Buzhan et al., “An advanced study of silicon photomultiplier”, ICFA Inst. Bulletin. 23, (2003).

[32] D. Renker, “New trends on photodetectors for Nuclear Instruments and Methods in Physics”, Research Section A, 571(1-2):1 – 6, (2007).

[33] A. Ghassemi, K. Sato, K. Kobayash, “MPPC Techincal note” , Hamamatsu , (2017).

[34] Hammatsu product flyer, “VUV-MPPC 4th generation”, (2017).

[35] M. Kapusta et al., “Breakthrough in quantum efficiency of bi-alkali photocathodes PMTs”, Nuclear Science Symposium Conference Record, 2007. NSS ’07. IEEE, 1, 26 2007-Nov. 3 (2007).

[36] H. Dautet et al.,“ Photon counting techniques with silicon avalanche photodiodes”, Appl. Opt., 32(21):3894–3900, (1993).

[37] Hamamatsu,“ Photomultiplier tubes: Basics and Applications”, pages 221- 231 ,3rd edition, (2007).

[38] R M Faradzhaev et al, J. Phys.: Conf. Ser. 675 042008, (2016).

[39] NIKOLAI V.TKACHENKO,“Optical Spectroscopy”, pages 61 - 87, Elsevier Science, (2006).

[40] Boc, Liquid Argon price https://www.boconline.co.uk.

[41] Philip Stanley, Janet Anderson, Marty Kraimer “Experimental Physics and Industrial Control System (EPICS)”, The University of California, The University of Chicago, (1995).

[42] Cryogenic Control Systems, INC,Model 24c cryogenic temperature controller , "User Guide".

[43] InstruTech, Hot Cathode Ionization Vacuum Gauge With Dual Convection IGM402 Module" User Manual", (2004).

[44] Omega, Omega PX 219 Pressure transducer, "User manual".

[45] https://bitbucket.org/Theomedphysics/pet_daq/src/.

[46] M W Hosking et al 1993 Supercond. Sci. Technol. **6** 549.

[47] C.A.E.N. "Technical information manual", V1720 digitizer, (2014).

[48] C.A.E.N. "Technical information manual", Mod n625 quad linear fan in / fan out, (2004).

[49] C.A.E.N. "Technical information manual", Mod n417 8 channel low threshold discriminators, (1996).

[50] https://bitbucket.org/Theomedphysics/pet_daq/src/master/instruments/CaenDigitiser/.

[51] E.D. Marquardt, J.P. Le, and Ray Radebaugh, "Cryogenic Material Properties Database", National Institute of Standards and Technology, CO 80303 , (2000).

[52] Cryomech, "PT810 Cryocooler system drawing".

[53] Cryomech, "Cryorefrigerator specification sheet".

[54] Cryomech, "PT810 Cryocooler capacity curve".

[55] Chawner, J.M.A., Jones, A.T., Noble, M.T. et al. "LEGO Block Structures as a Sub-Kelvin Thermal Insulator", Sci Rep 9, 19642 (2019).

[56] Cryogenic Control Systems NC , Silicon diode temperature sensor s900, "User Manual", (2013).

[57] GEANT4 Collaboration, "GEANT4 Simulation Tool kit Book For Application Developers", Release 10.4.

[58] https://bitbucket.org/theophysics/geant4cells/src.

[59] S.T. Boogert et al, "Pyg4ometry : A Tool To Create Geometries For Geant4, BDSIM, G4Beamline and Fluka For Particle Loss and Energy Deposit Studies", IPAC2019, Melbourne, Australia, (2019).

[60] Björn Karlsson and Carl G. Ribbing, "Optical constants and spectral selectivity of stainless steel and its oxides", Journal of Applied Physics 53, 6340 (1982).

[61] Roger A. Paquin, "Handbook of Optics", Vol. II, Part 4 ,Chapter 35, Properties of metals, McGRAW-HILL , INC, (1995).

[62] Action opics and coating, "Optics and Coatings (Al+$\mathrm{MgF_2}$) Acton-Optics-Brochure-revD5", pages 16-17.

[63] Jan S, Santin G, Strul D et al., "GATE: a simulation toolkit for PET and SPECT", Phys Med Biol. 2004;49(19):4543-4561. doi:10.1088/0031-9155/49/19/007, (2004).

[64] GATE - Geant4 Application for Tomographic Emission: "Users Guide & Installation Guide".

[65] S. Vandenberghe, E. Mikhaylova, E. D'Hoe, P. Mollet and J. S. Karp, "Recent developments in time-of-flight PET", EJNMMI Physics 3:3 DOI 10.1186/s40658-016-0138-3, (2016).

[66] William W. Moses, "Fundamental Limits of Spatial Resolution in PET", Nucl Instrum Methods Phys Res A. Aug 21; 648 Supplement 1: S236–S240, (2011).

[67] N. Ishida et al.,"Attenuation length measurements of scintillation light in liquid rare gases and their mixtures using an improved reflection suppresser", Nuclear Instruments and Methods in Physics Research Section A: Accelerators, Spectrometers, Detectors and Associated Equipment, Volume 384, Issues 2–3, (1997).

[68] Mehmet Aykac et al, "A Study of Narrow Energy Window on the Siemens Vision 600 PET/CT Scanner", Journal of Nuclear Medicine , Vol. 61, Issue supplement 1, May 1, (2020).

[69] https://bitbucket.org/theophysics/geant4cells/src/master/GATE/.